UNIVERSITY OF CALIFORNIA,
IRVINE

The seasonally varying ventilation of the ocean: a model-data synthesis

DISSERTATION

submitted in partial satisfaction of the requirements
for the degree of

DOCTOR OF PHILOSOPHY

in Earth System Science

by

Qian Huang

Dissertation Committee:
François Primeau, Chair
Adam Martiny
Kristen A. Davis
Tim DeVries

2019

TABLE OF CONTENTS

Page

LIST OF FIGURES **iv**

LIST OF TABLES **vi**

ACKNOWLEDGMENTS **vii**

CURRICULUM VITAE **viii**

ABSTRACT OF THE DISSERTATION **x**

1 Introduction **1**

2 CYCLOCIM: A 4-D variational assimilation system for the climatological mean seasonal cycle of the ocean circulation **7**

2.1 Introduction . . . 7
2.2 Tracer transport . . . 9
2.2.1 Space discretization . . . 10
2.2.2 Temperature model . . . 11
2.2.3 Salinity model . . . 11
2.2.4 Natural radiocarbon model . . . 12
2.2.5 Chlorofluorocarbons model . . . 12
2.2.6 Time discretization . . . 13
2.2.7 Cyclo-stationary solutions . . . 14
2.3 Dynamical model . . . 15
2.3.1 Space discretization . . . 17
2.3.2 Time discretization and cyclo-stationary state . . . 18
2.4 Bayesian inversion for the adjustable model parameters . . . 20
2.4.1 Summary of CYCLOCIM data-assimilation procedure . . . 25
2.5 Results . . . 26
2.5.1 Comparison of assimilated variables with observations . . . 28
2.5.2 Inferred air-sea fluxes and meridional transport of heat flux and fresh water . . . 36
2.5.3 Meridional overturning circulation . . . 39
2.6 Summary and discussion . . . 41

3 Characterizing Stommel's demon using a new data-constrained ventilation diagnostics **43**
3.1 Introduction . . . 43
3.2 Method . . . 49
3.2.1 Transit-time distribution (TTD) . . . 49
3.2.2 Forward and adjoint transport model . . . 52
3.2.3 Direct computation of moments of TTD using Newton krylov solver . 60
3.3 Results . . . 64
3.3.1 Global ocean . . . 65
3.3.2 North Atlantic . . . 71
3.3.3 North Pacific . . . 74
3.4 Discussion . . . 79

4 Quantifying ventillation of the deep water masses **85**
4.1 Introduction . . . 85
4.2 Method . . . 88
4.2.1 Cyclo-stationary Ocean Circulation Model . . . 88
4.2.2 TTD method . . . 89
4.3 Results . . . 89
4.3.1 Deep ocean . . . 90
4.3.2 NADW . . . 94
4.3.3 AABW . . . 96
4.3.4 PDW and IDW . . . 97
4.4 Discussion . . . 99

5 Discussion and future work **100**

Bibliography **105**

LIST OF FIGURES

Page

2.1 Schematic diagram of CYCLOCIM data-assimilation procedure 25
2.2 Evolution of the objective function 27
2.3 Evolution of the components of the objective-function 28
2.4 Joint distribution function for the gridbox-volume-weighted observed and modeled tracer concentrations 30
2.5 Horizontally-averaged root mean square error (RMSE) of tracers 31
2.6 Difference between modeled and observed temperature 32
2.7 Longitude-depth section of the modeled potential temperature abnormaly in comparison with the annual mean along 36°S 33
2.8 Difference between modeled and observed salinity in the upper 200m from OCIM 34
2.9 Modeled and observed Radiocarbon concentration 35
2.10 Modeled and Observed Chlorofluorocarbons concentrations 37
2.11 Heat flux and fresh water flux 38
2.12 Climatogical mean meridional overturning circulation (MOC) stream function 40

3.1 Schematic diagram of the subduction process 44
3.2 Schematic diagram of the obduction process 46
3.3 Schematic diagram of the surface-to-interior TTDs and the interior-to-surface TTDs 49
3.4 Schematic diagram of BIR and TTD 51
3.5 Schematic diagram of the forward and adjoint transport model 55
3.6 Surface-to-interior TTDs 59
3.7 Subduction of the upper ocean from January to June 65
3.8 Subduction of the upper ocean from July to December 66
3.9 Monthly subduction of the upper ocean in different ocean basins 67
3.10 Obduction of the upper ocean from January to June 68
3.11 Obduction of the upper ocean to surface from July to December 69
3.12 Monthly obduction of the upper ocean in different ocean basins 70
3.13 Subduction of the upper North Atlantic from January to June 72
3.14 Subduction of the upper North Atlantic from July to December 73
3.15 Monthly subduction of the upper North Atlantic in different ocean basins . . 74
3.16 Obduction of the upper North Atlantic from January to June 75
3.17 Obduction of the upper North Atlantic from July to December 76

3.18 Monthly obduction of the upper North Atlantic in different ocean basins . . 77
3.19 Subduction of the upper North Pacific from January to June 78
3.20 Subduction of the upper North Pacific from June to December 79
3.21 Monthly subduction of the upper North Pacific in different ocean basins . . . 80
3.22 Obduction of upper North Pacific from January to June 81
3.23 Obduction of upper North Pacific from July to December 82
3.24 Monthly obduction of the upper North Pacific in different ocean basins . . . 83

4.1 Global climatogical mean meridional overturning circulation (MOC) stream function. 92
4.2 Subduction of the deep Ocean 93
4.3 Obduction of the deep Ocean 93
4.4 Subduction and obduction of NADW 95
4.5 Subduction and obduction of AABW 96
4.6 Subduction and obduction of PDW 98
4.7 Subduction and obduction of IDW 98

LIST OF TABLES

Page

2.1 Vertical discretization used in CYCLOCIM 10

4.1 Subduction of deep water masses 90
4.2 Subduction of deep water masses 91

ACKNOWLEDGMENTS

I would like to thank my advisor François Primeau who taught me how to build the model and measure the "Stommel's demon". His patience, knowledge, and passion for science encourage me to finish the dissertation. Moreover, I would like to thanks my committees, Adam Martiny, Kristen Davis, Tim DeVries who gave me advises about my research. Finally, I would like to thank my friends and my family who supported me during the five years.

I would like to thank the National Science Foundation and the Department of Energy Office of Biological Research for the grants received by François Primeau.

CURRICULUM VITAE

Qian Huang

EDUCATION

Doctor of Philosophy in Earth System Science **2019**
University of California, Irvine *Irvine, CA*

Master of Science in Earth System Science **2016**
University of California, Irvine *Irvine, CA*

Master of Science in Physical Oceanography **2014**
South China Sea Institute of Oceanology, Chinese Academy of Science *Guangzhou, China*

Bachelor of Science in Atmospheric Science **2011**
Lanzhou University *Lanzhou, China*

RESEARCH EXPERIENCE

Graduate Research Assistant **2014–2019**
University of California, Irvine *Irvine, California*

TEACHING EXPERIENCE

Teaching Assistant **2016–2018**
University of California, Irvine *Irvine, California*

REFEREED CONFERENCE PUBLICATIONS

A Data-Constrained Climatological Model of the Ocean's Seasonally Varying Circulation **Feb 2018**
Ocean Science Meeting (OSM)

ABSTRACT OF THE DISSERTATION

The seasonally varying ventilation of the ocean: a model-data synthesis

By

Qian Huang

Doctor of Philosophy in Earth System Science

University of California, Irvine, 2019

François Primeau, Chair

This dissertation is a study of the climatological mean seasonal cycle of the ventilation of the ocean. Firstly, I have developed a computationally efficient 4-D variational assimilation system, called CYCLOCIM. It assimilates monthly mean temperature and salinity data from the World Ocean Atlas, transient CFC-11 and CFC-12, and natural radiocarbon measurements for the deep ocean from the GLODAPv2 database. CYCLOCIM is a new variational assimilation system that is specifically designed for the problem of estimating the climatological seasonal cycle of the residual mean circulation. I independently obtain the modeled overturning circulation, and the meridional heat and fresh water transport that largely agree with existing studies. Moreover, CYCLOCIM improves the model fit to the observation in the upper ocean compared to previous studies that ignored the seasonal cycle. The main product of the assimilation system is a set of 12 monthly data-constrained of tracer transport operators. I then calculate transit-time distribution (TTD) using the monthly transport operators to quantify "Stommel's demon", that is, the seasonality of the ventilation in the main thermocline. The study provides an accurate estimate of effective subduction and obduction months and maps of the water fraction in the main thermocline was last transported from or will be first transported back to the surface. For example, subduction occurs mainly in the Southern Ocean (64%), which lasts from June to November and peaks in September (21%) and October (20%). Moreover, the subduction happens in

the North Pacific (12%) and the North Atlantic (16%), which lasts from January to April and peaks in March (15%). Obduction occurs mainly in ACC region (48%), which starts from April to November and peaks in August. The upwelling regions of the tropical ocean is the secondary primary obduction region, which upwell 35% of the water back to surface and lasts the whole year. Furthermore, I have applied the TTD method to estimate the ventilation of the deep water masses. The formation of NADW, AABW, PDW, IDW occurs mainly in the surface of the Southern Ocean (respectively, 15%, 69%, 56% and 53%) and the Atlantic Ocean (respectively, 84%, 39%, 37% and 41%) during winter and spring in both hemisphere.

Chapter 1

Introduction

Ventilation is the process by which water and tracers are exchange between the surface and the interior ocean. It is the integrated results of the multiplicity of processes ranging from the global overturning circulation down to the small-scale turbulent mixing. Ventilation controls the physical properties of the ocean and the exchange of the heat, oxygen, and carbon between the atmosphere and ocean. Therefore, estimating oceanic circulation and ventilation precisely is crucial to understand ocean dynamics and simulate the transport of the biogeochemical tracer.

Ocean general circulation models (OGCMs) can be used to study the climatological mean ventilation of the ocean but they are suffering from some important shortcomings. First, it is computationally expensive to spin up OGCMs until they achieve the equilibrium. Moreover, OGCMs only use observation to set up an initial condition. Therefore, the longer models spun up, the further the model state drift from the observed ocean state. Furthermore, The parameterization of unresolved physical processes in OGCMs will produce biases in the estimate of the ventilation. Efforts have been made to improve the parameterizations with the development of the higher resolution OGCMs. It is generally believed that increasing the

model resolution will decrease model bias, however, the added computational cost generally leads to shorter spinups, and fewer efforts to optimize the subgrid scale parameterization, which will potentially lead to high bias in the ventilation process. Therefore, estimating ventilation using OGCMs will have significant biases.

On the other hand, an alternative method to estimate the circulation is using the observed tracer distributions to "advise" the model. The essential idea is that the concentration of the tracer in each water parcel carries information about its source and sink, ventilation pathway and transit timescale. Therefore, combing observations and dynamics can constrain the circulation which is called inverse method or the data assimilation method. The growing oceanic observation from the ships and satellites make it possible estimating the dynamic and biogeochemical state of the ocean using the inverse method. For example, the Version 2 of the Global Ocean Data Analysis Project (GLODAPv2) provides the assembled hydrographic and biogeochemical data from 724 scientific cruises (Olsen et al., 2016). Compared to the free-running OCGMs that only use observation to set up initial condition, the inverse method produces the circulation that is consistent with the ventilation of the observed tracers.

There are already multiple ocean reanalysis efforts that have been made to constrain the oceanic circulation by assimilating large sets of steady and transient hydrographic data (e.g. Schlitzer, 1993, 2007; DeVries and Primeau, 2011; Primeau et al., 2013; DeVries, 2014; Forget et al., 2015; Köhl, 2015). One of the important data assimilation models is the Estimating the Climate and Circulation of the Ocean (ECCO) project which estimates the circulation evolving from 1992 to 2015 using satellite data such as the temperature, salinity and sea surface height (Forget et al., 2015). The German ECCO (GECCO) is another ECCO project that assimilating model with the 50 years NCEP/NCAR reanalysis data (Köhl, 2015). The ECCO models set the initial state of the ocean as part of their control variables and repeatedly simulate the circulation for at most a few decades. However, it is not clear that whether the short simulation time makes the circulation in the deep ocean

is in equilibrium with surface forces. Moreover, the ECCO models don't include transient tracers such as natural radiocarbon and chlorouorocarbons (CFCs), which have been widely used to calculate the age of the deep water masses. Therefore, the ECCO models are not appropriate for studies related to ventilation in the deep ocean.

An alternative data assimilation strategy is to try to estimate the steady time-averaged climatological circulation directly instead of simulation the teme evolving circulation, for example, the adjoint ocean circulation model developed by Schlitzer (1993, 2007) and the Ocean Inverse Circulation Model (OCIM) developed by DeVries and Primeau (2011). In those studies, the climatologically mean circulation is constrained by not only the temperature, salinity data but by the transient tracers, such as the natural radiocarbon and chlorouorocarbons (CFCs). The advantage of those climatiological mean model is that they produce a non-drifting circulation with minimal biases that can be used to explore the ventilation pathways and rates on timescales. The main difference between Schlitzer (1993, 2007) and OCIM is the dynamic constraint. The former includes the horizontal velocity as the control parameter which is imposed to be consistent with the geostrophic circulation calculated from data. However, the OCIM constructs a dynamic model based on the linearized Navier-Stokes equations, which includes the wind-driven Ekman dynamics, geostrophy and eddy viscosity term and the adjustable term in the OCIM is the unresolved eddy stress. Moreover, The other advantage of the OCIM over the Schlitzer (1993, 2007) is that it provides the transport operator in the form of the sparse matrix, which can be used to calculate the tracer distribution. The transport matrix reduces the tracer simulation to a sequence of simple matrix-vector products and therefore provides a useful tool for the study of the marine biogeochemistry.

The transport operator of the OCIM have been widely used to compute large-scale tracer flux in recent years. For example, the OCIM transport operators coupled with a simple phosphorus cycle model was used first time to estimate the global map of the sequestration

efficiency of the biological pump (Devries et al., 2012b) and to estimates the biological pump efficiency in the Southern Ocean (Primeau et al., 2013). Moreover, The OCIM transport operators have been used to construct the global inverse marine nitrogen (N) cycle model to calculate denitrification in the three main suboxic zones (Devries et al., 2012a), to produce the 3-D estimates of denitrification rates (DeVries et al., 2013), to study the transformations between different forms of N in marine oxygen deficient zones (ODZs)(Martin et al., 2019b,a) and to estimate nitrogen fixation (Wang et al., 2019). Furthermore, the OCIM transport operators has been applied to construct inverse model to calculate the C:N:P stoichiometry of the exported organic matters. Teng et al. (2014) assessed the global variability in the C:P ratio in exported marine organic matter using the measurements of the dissolved inorganic carbon and the phosphate, and Devries and Deutsch (2014) estimated the ratio of the oxygen and the phosphate using the measurements dissolved oxygen and the nutrient phosphate. the OCIM transport operator also have been used to study the biological carbon pump and anthropogenic CO_2 uptake. For example, DeVries (2014) assessed oceanic uptake of the anthropogenic CO2 based on the climatological mean circulation from the OCIM, and DeVries et al. (2017) diagnose an increasing oceanic carbon uptake trend due to the weakening of the ventilation by constraining OCIM in different periods using the OCIM. Roshan and DeVries (2017) obtain the global-scale assessment of dissolved organic carbon DOC production and export by coupling the artificial neural network (ANN) produced DOC concentrations to a global ocean circulation model. Devries and Weber (2017) construct a new inverse model using the OCIM transport operators and satellite and oceanographic tracer observations to predict global particulate organic carbon (POC) flux. What's more, the OCIM is also used to study the submarine groundwater discharge (Kwon, 2014), the iron cycle (Frants et al., 2015), biological cycling of Zinc (Weber et al., 2018) and mantle helium source (Holzer et al., 2017). In summary, OCIM is proven to be a useful tool for the study of the marine biogeochemistry.

However, the current version of the OCIM assumes a climatological steady state, which

ignores the importance of the seasonality in the ventilation and the biogeochemical cycling. Throughout the year, the depth of the mixed layer varies seasonally due to the seasonal cycle of the heat flux on the surface. The circulation at the base of the mixed layer transfers mixed-layer water masses into the thermocline, a process called the subduction. (Stommel, 1979) argues that subduction only acts at the end of winter instead of continuously throughout the whole year. During the late winter, the mixed layer reaches its annual maximum density with a thick layer of almost vertically homogenized water. When spring comes, the rapid shoaling of the deep winter mixed layer leaves the homogenized water behind, which is then subducted into the permanent thermocline by the circulation. Water that is subducted during the summer and fall typically gets re-entrained into the mixed layer when the mixed layer deepens during the late fall and winter. Thus, only late-winter water properties make it into the permanent thermocline. The process is called "Stommel's demon", that is, the "demon" only opens the "trap door" to select end-of-winter properties for export into the permanent thermohaline. During the rest of the year, the door remains closed. On the other hand, the properties of the water mass in the mixed layer have a strong seasonal cycle. For example, primary production and particulate carbon export increase in the early spring when nutrient concentrations reach maximum and decrease sharply in the early summer and remain low throughout the rest of the year. This spring blooming draws down the dissolved inorganic carbon and nutrients in the surface waters. The study in Dall'Olmo et al. (2016) suggests that all the particulate organic carbon (POC) isolated below 100m is permanently exported during the transition period from winter to summer. In conclusion, the strong seasonal cycle of phytoplankton blooms coupled to the seasonality of the ventilation process leads to the important rectification effects in biogeochemical cycling. Therefore, it is necessary to obtain the seasonal varying circulation and produces the transport operators that resolve the seasonal cycle.

My research aims to constrain the circulation using the monthly observation and quantify the seasonal cycle of the ventilation in the main thermocline and deep ocean. Therefore, I develop

a 4-D variational assimilation system tp estimate the climatological mean seasonal cycle of the residual mean ocean circulation and hence provides a 12 monthly data constrained tracer transport operators. In chapter 2, I describe the governing equation and solution method and compare the model results with previous studies. In chapter 3, I develop a TTD method with a periodic solver combined with the monthly transport operators from CYCLOCIM to quantify when and where the "Stommel's demon" allows the surface water to enter the main thermocline or the water from the main thermocline return to the surface. In chapter 4, I apply the TTD method to study the ventilation of the deep water masses and hence compare the ventilation pathway to the previous understanding of the global overturning circulation (GOC). In chapter 5, I summary my research results and discuss the future application of the CYCLOCIM.

Chapter 2

CYCLOCIM: A 4-D variational assimilation system for the climatological mean seasonal cycle of the ocean circulation

2.1 Introduction

The application of inverse methods to global marine biogeochemical cycles has progressed rapidly in recent years because of the development of a data-constrained model for the global ocean circulation expressed in the form of a sparse Matlab matrix that can be used to efficiently compute large-scale tracer flux divergences (e.g. Devries et al., 2012a,a; DeVries et al., 2013; Holzer and Primeau, 2013; Devries and Deutsch, 2014; DeVries, 2014; Holzer et al., 2014; Teng et al., 2014; Frants et al., 2015; Holzer et al., 2016; Weber et al., 2016; DeVries et al., 2017; Pasquier and Holzer, 2016; Roshan et al., 2017; Pasquier and Holzer,

2017; Roshan and DeVries, 2017; Holzer et al., 2017; John et al., 2018; Wang et al., 2019; Martin et al., 2019b,a). The tracer-transport matrix used in the aforementioned studies is produced by a data assimilation system known as the Ocean Circulation Inverse Model (OCIM) (DeVries and Primeau, 2011; Primeau et al., 2013; DeVries, 2014; DeVries and Holzer, 2019). OCIM uses a variational method to assimilate stationary and transient tracers into a steady-state model for the large-scale momentum balance of the ocean. Through the assimilation process, the biases of prognostic ocean general circulation models (OGCMs) can be greatly reduced. As a result, biogeochemical inferences made on the basis of tracer flux divergences computed using OCIM are much easier to interpret than those obtained from free running OGCMs.

The steady-state assumption used in the OCIM system makes it possible to obtain a fully-spun up ocean state by direct matrix inversion rather than by a slow time-stepping spin-up as is used in traditional OGCMs. This capability makes it feasible to compute the $\mathcal{O}(10^3)$ forward and adjoint model solutions that are required by the iterative numerical optimization algorithm to bring the model state into agreement with the tracer-data constraints.

An important drawback of the steady-state formulation is that it ignores the pronounced seasonality of ventilation processes in mid to high latitudes (Marshall and Schott, 1999; Williams et al., 1995). This neglect can lead to potentially important and difficult to quantify biases. For example, it is well known that late-winter mixed layer water properties are preferentially selected for export to the permanent pycnocline (e.g. Stommel, 1979; Williams et al., 1995). By neglecting the seasonal cycle, the OCIM tracer-transport operator must necessarily be biased in the upper ocean if it is to reproduce the correct water-mass properties in the permanent thermocline and abyssal waters.

Here I present and extend OCIM assimilation system, which I call CYCLOCIM, that produces a cyclo-stationary state estimate for the climatological annual cycle of the ocean. The direct matrix inversions that were used to obtain fully spun-up steady states in OCIM are

replaced by calls to a cyclo-stationary Newton-Krylov solver (e.g. Li and Primeau, 2008; Bardin et al., 2014). In this paper I document the numerical formulation of the model and the solution method. In Section 2.2 I present the governing equations and solution method for the cyclo-stationary and transient tracers that are used to constrain the circulation. In Section 2.3 I present the governing equations for the residual mean circulation and the computational method used to obtain their cyclo-stationary solution. In Section 2.4 I give a Bayesian formulation of the inverse problem. I then present how I use the adjoint method to efficiently compute the gradient of the logarithm of posterior distribution so that I can locate the maximum of the posterior probability function. In Section 2.5 I compare the tracers simulated using our most probable model to the observed tracers. I show the most probable meridional overturning circulation conditioned on the tracer data and model formulation along with the implied meridional fluxes of heat and fresh water. Finally, in Section 2.6 I summarize the results and give directions for future model developments and applications.

2.2 Tracer transport

The primary observational constraint for the CYCLOCIM state estimate consist of hydrographic tracer observations. I therefore begin by describing the model's tracer equations. The advection-diffusion equation for a tracer c is given by

$$\frac{\partial c}{\partial t} + \nabla \cdot [\boldsymbol{u}^\dagger(t) - \mathbf{K}(t)\nabla]c = \mathcal{S}(c,t) \tag{2.1}$$

where $\mathbf{K}(t)$ is the tracer diffusivity tensor and $\boldsymbol{u}^\dagger(t)$ is the residual mean circulation. The implicit averaging operator used to define the residual mean is based on a projection of the ocean circulation onto its climatological mean seasonal cycle. Thus both $\boldsymbol{u}^\dagger(t)$ and $\mathbf{K}(t)$ are assumed to be periodic functions with a period of $\Delta T = 1$ year.

For the particular state estimates I present here, the diffusivity tensor is constructed using a horizontal diffusivity of 10^3 m^{2}s^{-1}, and a vertical diffusivity of 10^{-5} m^{2}s^{-1}. The horizontal diffusivity is rotated to lie along the isopycnal surfaces computed using the 2013 World Ocean Atlas monthly-mean temperature and salinity (Boyer et al., 2013). In addition, the vertical diffusivity is enhanced to a value of 1 m^{2}s^{-1} in a surface mixed layer of thickness h, which is prescribed according to the observed monthly-mean mixed layer depth climatology (de Boyer Montégut et al., 2004).

2.2.1 Space discretization

The version of the model I present here uses a staggered Arakawa C-grid discretization (e.g Haltiner and Williams, 1980) with a uniform horizontal resolution of $4^\circ \times 4^\circ$ and a vertical discretization with 24 layers whose thicknesses increase monotonically with depth (Table 2.1). At this resolution the model has a total of $N = 45\,515$ wet grid boxes. A discretized tracer field can then be organized into an $N \times 1$ column vector, $\boldsymbol{c}$, and the discretized version

Table 2.1: Vertical discretization used in CYCLOCIM. The thicknesses in meters increase monotonically with increasing depth.

36.1	37.3	40.7	46.3	54.2	64.4
76.8	91.5	108.4	127.6	149.1	172.8
198.7	227.0	257.5	290.2	325.2	362.5
402.0	443.8	487.8	534.1	582.7	633.5

of Eq.(2.1), expressed in matrix-vector form, is

$$\frac{d\boldsymbol{c}}{dt} + \boldsymbol{\Gamma}(t)\boldsymbol{c} = \boldsymbol{s}(\boldsymbol{c}, t), \tag{2.2}$$

where $\boldsymbol{s}$ is an $N \times 1$ source vector and $\boldsymbol{\Gamma}(t)$ is a $N \times N$ sparse matrix constructed such that the matrix-vector product $\boldsymbol{\Gamma c}$ produces the advective-diffusive tracer flux divergence in each of the model's wet grid boxes. In the construction of $\boldsymbol{\Gamma}$ the diffusive tracer fluxes are

discretized using a second-order centered differences and the advective fluxes are discretized using a 'Quick-up' scheme, that is, 'semi-upwind' in the horizontal and 'Quick' in the vertical (Leonard, 1979). For the grid-box interfaces separating the ocean from the land or atmosphere, $\mathbf{\Gamma}$ is constructed to satisfy no normal flux conditions.

2.2.2 Temperature model

For the temperature equation the source term $\boldsymbol{s}$ appearing in Eq. (2.2) consists of a surface heat flux, which I model by restoring the temperature in the model's upper-most layer to a prescribed temperature field, $\boldsymbol{\theta}_a(t)$, that is periodic in time, i.e. $\boldsymbol{\theta}_a(t + \Delta T) = \boldsymbol{\theta}_a(t)$. With N_s wet surface grid-boxes, $\boldsymbol{s}$ can be expressed in matrix-vector form as

$$\boldsymbol{s} = \frac{1}{\tau}\mathbf{\Lambda}_s(\boldsymbol{\theta}_a - \mathbf{\Lambda}_s^T \boldsymbol{c}), \tag{2.3}$$

where $\tau = 30$ days, $\mathbf{\Lambda}_s$ is an $N \times N_s$ sparse matrix with ones on the main diagonal and zeros elsewhere. The superscript T is used to denote the matrix transpose operation. The prescribed sea surface temperature field is constructed using the WOA2013 monthly climatology to which I add a small periodic in time correction to account for errors in the climatology , i.e. $\boldsymbol{\theta}_a(t) = \boldsymbol{\theta}_a^{\mathrm{WOA}}(t) + \delta\boldsymbol{\theta}_a(t)$. The unobserved correction, $\delta\boldsymbol{\theta}_a$, will be estimated as part of the Bayesian inversion.

2.2.3 Salinity model

For the salinity equation $\boldsymbol{s}$ consists of surface freshwater fluxes, which I model by restoring the salinity in the model's upper-most layer to a seasonally varying sea surface salinity field, $\boldsymbol{s}_a(t)$, that is periodic in time, i.e. $\boldsymbol{s}_a(t + \Delta T) = \boldsymbol{s}_a(t)$. Using a restoring timescale of $\tau = 30$

days, the source vector for salinity is given by i.e.

$$\boldsymbol{s} = \frac{1}{\tau}\boldsymbol{\Lambda}_s(\boldsymbol{s}_a - \boldsymbol{\Lambda}_s^T\boldsymbol{c}). \tag{2.4}$$

The prescribed sea surface salinity field is constructed using the WOA2013 monthly climatology to which I add a small periodic in time correction to account for errors in the climatology, i.e. $\boldsymbol{s}_a(t) = \boldsymbol{s}_a^{\mathrm{WOA}}(t) + \delta\boldsymbol{s}_a(t)$. The unobserved correction, $\delta\boldsymbol{s}_a$, will be estimated as part of the Bayesian inversion.

2.2.4 Natural radiocarbon model

For the natural (pre-bomb) radiocarbon model, the source function consists of the radioactive decay and air-sea gas exchange of $^{14}CO_2$, which I model simply as

$$\boldsymbol{s} = \frac{1}{\tau}\boldsymbol{\Lambda}_s({}^{14}\boldsymbol{c}_a - \boldsymbol{\Lambda}_s^T\boldsymbol{c}) - \lambda\boldsymbol{c}, \tag{2.5}$$

where $\lambda = -\log(2)/(5730 \text{ years})$ is the ^{14}C decay rate, ${}^{14}\boldsymbol{c}_s$ is the GLODAP estimate of the surface Δ^{14}C concentration prior to the atmospheric bomb tests and $\tau = 30$ days.

2.2.5 Chlorofluorocarbons model

Chlorofluorocarbon(CFCs) are transient tracers which have been released into the atmosphere since 1940. To simulate them I perform a transient simulation from 1940 up to 2009. For this I use the atmospheric history of CFC-11 and CFC-12 interpolated to a time resolution of one month (compiled by the U.S. Geological Survey Chlorofluorocarbon Laboratory and downloaded from http://water.usgs.gov/lab/software/air_curve/). To simulate the gas

exchange flux, I use the standard OCIM-2 formulation (see details in (DeVries, 2014)).

$$\boldsymbol{s} = \frac{\boldsymbol{\Lambda}_k}{dz_1}(\boldsymbol{c}^{atm} - \Lambda_s^T \boldsymbol{c}) \tag{2.6}$$

where $dz_1 = 36.1$ is the thickness of the model's upper most layer and $\boldsymbol{c}^{atm}$ is the prescribed atmospheric CFC concentration. The gas-exchange operator $\boldsymbol{\Lambda}_k$ is an $N \times N_s$ sparse matrix with non-zero elements on the main diagonal given by the piston velocity, k, scaled upwards using an adjustable parameter α, such that

$$k = \alpha \cdot (u_{10})^2 \cdot (Sc/660)^{-\frac{1}{2}} \cdot (1 - f_{\text{ice}}), \tag{2.7}$$

where u_{10} is the root-mean-square wind speed at 10 m above the sea surface, Sc is the temperature-dependent Schmidt number and f_{ice} is the climatological fractional ice cover.

2.2.6 Time discretization

The version of the model I present here uses a fully implicit Euler backward time-stepping scheme with a time step of one month:

$$\begin{aligned} \mathbf{B}_n \boldsymbol{c}_n &= \boldsymbol{c}_{n-1} + \boldsymbol{s}_n^o dt, \\ \mathbf{B}_n &\equiv \mathbf{I} + \left(\boldsymbol{\Gamma}_n - \left[\frac{\partial \boldsymbol{s}}{\partial \boldsymbol{c}} \right]_n \right) dt, \end{aligned} \tag{2.8}$$

for $n = 1, 2, \cdots, M$ with $dt = \Delta T/12$. In this equation the time-dependent tracer transport matrix, $\boldsymbol{\Gamma}(t)$, and the partial derivative of the tracer source function with respect to the tracer concentration, $\partial \boldsymbol{s}(\boldsymbol{c}, t)/\partial \boldsymbol{c}$ are discretized into 12 time-independent matrices $\boldsymbol{\Gamma}_n$ and $[\partial \boldsymbol{s}/\partial \boldsymbol{c}]_n$ respectively for $n = 1, 2, \cdots, 12$, with the condition that $\boldsymbol{\Gamma}_{n+12} = \boldsymbol{\Gamma}_n$ and $[\partial \boldsymbol{s}/\partial \boldsymbol{c}]_{n+12} = [\partial \boldsymbol{s}/\partial \boldsymbol{c}]_n$. The non-homogeneous part of the source function is discretized into time-dependent source vectors, $\boldsymbol{s}(0, t_n) = \boldsymbol{s}_n^o$ for $n = 1, 2, \cdots, M$. For the transient

CFC tracers I use the initial condition that $\boldsymbol{c} = 0$ and step the equations forward for $n = 1, 2, \cdots, M = N_{\text{yr}} \times 12$, corresponding to the period from 1940 to 2009. For salinity, temperature, and pre-bomb radiocarbon, the source vectors satisfy the same periodicity condition as the transport operators, i.e. $\boldsymbol{s}^o_{n+12} = \boldsymbol{s}^o_n$, implying that the fully spun-up solution ($M \to \infty$) will also be cyclo-stationary with $\boldsymbol{c}_{n+12} = \boldsymbol{c}_n$.

2.2.7 Cyclo-stationary solutions

With a one-month time-discretization and the Euler backward scheme the cyclo-stationary tracers (temperature, salinity, and pre-bomb radiocarbon) satisfy the following block-matrix system

$$\underbrace{\begin{bmatrix} -\mathbf{I}, & \mathbf{B}_1, & 0, & \cdots & 0 \\ 0 & -\mathbf{I} & \mathbf{B}_2 & \cdots & 0 \\ \vdots & & \ddots & \ddots & \vdots \\ 0 & 0 & \cdots & -\mathbf{I} & \mathbf{B}_{11} \\ \mathbf{B}_{12} & ... & ... & ... & -\mathbf{I} \end{bmatrix}}_{\tilde{\mathbf{B}}} \begin{bmatrix} \boldsymbol{c}_{12} \\ \boldsymbol{c}_1 \\ \boldsymbol{c}_2 \\ \vdots \\ \boldsymbol{c}_{11} \end{bmatrix} = \begin{bmatrix} \boldsymbol{s}^0_1 dt \\ \boldsymbol{s}^0_2 dt \\ \vdots \\ \boldsymbol{s}^0_{11} dt \\ \boldsymbol{s}^0_{12} dt \end{bmatrix}. \tag{2.9}$$

In principle one could try to obtain the cyclo-stationary solution to Eq.2.9 by directly inverting $\tilde{\mathbf{B}}$, but this is computationally very expensive because of the size of $\tilde{\mathbf{B}}$. This prohibitive computational costs is particularly true if I try to decrease the size of the time-step to better resolve the seasonal cycle. I therefore solve Eq.(2.9) using a pre-conditioned iterative Newton-Krylov solver without explicitly constructing the $\tilde{\mathbf{B}}$ matrix or the source vector on the right hand side (Li and Primeau, 2008; Khatiwala, 2008; Bardin et al., 2014; Fu and Primeau, 2017, e.g.)). I use the `nsoli.m` Newton Krylov solver (Kelley, 2013)). For the

preconditioner I use the same one first described in Li and Primeau (2008), namely

$$\mathbf{P} = \left(\frac{\Delta T}{12} \sum_{n=1}^{12} \left(\mathbf{\Gamma}_n - \left[\frac{\partial \boldsymbol{s}}{\partial \boldsymbol{c}} \right]_n \right) \right)^{-1} - \mathbf{I}, \tag{2.10}$$

which allows me to obtain fully-spun up cyclo-stationary solutions with the equivalent of only a few years of simulation – typically less than 10 and seldom more than 50.

2.3 Dynamical model

The dynamical model is based on the linearized Navier-Stokes equations with hydrostatic, Boussinesq and rigid-lid approximations

$$\begin{aligned}
u^\dagger_t - f v^\dagger + \frac{1}{a\cos\phi} g \eta_\lambda + \mathcal{D}u^\dagger &= -\frac{1}{a\cos\phi}\frac{p_\lambda}{\rho_0} + \frac{\delta_{1k}}{\Delta z_1}\frac{\tau^\lambda + \delta\tau^\lambda}{\rho_0} + \frac{1}{\rho_0}\tau_z^{e\lambda}, \quad (a) \\
v^\dagger_t + f u^\dagger + \frac{1}{a} g \eta_\phi + \mathcal{D}v^\dagger &= -\frac{1}{a}\frac{p_\phi}{\rho_0} + \frac{\delta_{1k}}{\Delta z_1}\frac{\tau^\phi + \delta\tau^\phi}{\rho_0} + \frac{1}{\rho_0}\tau_a^{e\phi}, \quad (b) \\
p &= g\int_z^0 \rho(z')dz', \quad (e) \\
\frac{1}{a\cos\phi}[(v^\dagger\cos\phi)_\phi + u^\dagger_\lambda] + w^\dagger_z &= 0, \quad (c) \\
\eta_t + \int_z^0 \{\frac{1}{a\cos\phi}[(v^\dagger\cos\phi)_\phi] + u^\dagger_\lambda\}dz &= 0, \quad (d)
\end{aligned} \tag{2.11}$$

where $(u^\dagger, v^\dagger, w^\dagger)$ is the residual mean velocity rather than the Eulerian mean; $\vec{\tau}^e = \left(\tau^{\lambda e}, \tau^{\phi e}\right)$ is a cyclo-stationary eddy-stress vector; η is the seasonally-varying mean dynamic topography; p is the climatologically-averaged seasonally-varying baroclinic pressure computed using the hydrostatic balance and the observed climatological density field; ρ is the climatologically-averaged seasonally-varying density; $\delta\vec{\tau}^w = (\delta\tau^{w\lambda}, \delta\tau^{w\phi})$ is a correction to the prescribed wind-stress climatology (e.g. Stammer et al., 2002; Ferreira et al., 2005; DeVries and Primeau, 2011); f is the Coriolis parameter; g is gravity. The friction operator, $\mathcal{D}$, is here taken to be a simple Rayleigh drag, i.e. $\mathcal{D}(u^\dagger, v^\dagger) = r(u^\dagger, v^\dagger)$, $r = 10^{-6}$ s^{-1}. λ is the longitude and ϕ is the

latitude. As previously mentioned, the averaging operator used to define the residual mean is based on a projection of the ocean circulation on its cyclo-stationary mean seasonal-cycle. Consequently, any deviation from this perfectly periodic state is, by definition, part of the "eddy" field.

Rewriting (2.11) in matrix-vector form I have

$$\partial_t \begin{bmatrix} u^\dagger \\ v^\dagger \\ w^\dagger \\ \eta \end{bmatrix} + \boldsymbol{\mathcal{M}} \begin{bmatrix} u^\dagger \\ v^\dagger \\ w^\dagger \\ \eta \end{bmatrix} = \mathcal{F} + \mathcal{F}^e \tag{2.12}$$

where

$$\boldsymbol{\mathcal{M}} = \begin{bmatrix} r & -f & 0 & \frac{1}{a\cos\phi} g\partial_\lambda \\ f & r & 0 & \frac{1}{a} g\partial_\phi \\ \frac{1}{a\cos\phi}\partial_\lambda & \frac{1}{a\cos\phi}\partial_\phi \cos\phi & \partial_z & 0 \\ \partial_z^{-1}\partial_\lambda & \partial_z^{-1}\partial_\phi \cos\phi & 0 & 0 \end{bmatrix} \tag{2.13}$$

with the linear operator ∂_z^{-1} defined to return the indefinite vertical integral of its operand, i.e. $\partial_z^{-1} q \equiv \int_z^0 q dz$. The forcing term on the right hand side is decomposed into two periodic forcing terms, $\mathcal{F}(t + \Delta T) = \mathcal{F}(t)$ and $\mathcal{F}^e(t + \Delta T) + \mathcal{F}^e(t)$. The first contribution consists of the wind-stress and the baroclinic pressure forces,

$$\mathcal{F}(t) \equiv \frac{1}{\rho_0} \begin{bmatrix} \frac{\delta_{1k}}{\Delta z_1}\tau^\lambda - \frac{g}{a\cos\phi}\partial_\lambda \partial_z^{-1}\rho \\ \frac{\delta_{1k}}{\Delta z_1}\tau^\phi - \frac{g}{a}\partial_\phi \partial_z^{-1}\rho \\ 0 \\ 0 \end{bmatrix}, \tag{2.14}$$

which can be computed directly from the observed climatological wind-stress obtained from

the European Centre for Medium-Range Weather Forecasts (ECMWF) climatological fields (Trenberth et al., 1989), and the observed climatological density computed using the equation of state for seawater and the World Ocean Atlas 2013 (Boyer et al., 2013) gridded temperature and salinity fields. The second contribution consists of the unobserved errors in the wind-stress climatology and the unresolved eddy-stress forcing

$$\mathcal{F}^e = \frac{1}{\rho_0} \begin{bmatrix} \frac{\delta_{1k}}{\Delta z_1}\delta\tau^\lambda + \partial_z \tau^{e\lambda} \\ \frac{\delta_{1k}}{\Delta z_1}\delta\tau^\phi + \partial_z \tau^{e\phi} \\ 0 \\ 0 \end{bmatrix}, \tag{2.15}$$

which will be inferred via the Bayesian inversion procedure using transient and cyclo-stationary tracer observations.

2.3.1 Space discretization

The dynamical state of the model is discretized using a staggered Arakawa B-grid finite-difference scheme (Haltiner and Williams, 1980) resulting in a discretized $122\,333 \times 1$ dynamical state vector $\boldsymbol{x} = [u^\dagger, v^\dagger, w^\dagger, \eta]$. With this discretization scheme, the operator $\boldsymbol{\mathcal{M}}$ becomes a time-independent $122\,333 \times 122\,333$ sparse-matrix operator. Similarly, the right-hand-side forcings, $\mathcal{F}$ and $\mathcal{F}^e$ become $122\,333 \times 1$ time-periodic vectors, $\mathcal{F}$ and $\mathbf{F}^e$. The resulting governing equation for the dynamics expressed in matrix-vector form is

$$\frac{d\boldsymbol{x}}{dt} + \mathbf{M}\boldsymbol{x} = \mathbf{F}(t) + \mathbf{F}^e(t). \tag{2.16}$$

2.3.2 Time discretization and cyclo-stationary state

Equation (2.16) can be further discretized in time using an Euler Backward scheme with $dt = \Delta T/12$, to get

$$\begin{aligned} \mathbf{A}\boldsymbol{x}_n &= \boldsymbol{x}_{n-1} + (\mathbf{F}_{n-1} + \mathbf{F}^e_{n-1})dt, \\ \mathbf{A} &\equiv \mathbf{I} + \mathbf{M}dt. \end{aligned} \tag{2.17}$$

with $\mathbf{F}_0 = \mathbf{F}_{12}$, $\mathbf{F}^e_0 = \mathbf{F}^e_{12}$, and $\boldsymbol{x}_0 = \boldsymbol{x}_{12}$. Because the forcing term on the right-hand-side is periodic in time the fully spun-up dynamical state will be cyclo-stationary and satisfy the following block-matrix system

$$\underbrace{\begin{bmatrix} -\mathbf{I} & \mathbf{A} & 0 & \cdots & 0 \\ 0 & -\mathbf{I} & \mathbf{A} & \cdots & 0 \\ \vdots & & \ddots & \ddots & \vdots \\ 0 & 0 & \cdots & -\mathbf{I} & \mathbf{A} \\ \mathbf{A} & 0 & \cdots & 0 & -\mathbf{I} \end{bmatrix}}_{\tilde{\mathbf{A}}} \begin{bmatrix} \boldsymbol{x}_{12} \\ \boldsymbol{x}_1 \\ \boldsymbol{x}_2 \\ \vdots \\ \boldsymbol{x}_{11} \end{bmatrix} = \begin{bmatrix} \mathbf{F}_1 + \mathbf{F}^e_1 \\ \mathbf{F}_2 + \mathbf{F}^e_2 \\ \vdots \\ \mathbf{F}_{11} + \mathbf{F}^e_{11} \\ \mathbf{F}_{12} + \mathbf{F}^e_{12} \end{bmatrix}. \tag{2.18}$$

The enormous size of the matrix, $\tilde{\mathbf{A}}$, precludes the use of a direct LU factorization to solve Eq. 2.18. I therefore obtain a solution to Eq. 2.18 using an iterative Newton-Krylov solver that avoids the need to explicitly construct $\tilde{\mathbf{A}}$. The convergence of the solver is greatly accelerated by the fact that it is possible to construct a nearly converged initial iterate using a Fourier representation of the continuous-time solution. Because $\mathbf{M}$ does not depend on t, a continous-time cyclo-stationary solution to Eq. 2.16 can be efficiently computed by first transforming the equation to Fourier space. To this end, I expand the forcing function and

the solution in Eq. (2.16) into truncated Fourier series with 6 complex sinusoidal modes

$$\begin{aligned} \mathbf{F}(t) + \mathbf{F}^e(t) &= \sum_{k=0}^{5} \widehat{\mathbf{F}}_k e^{ik2\pi t/\Delta T}, \\ \boldsymbol{x}(t) &= \sum_{k=0}^{5} \widehat{\boldsymbol{x}}_k e^{ik2\pi t\Delta T}, \end{aligned} \tag{2.19}$$

which transforms Eq, (2.16) into an system of 733 998 complex-valued algebraic equations

$$\begin{bmatrix} i\omega_0\mathbf{I}+\mathbf{M} & 0 & & 0 \\ 0 & i\omega_1\mathbf{I}+\mathbf{M} & 0 & \vdots \\ \vdots & 0 & \ddots & 0 \\ 0 & & 0 & i\omega_5\mathbf{I}+\mathbf{M} \end{bmatrix} \begin{bmatrix} \widehat{\boldsymbol{x}}_0 \\ \widehat{\boldsymbol{x}}_1 \\ \vdots \\ \widehat{\boldsymbol{x}}_5 \end{bmatrix} = \begin{bmatrix} \widehat{\mathbf{F}}_0 \\ \widehat{\mathbf{F}}_1 \\ \vdots \\ \widehat{\mathbf{F}}_5 \end{bmatrix}. \tag{2.20}$$

Because the matrix in Eq. (2.20) is block-diagonal it uncouples into 6 independent 122 333 × 122 333 systems, each of which can be solved using a complex sparse-matrix LU factorization. The resulting continuous-time solution can then be evaluated at $t = 0$ to construct an initial iterate

$$\boldsymbol{x}_1 = \Re\left\{\sum_{k=0}^{5} \widehat{\boldsymbol{x}}_k\right\}, \tag{2.21}$$

for the Newton Krylov solver. Using this approach, fully spun-up cyclo-stationary solutions can be obtained using this method with the equivalent of only a few years of simulation – typically 5 or less – without the need for a sophisticated preconditioner.

2.4 Bayesian inversion for the adjustable model parameters

As presently formulated the model has a suite of adjustable parameters, organized into an $980\,737 \times 1$ vector,

$$\boldsymbol{p} = \left[\begin{array}{ccccccc} \partial_z \boldsymbol{\tau}_e^{\lambda} & \partial_z \boldsymbol{\tau}_e^{\phi} & \delta\boldsymbol{\tau}^{\lambda} & \delta\boldsymbol{\tau}^{\phi} & \delta\boldsymbol{\theta}_a & \delta\boldsymbol{s}_a & \alpha \end{array} \right]^T, \tag{2.22}$$

that must be specified for the problem to be well posed. I infer their values via a Bayesian inversion procedure constrained by tracer observations.

To this end I assign normal probability distributions to the observed tracer concentrations, with the mean of the distributions given by the model's simulated concentrations. Specifically, the probability of the data conditioned on the model parameters, is given by

$$\text{prob}(\boldsymbol{c}_i^{\text{obs}}|\boldsymbol{p}) \propto \exp\left[-\frac{1}{2} (\mathbf{H}_i \boldsymbol{c}_i - \boldsymbol{c}_i^{\text{obs}})^T \mathbf{W}_i (\mathbf{H}_i \boldsymbol{c}_i - \boldsymbol{c}_i^{\text{obs}}) \right] \tag{2.23}$$

where the index $i = 1, 2, \cdots 5$ identifies the particular tracer being considered, i.e. temperature, salinity, CFC-11, CFC-12, or pre-bomb radiocarbon. The likelihood function for temperature was modified from the Gaussian density by a factor that assigns a very low probability tp temperatures that fall close to or below the freezing point of seawater, i.e. $\exp\left\{-\omega_{\text{ice}} \boldsymbol{\phi}^T \boldsymbol{\phi})\right\}$, where $\boldsymbol{\phi} = \tanh\left[\exp\left\{-(T + 2.6°\text{C})/0.1°\text{C}\right\}\right]$ and $\omega_{\text{ice}} = 10^4$. The matrices $\mathbf{H}_i$ are used to select the grid-boxes and months for which I have tracer observations. For tempeature and salinity these matrices are identity matrices because I constrain the model using the gridded climatology, but for the other tracers I use bottle measurements. The scaled precision matrices, $\mathbf{W}_i$, are taken to be the sum of two symmetric matrices one of which is positive definite. The positive definite matrix is diagonal with entries given by the reciprocals of the variances σ_i^2 computed from all the observations available for a given month

and grid box (for temperature, salinity, and pre-bomb radiocarbon) and for a particular, grid box, month, and year for the transient CFC-11 and CFC-12 tracers, and then divided by the numbers of observations. The other matrix is given by $\beta_i \mathbf{L}^T\mathbf{L}$ where $\mathbf{L}$ is a discretized version of the horizontal Laplacian operator in spherical coordinates. The Laplacian operator is only added in the distribution of the temperature and the salinity term. The value of β_i is given by one over the product of the variance of calculated σ_i^2 for a given layer and month and the number of observation used in the tracer simulation. I further assume that conditioned on the model, all the tracer observations are independent allowing us to construct the likelihood function by simply multiplying the probability densities for each tracer, i.e.

$$\text{prob}(\{\boldsymbol{c}_i^{\text{obs}}\}_{i=1}^{5}|\boldsymbol{p}) = \prod_{i=1}^{5} \text{prob}(\boldsymbol{c}_i^{\text{obs}}|\boldsymbol{p}). \tag{2.24}$$

For the prior probability of $\boldsymbol{p}$ I assume a normal distribution centered at $\boldsymbol{p} = 0$,

$$\text{prob}(\boldsymbol{p}) \propto \exp\left[-\frac{1}{2}\boldsymbol{p}^T\mathbf{W}_p\boldsymbol{p}\right], \tag{2.25}$$

with a prior precision matrix, $\mathbf{W}_p$, taken to be diagonal. For the unobserved errors in the wind-stress climatology, $\delta\boldsymbol{\tau}^\lambda, \delta\boldsymbol{\tau}^\phi$ and the unresolved eddy-stress forcing, $\partial_z\boldsymbol{\tau}_e^\lambda, \partial_z\boldsymbol{\tau}_e^\phi$, the diagonal elements of $\mathbf{W}_p$ is the $\frac{1}{(0.1\mathbf{F})^2 n}$, where $\mathbf{F}$ is the forcing vector in Eq.2.16, and the n is the number of the parameters. For the $\delta\boldsymbol{\theta}_a, \delta\boldsymbol{\lambda}_a$, the diagonal elemnets are one over the product of variance computed from all the observation for a given month and grid box in the surface layer. Moreover, I assign a flat prior for the α. I further constrained the prior distribution of the parameters implicitly by assigning a weak prior on the dynamical state of the model, i.e. I assigned a normal distribution centered at zero

$$\text{prob}(\boldsymbol{x}|\boldsymbol{p}) \propto \exp\left[-\frac{1}{2}\boldsymbol{x}^T\mathbf{W}_x\boldsymbol{x}\right] \tag{2.26}$$

where the precision matrix, $\mathbf{W}_x$, is taken to be diagonal with very low values for the precisions

for the horizontal velocity. This weak constraint is helpful in the early stages of the parameter optimization as it prevents the search algorithm from suggesting parameter values that lead to completely implausible dynamical states. It's impact on the ultimate solution is completely negligible. For the vertical velocity, I have tried two version of the precision matrix that representing different penalty. The model run that using the same penalty as DeVries (2014) is called CYCLOCIM$_0$, and the model run that increase the penalty to fiftyfold as DeVries and Holzer (2019) is called CYCLOCIM. The increased penalty have significantly reduced the vertical velocity to the similar magnitude as the vertical velocities estimated from the Estimating the Circulation and Climate of the Ocean data assimilation (ECCO) (DeVries and Holzer, 2019).

With the above choices the posterior probability density function obtained via Bayes' theorem is

$$\begin{aligned}\mathbf{prob}(\boldsymbol{p}|\{\boldsymbol{c}_i^{\text{obs}}\}_{i=1}^5) \propto \exp\Big[&-\frac{1}{2}\sum_{i=1}^{5}(\mathbf{H}_i\boldsymbol{c}_i-\boldsymbol{c}_i^{\text{obs}})^T\mathbf{W}_i(\mathbf{H}_i\boldsymbol{c}_i-\boldsymbol{c}_i^{\text{obs}}) \\ &-\frac{1}{2}\omega_{\text{ice}}\boldsymbol{\phi}^T\boldsymbol{\phi}-\frac{1}{2}\boldsymbol{x}^T\mathbf{W}_x\boldsymbol{x}-\frac{1}{2}\boldsymbol{p}^T\mathbf{W}_p\boldsymbol{p}\Big]\end{aligned} \tag{2.27}$$

The posterior probability density described by equation (2.27) lives in a high-dimensional space. Here I limit ourselves to summarizing the posterior density in terms of the location of its maximum, which is equivalent to finding the minimum of the negative logarithm of the posterior density,

$$\begin{aligned}\widehat{f}(\boldsymbol{p}) \equiv& f(\boldsymbol{y}(\boldsymbol{p}),\boldsymbol{p}) \\ =&\frac{1}{2}\sum_{i=1}^{5}(\mathbf{H}_i\boldsymbol{c}_i-\boldsymbol{c}_i^{\text{obs}})^T\mathbf{W}_i(\mathbf{H}_i\boldsymbol{c}_i-\boldsymbol{c}_i^{\text{obs}})+\frac{1}{2}\omega_{\text{ice}}\boldsymbol{\phi}^T\boldsymbol{\phi} \\ &+\frac{1}{2}\boldsymbol{x}^T\mathbf{W}_x\boldsymbol{x}+\frac{1}{2}\boldsymbol{p}^T\mathbf{W}_p\boldsymbol{p}.\end{aligned} \tag{2.28}$$

where $\boldsymbol{y}(\boldsymbol{p}) = \left[\begin{array}{cccc} \boldsymbol{x} & \boldsymbol{c}_1 & \cdots & \boldsymbol{c}_5 \end{array}\right]$ is the solution to the model equations, $F(\boldsymbol{y}, \boldsymbol{p}) = 0$, combining the cyclo-stationary dynamical state with the cyclo-stationary temperature, salinity, radiocarbon solutions with the transient CFC-11 and CFC-12 solutions.

I solve the above problem using a quasi-Newton method. Following Heinkenschloss (2008), I express the gradient of $\widehat{f}(\boldsymbol{p})$ in terms of the partial gradients of $f(\boldsymbol{y}, \boldsymbol{p})$,

$$\begin{aligned} \nabla_{\boldsymbol{p}} \widehat{f}(\boldsymbol{p}) &= \boldsymbol{y}_{\boldsymbol{p}}^T \nabla_{\boldsymbol{y}} f(\boldsymbol{y}(\boldsymbol{p}), \boldsymbol{p}) + \nabla_{\boldsymbol{p}} f(\boldsymbol{y}, \boldsymbol{p}) \\ &= -(F_{\boldsymbol{y}}(\boldsymbol{y}(\boldsymbol{p}), \boldsymbol{p})^{-1} F_{\boldsymbol{p}}(\boldsymbol{y}(\boldsymbol{p}), \boldsymbol{p}))^T \nabla_{\boldsymbol{y}} f(\boldsymbol{y}(\boldsymbol{p}), \boldsymbol{p})) + \nabla_{\boldsymbol{p}} f(\boldsymbol{y}(\boldsymbol{p}), \boldsymbol{p}), \\ &= F_{\boldsymbol{p}}(\boldsymbol{y}(\boldsymbol{p}), \boldsymbol{p})^T \boldsymbol{\lambda}(\boldsymbol{p}) + \nabla_{\boldsymbol{p}} f(\boldsymbol{y}(\boldsymbol{p}), \boldsymbol{p}), \end{aligned} \tag{2.29}$$

where $\boldsymbol{\lambda}(\boldsymbol{p})$ is the solution to

$$\left[F_{\boldsymbol{y}}(\boldsymbol{y}(\boldsymbol{p}), \boldsymbol{p})\right]^T \boldsymbol{\lambda}(\boldsymbol{p}) = -\nabla_{\boldsymbol{y}} f(\boldsymbol{y}, \boldsymbol{p}). \tag{2.30}$$

The great computational advantage of using the last expression in Eq. (2.29) rather than the one in the middle line is that it involves solving only one linear system of equations for $\boldsymbol{\lambda}(\boldsymbol{p})$ instead of solving a separate linear system for each the 980 737 components of $\boldsymbol{p}$. Because the linear system involves the transposed Jacobian matrix, $\left[F_{\boldsymbol{y}}(\boldsymbol{y}(\boldsymbol{p}), \boldsymbol{p})\right]^T$ it is known as the adjoint method (e.g. Schlitzer, 1993, 2007; DeVries and Primeau, 2011).

The adjoint system (2.30) and $\boldsymbol{\lambda}(\boldsymbol{p})$ can be partitioned into components which can be solved separately. Specifically,

$$\boldsymbol{\lambda}(\boldsymbol{p})^T = \left[\begin{array}{cccccc} \boldsymbol{\lambda}_{\boldsymbol{x}}^T & \boldsymbol{\lambda}_{\boldsymbol{\theta}}^T & \boldsymbol{\lambda}_{\boldsymbol{s}}^T & \boldsymbol{\lambda}_{\boldsymbol{c}_{14}}^T & \boldsymbol{\lambda}_{\text{CFC-11}}^T & \boldsymbol{\lambda}_{\text{CFC-12}}^T \end{array}\right] \tag{2.31}$$

where

$$\mathbf{B}_n^T \boldsymbol{\lambda}_{\boldsymbol{c}_n} = \boldsymbol{\lambda}_{\boldsymbol{c}_{n+1}} + \nabla_{\boldsymbol{c}_n} f(\boldsymbol{y}, \boldsymbol{p}) dt, \tag{2.32}$$

for $n = M, M-1, \cdots, 1$. For the cases where $\boldsymbol{c}_n$ correspond to the transient CFC tracers, the system is solved starting with the final condition $\boldsymbol{\lambda}_{\boldsymbol{c}_{M+1}} = 0$ and time-stepped backwards in time from $= M = N_{\text{yr}} \times 12$ and down to $n = 1$. For the cyclo-stationary tracers, the $\boldsymbol{\lambda}_{\boldsymbol{c}_n}$ are also periodic and solutions are obtained using the same Newton-Krylov method used for the forward tracers except that the the operators are cycled in reverse order and the transposed operators are used for both the $\mathbf{B}_n$'s and the preconditioner.

Having obtained the Lagrange multipliers corresponding to the tracer variables, the Lagrange multipliers corresponding to the model's dynamical state can be obtained by solving for the cyclo-stationary state of

$$\mathbf{A}^T \boldsymbol{\lambda}_{\boldsymbol{x}_n} = \boldsymbol{\lambda}_{\boldsymbol{x}_{n+1}} + \mathbf{F}_n^\dagger dt \tag{2.33}$$

where the monthly forcing terms are given by

$$\begin{aligned} \mathbf{F}_n^\dagger = & \boldsymbol{\Gamma}_{\boldsymbol{x}_n} \left[\boldsymbol{\lambda}_{\boldsymbol{\theta}_n} + \boldsymbol{\lambda}_{\boldsymbol{s}_n} + \boldsymbol{\lambda}_{\boldsymbol{c}_{14,n}} + \sum_{m=1}^{N_{\text{yr}}} \left(\boldsymbol{\lambda}_{\text{CFC-11},m,n} + \boldsymbol{\lambda}_{\text{CFC-12},m,n} \right) \right] \\ & - \nabla_{\boldsymbol{x}_n} f(\boldsymbol{y}, \boldsymbol{p}) \end{aligned} \tag{2.34}$$

for $n = 1, 2, \cdots, 12$, where $\boldsymbol{\Gamma}_{\boldsymbol{x}_n}$ corresponds to the partial derivative of the tracer transport operator with respect to the dynamical state variable during month n. Cyclo-stationary solutions are obtained using the same Newton-Krylov solver used for the forward model except that the transpose of $\mathbf{A}$ is used and the forcing terms are cycled in reversed time order.

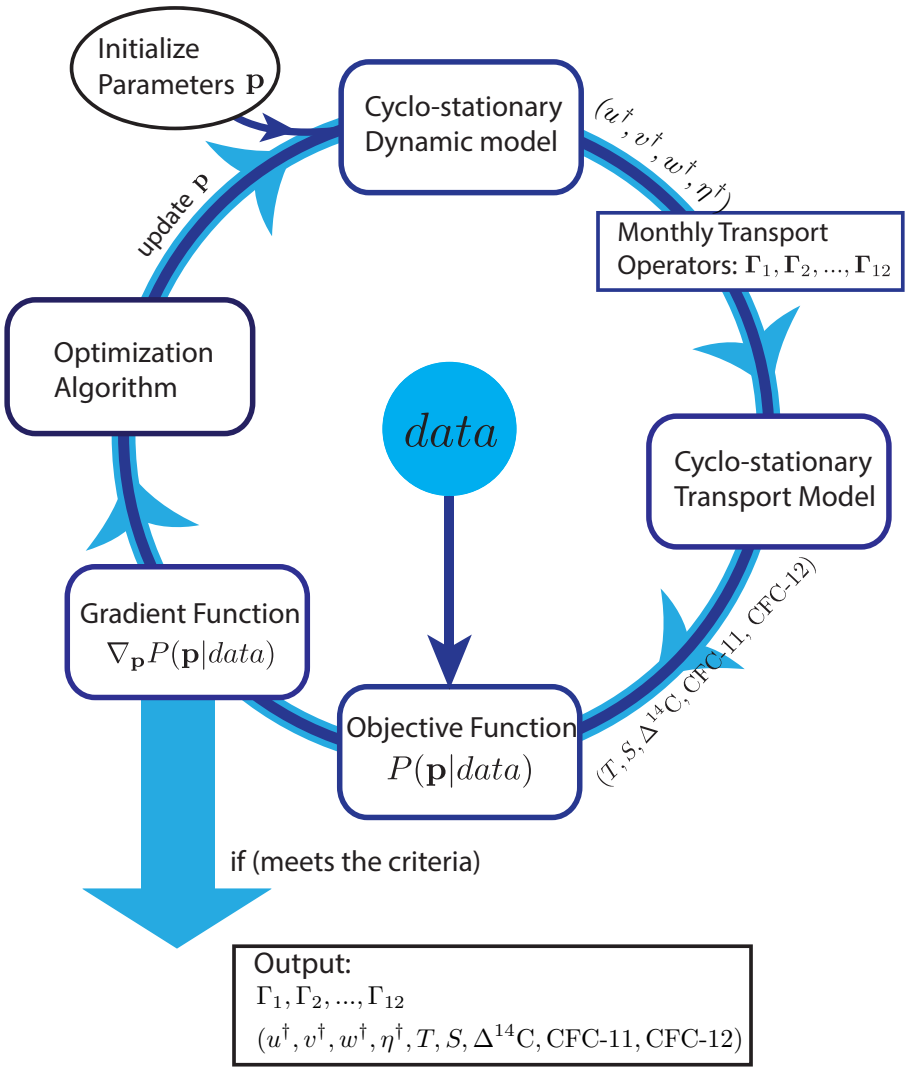

Figure 2.1: The workflow of the cyclo-stationary ocean circulation inverse model (CYCLOCIM).

2.4.1 Summary of CYCLOCIM data-assimilation procedure

The CYCLOCIM data-assimilation system solves the constrained optimization problem

$$\begin{aligned} &\underset{\boldsymbol{y},\boldsymbol{p}}{\text{minimize}} f(\boldsymbol{y},\boldsymbol{p}) \\ &\text{such that } C(\boldsymbol{y},\boldsymbol{p}) = 0 \end{aligned} \tag{2.35}$$

where $\widehat{f}(\boldsymbol{p}) = f(\boldsymbol{y}(\boldsymbol{p}), \boldsymbol{p})$ is the negative of the logarithm of the posterior probability density for $\boldsymbol{p}$ and $C(\boldsymbol{y}, \boldsymbol{p}) = 0$ are the governing equations for the dynamical and tracer states of the model. The solution procedure is summarized in Figure 2.1. The iterative procedure consists of repeating five main steps: (1) Given a current estimate of $\boldsymbol{p}$, solve the cyclo-stationary dynamical model to obtain $\boldsymbol{x}(\boldsymbol{p})$, i.e. the seasonally varying residual mean circulation $(u^\dagger, v^\dagger, w^\dagger)$ and dynamic topography (η), (2) solve the transient tracers ($\boldsymbol{c}_{\text{CFC-11}}$ and $\boldsymbol{c}_{\text{CFC-12}}$) and the cyclo-stationary tracers, temperature salinity and natural radiocarbon ($\boldsymbol{\theta}$, $\boldsymbol{s}$, and $\boldsymbol{c}_{14}$) using the sparse-matrix tracer transport operators constructed using the current estimate of $\boldsymbol{x}$, (3) evaluate the objective function for the given $\boldsymbol{p}$, (4) compute the gradient of the objective function $\nabla_{\boldsymbol{p}}\widehat{f}(\boldsymbol{p})$ and check if the minimum has been reached, and (5) use a quasi-newton search algorithm and $\nabla_{\boldsymbol{p}}\widehat{f}(\boldsymbol{p})$ to produce an improved (more probable) estimate of $\boldsymbol{p}$. The data assimilation procedure I use is equivalent to what is sometimes called a 4-D variational assimilation system except that the time-dependent part of the procedure is restricted to be periodic for the circulation and the non-transient tracers.

2.5 Results

I conducted state estimates for a version of CYCLOCIM with a resolution of $8^\circ \times 8^\circ \times 22$ layers and $4^\circ \times 4^\circ \times 24$ layers. The optimization for a version of CYCLOCIM with the standard OCIM resolution of $2^\circ \times 2^\circ \times 24$ layers is underway, but the optimal solution has not yet been found. Our goal is to present the higher resolution circulation in a separate paper than can focus on the state estimate rather than the technical asspects of the assimilation, which is the main focus of the present report.

The evolution of the objective function for the $8^\circ \times 8^\circ \times 22$ model for the first 10 000 iterations is shown in Figure 2.2. Initially, the objective function is approximately 10^4. After 10,000 iterations the objective function is less than 5.4. The drop is fastest for the first 2000

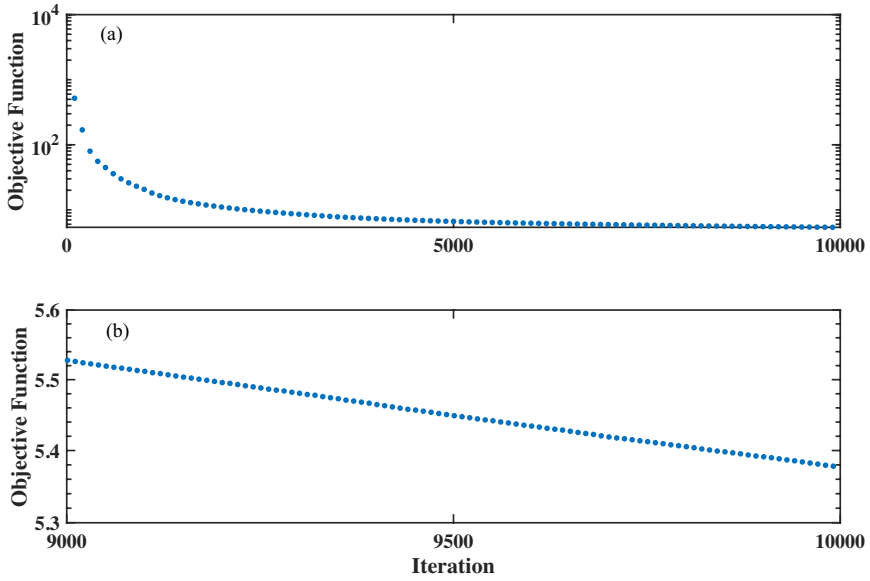

Figure 2.2: The evolution of objective function of $8° \times 8° \times 24$ model run in (a) 10000 iterations (b) last 1000 iteration.

iterations and the rate of decrease slows down afterwards. While the rate of decrease is modest in the last 1000 iterations, $\widehat{f}(\boldsymbol{p})$ is still decreasing monotonically. However the changes in the resulting state estimate are rather modest. For the version of CYLCOCIM with a $4° \times 4° \times 24$ resolution, which I present in the next section I performed approximately 4×10^3 iterations but I restarted the optimization along the way because I did not include all the tracer constraints at the beginning.

For the $4° \times 4° \times 24$ layer resolution version of CYCLOCIM I did a preliminary optimization, which I call CYCLOCIM$_0$, and a second estimation in which I increased the prior precision on the vertical velocity of the model so as to penalize large vertical velocities. In this respect, I follow DeVries and Holzer (2019) who showed improvements in the simulated meridional overturning circulation with a penalty on large vertical velocities. In Figure 2.3 I show the different terms that contribute to the logarithm of the posterior probability for CYLCOCIM as a function of the iteration during the parameter optimization. Iteration zero corresonponds to the optimal solution for CYCLOCIM$_0$ The contribution from the penalty

on the vertical velocity starts from 30 at iteration 0 and decreases to less than 4 after 3000 iterations, while the other terms increase rapidly at first and then decrease gradually as the number of optimization steps increases. The results I present in the rest of the paper correspond to CYCLOCIM with the penalty on w unless explicitly stated. In which case they are referred to as the CYLCOCIM$_0$ estimate.

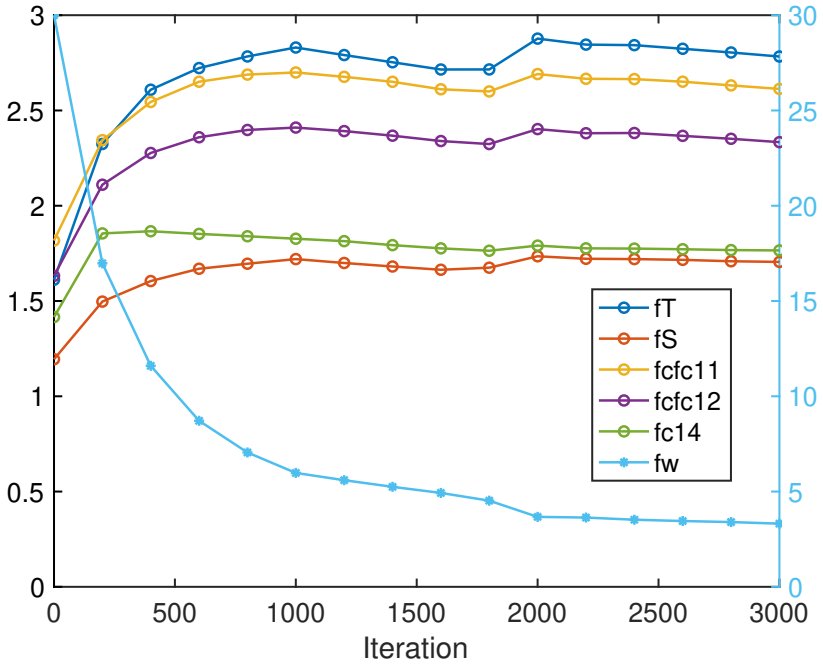

Figure 2.3: The evolution of the components of the objective-function for 3000 iterations of CYCLOCIM starting with the optimal solution for CYCLOCIM$_0$. The difference between CYLCOCIM and CYCLOCIM$_0$ is that I increased the prior precision on the vertical velocity so as to penalize circulations with large vertical velocities. The components of the objective function include those for the temperature (fT), salinity (fS), CFC11 (fcfc11), CFC12 (fcfc12), Δ^{14}C (fc14) use the left axis where as the component for the vertical velocity (fw) uses the right axis.

2.5.1 Comparison of assimilated variables with observations

A summary of the model fit to the data is provided in Figure 2.4 where I show the joint cumulative distribution functions for the observed and modeled tracer variables assimilated

by the model. The joint distribution was estimated using the kernel density estimation method described in Botev et al. (2010) and modified to produce a volume weighted distribution (Primeau et al., 2013). For all tracers more than 90% of volume is tightly clustered along the 1:1 line with $R^2 = 0.99$ for potential temperature, and $R^2 \approx 0.96$ for the other tracers. The close agreement between the modelled and observed tracers suggests that the CYCLOCIM circulation can be used to produce meaningful estimates of the climatological water mass formation rates and transport for the real ocean – analyzing the model solution is essentially equivalent to analyzing the climatological observations.

By resolving the seasonal cycle, the CYCLOCIM state estimate provides a better fit to the observations than the steady OCIM state estimates at mid to high latitudes in the surface mixed layer and seasonal thermocline. In Figure 2.5 the globally averaged root mean square errors (RMSE) for the potential temperature, salinity, CFC-11 from CYCLOCIM are compared to the corresponding RMSE for the OCIM CTRL state estimate (DeVries, 2014). For the deep ocean below 1000 m where seasonality is negligible the RMSE is similar for both state estimates.

The globally averaged RMSE for CYCLOCIM is 0.27°C, whereas for OCIM it is 0.45°C. For the surface waters, 0 – 200m, the decrease in the RMSE is significantly bigger: 0.46°C for CYCLOCIM versus 1.27°C for OCIM. Most of the improvements occur in mid-latitudes (Figure 2.6) where the mixed layer depths have a pronounced seasonal variation. For example, in the region of the Kuroshio Extension the cold bias of more than 3°C in the OCIM state estimate is substantially decreased in the CYCLOCIM state estimate despite the fact that the CYCLOCIM state estimate corresponds to a model with a horizontal resolution of only $4^\circ \times 4^\circ$ whereas the OCIM state estimate is for a horizontal resolution of $2^\circ \times 2^\circ$. Similarly, the low-latitude warm bias in the OCIM state estimate have been eliminated in the CYCLOCIM state estimate. Therefore, the CYCLOCIM have significantly improve the model fitness compared to the OCIM.

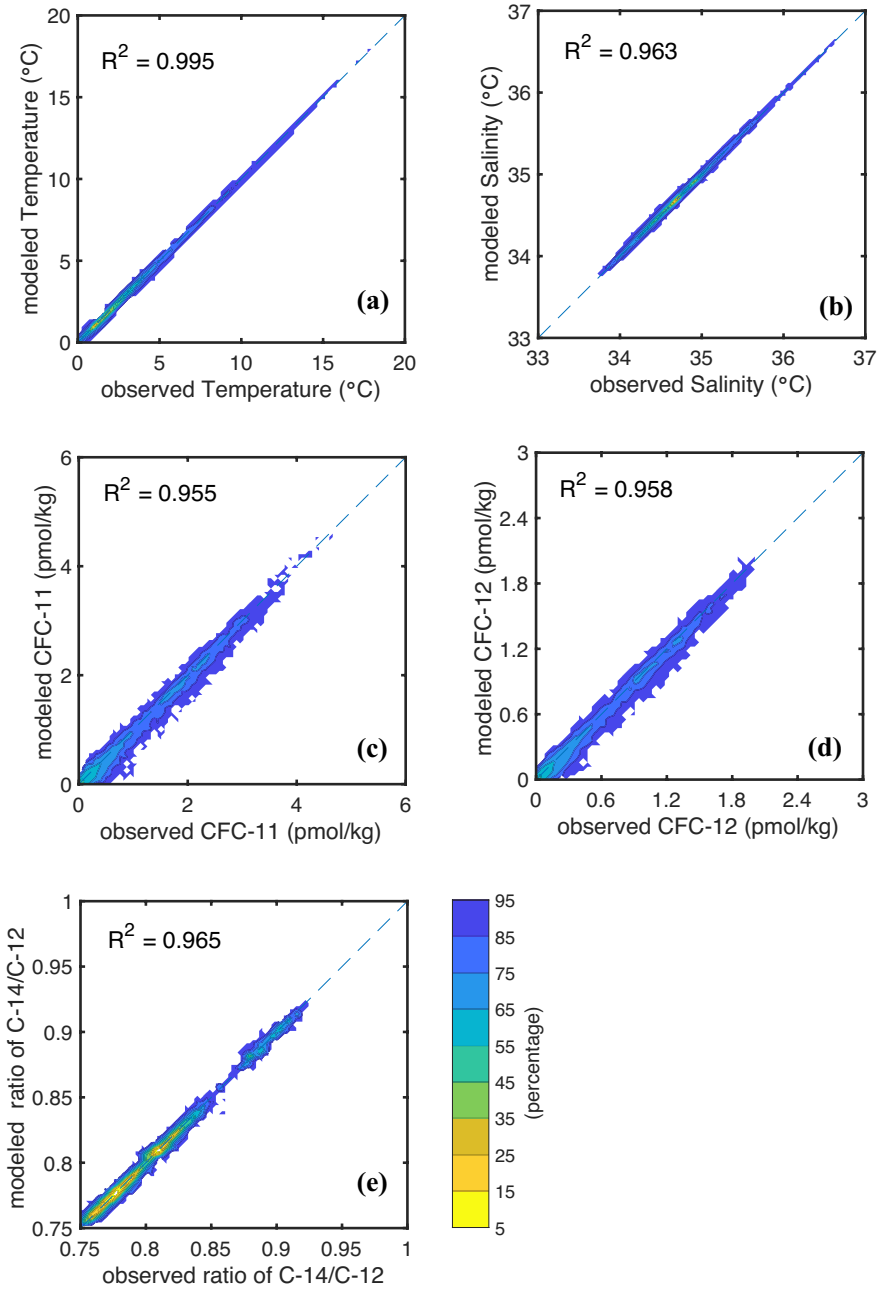

Figure 2.4: Joint distribution function for the gridbox-volume-weighted observed and modeled tracer concentrations: (a) potential temperature (b) salinity (c) CFC-11 (d) CFC-12 (e) Δ^{14}C, which are expressed in terms of the percentages of the cumulative distribution function. The Nth percentage is defined such that N% of the joint distribution lies inside N% contour.

The ability of the model to capture the correct seasonal cycle is illustrated in Figure 2.7 in which I compare the potential temperature anomalies (plotted as departure from the

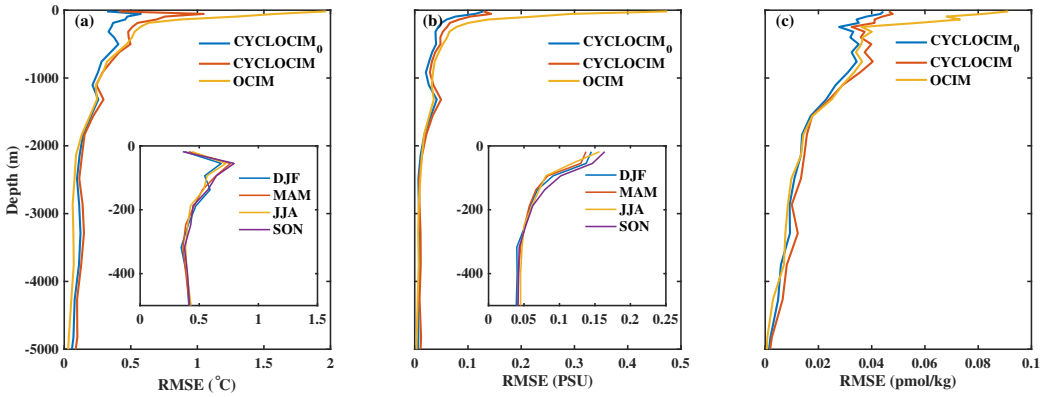

Figure 2.5: Horizontally-averaged root mean square error (RMSE) of (a) annual-mean potential temperature, (b) annual-mean salinity, and (c) CFC-11, computed from CYCLOCIM$_0$, CYCLOCIM and OCIM. The CYCLOCIM$_0$ model does not include any penalty on the velocity w. For The subplot in (a) and (c) is the monthly RMSE of potential temperature and salinity from CYCLOCIM in the upper ocean (0 - 500m).

annual average) along 36°S for CYCLOCIM and the WOA2013 observations. The modeled temperature shows a similar seasonal pattern as the observation. In the summer (DJF), the mixed layer is thinnest and strong temperature gradient is in the surface. In fall (MAM), the mixed layer is getting thicker. In winter (JJA), heat is lost, and the mixed layer continues to thicken, becoming thickest in late winter, and the surface stratification disappears. In spring (SON), winds weaken sunlight increases, and the mixed layer start to shrink. The model seasonality is quite similar to that of the observations. Exceptions are along the western boundary currents where the warm and cold anomalies penetrate deeper in the observations than in the model. Such errors are not surprising given the coarsness of the model resolution. I anticipate that these errors will be reduced in the $2° \times 2°$-CYCLOCIM with the dynamic topography constraint provided by satellite altimiter data.

There are also significant improvements to the simulated surface salinity fields as can be seen from Figure 2.8 where I plot the errors averaged over the top 200 m of the water column. Most prominently, large errors in the western part of the subpolar gyre in the North Atlantic ocean present in the steady OCIM state estimate are greatly reduced in the

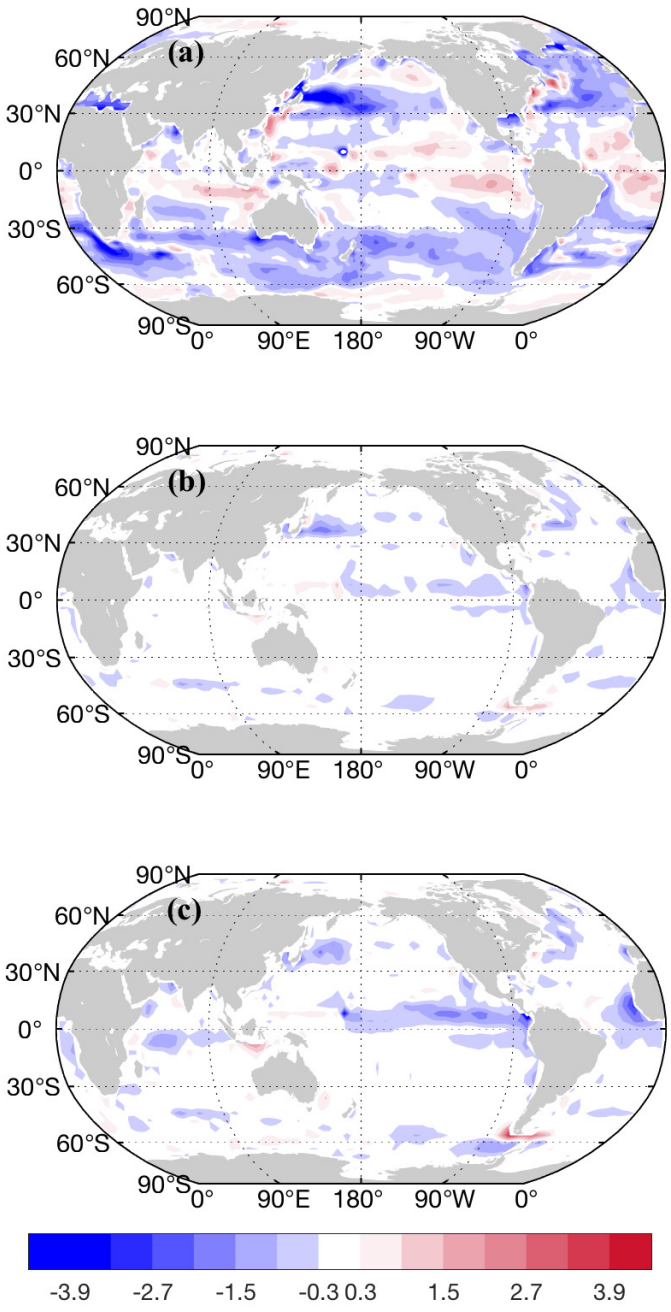

Figure 2.6: Difference between modeled and observed temperature in the upper 200m from OCIM (a), CYCLOCIM$_0$ (b) and CYCLOCIM (c) colored at 0.5 °C interval. The CYCLOCIM$_0$ model does not include the penalty on the vertical velocity.

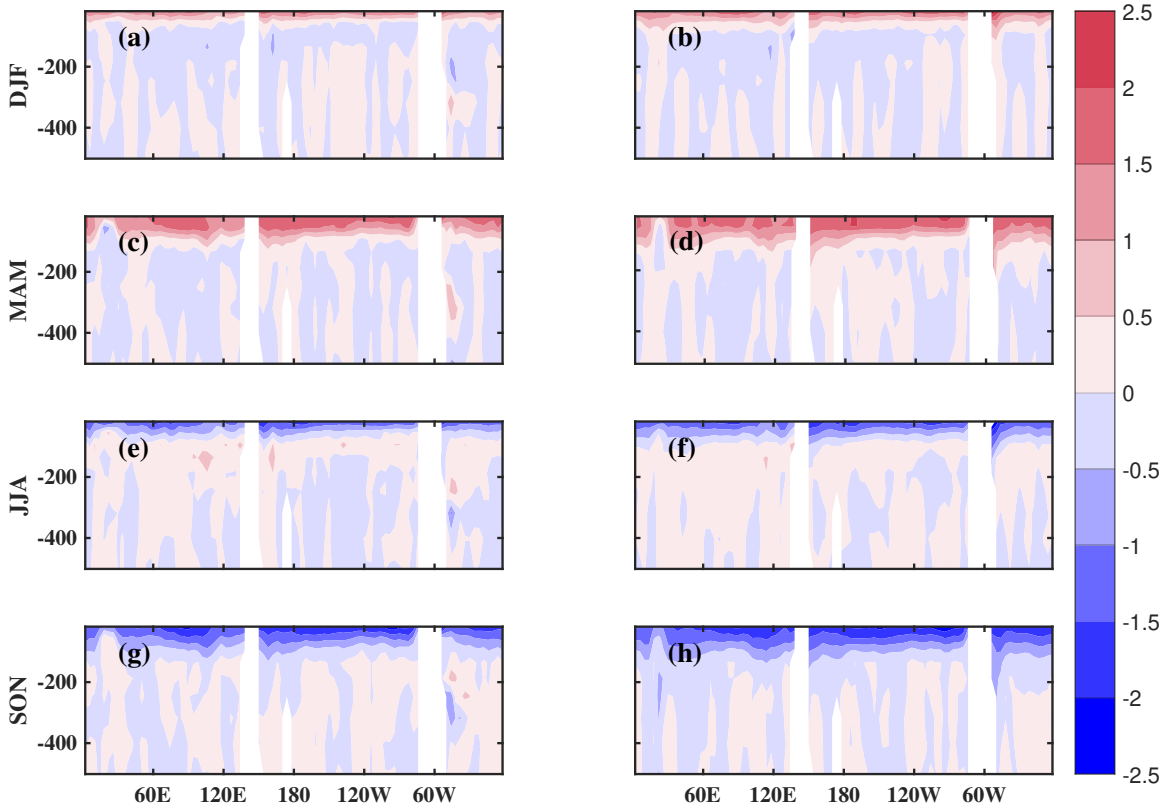

Figure 2.7: The longitude-depth section of the modeled potential temperature abnormaly in comparison with the annual mean along 36°S in CYCLOCIM run from (a) December to February (DJF), (c) March to May (MAM), (e) June to August (JJA) and (g) September to November(SON), and the longitude-depth section of theobserved potential temperature abnormaly in comparison with the annual mean (b) December to February (DJF), (d) March to May (MAM), (f) June to August (JJA)and (h) September to November(SON).

seasonally varying CYCLOCIM state estimate. But the improvements extend over most of the ocean with the exception of the Arctic basin where a uniformly positive salinity bias in OCIM has been replaced by errors that appear more random. A similar positive bias in the Southern ocean for the steady OCIM state estimation has been completely eliminated in the CYCLOCIM state estimate. Globally averaged the RMSE for salinity in the upper 200 m of the water column are reduced from 0.25 g/kg for OCIM to 0.09 g/kg for CYCLOCIM. For the full water column, the improvements are more modest but still significant with an

RMSE error reduced from 0.07 g/kg for OCIM to 0.04 g/kg for CYCLOCIM.

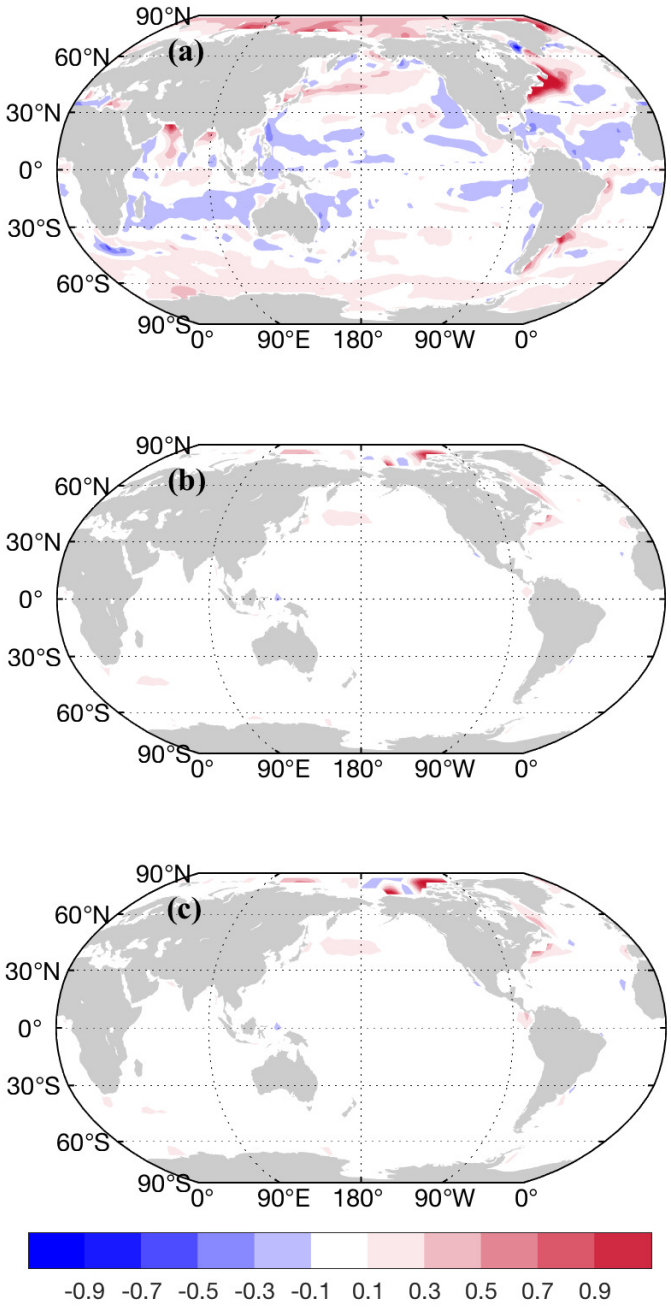

Figure 2.8: Difference between modeled and observed salinity in the upper 200m from OCIM (a), CYCLOCIM$_0$ (b) and CYCLOCIM (c), colored at 0.5 PSU interval. The CYCLOCIM$_0$ model does not include a penalty on the vertical velocity.

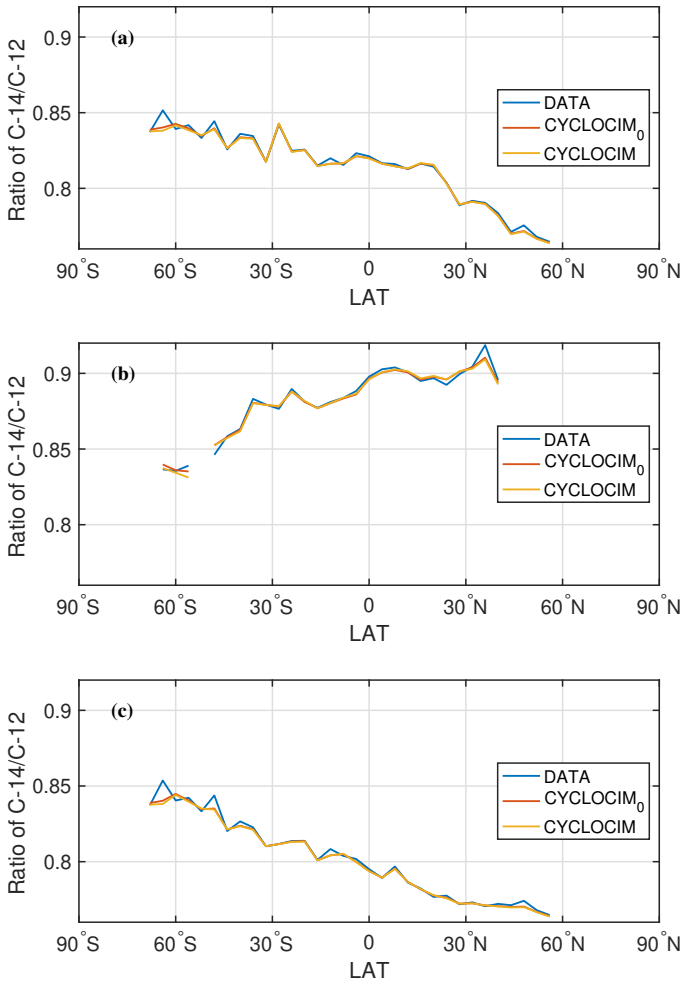

Figure 2.9: The masked zonal mean radiocarbon concentration relative to the pre-industrial atmosphere in CYCLOCIM$_0$ and CYCLOCIM compared to the GLODAPv2 observations. Only grid boxes with radiocarbon observations and no detectable CFCs are included in the basin averages. (a) global ocean, (b) Atlantic ocean and (c) Indian-Pacific ocean. The CYCLOCIM$_0$ model correspons to the one without the penalty on the vertical velocity.

The CYCLOCIM simulation of CFC-11 also provides a better fit to the observed CFC-11 data. The RMSE for surface waters between 0 and 200m is 0.07 pmol/kg for the OCIM state estimate whereas for CYLCOCIM it is 0.04 pmol/kg. In Figure 2.10 I plot the decadal masked zonal averages of CFC-11 and CFC-12 concentrations. Only model grid-boxes with observations during a particular decade are used to construct the averages. The agreement between CYCLOCIM and the observations are generally good. There are however clear decadeal biases at high latitudes in the Southern Ocean where the CYCLOCIM concentrations are too low. Underestimates are also present at high latitudes in the Northern Hemisphere. I tried increasing the scaling by a factor of 10^6 for the precision on the CFCs compared with the other tracers and found a large degradation of the fit to the other tracers with negligible reduction in the model's high latitude biases. These residual errors are consistent with the hypothesis that there has been some significant decadal changes in the ventilation of the ocean at high latitudes (e.g. Waugh et al., 2013; DeVries et al., 2017).

2.5.2 Inferred air-sea fluxes and meridional transport of heat flux and fresh water

In contrast to the OCIM state estimate, I did not use the NCEP heat and fresh water reanalysis product to constrain the CYCLOCIM state estimate. It is therefore interesting to examine how the inferred meridional heat and fresh water transports compare to other data-based estimates. In Figure 2.11 I show the CYCLOCIM estimate of the climatological air-sea heat flux along with the mean meridional heat transport. The pattern and magnitude is very similar to those of the NCEP reanalysis (Large and Yeager, 2009). The ocean gains heat in East Pacific cold tongue region and along the eastern boundaries of the Pacific and Atlantic with magnitude around 150 Wm^{-2}. Heat gained in the tropical regions is transported poleward and is lost in higher latitude. The heat transport peeks at 20°N with value of 2 PW and 20°S with value of 1 PW. The main difference is that our model has a

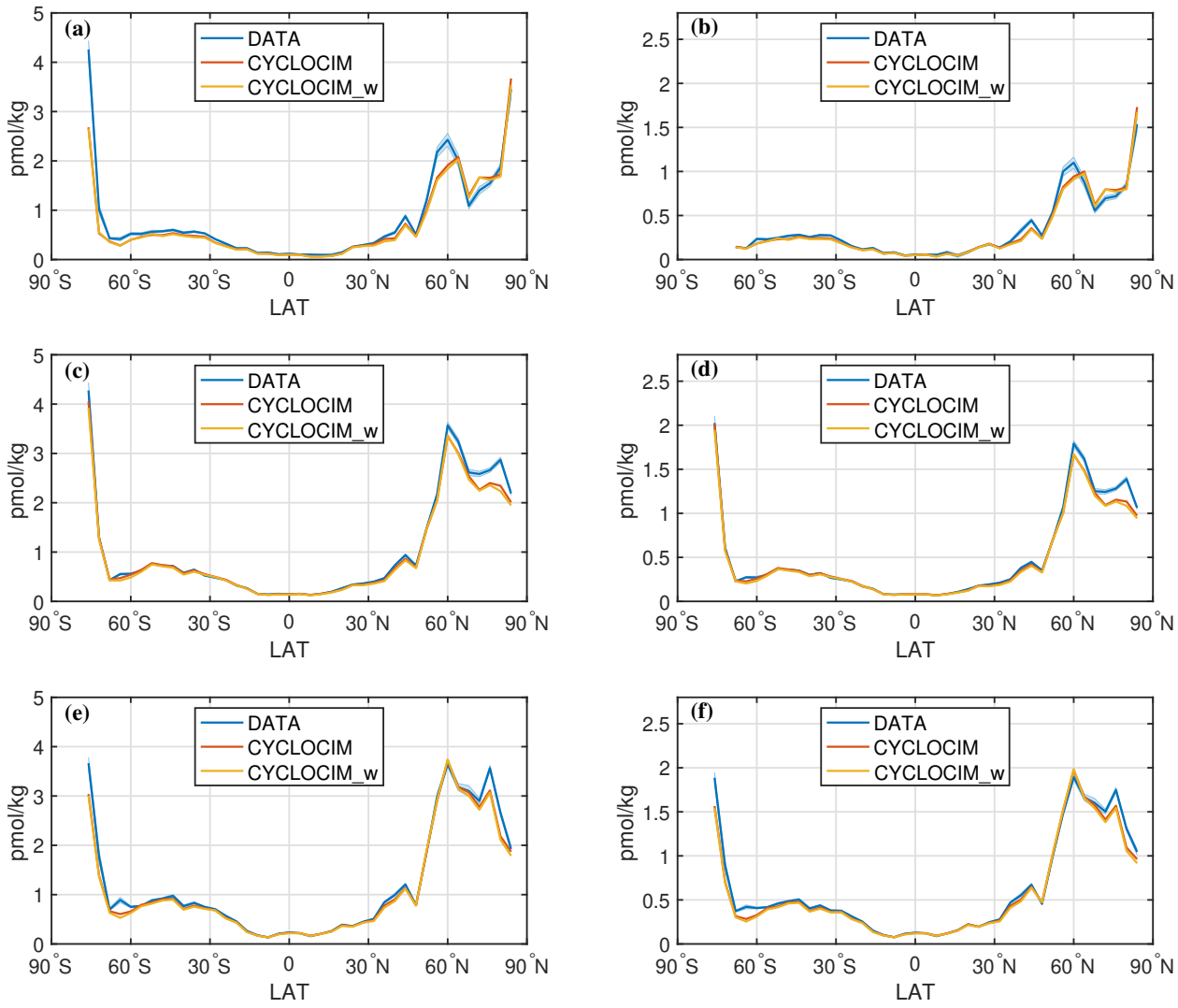

Figure 2.10: The masked zonal mean CFC concentrations for $CYCLOCIM_0$ and CYCLOCIM compared to observations in three decades, panels (a and b) 1980-1989, (c and d) 1990-1999, (e and f) 2000-2009. The 3 panels on the right (a,c, and e) show CFC-11 and the three panels on the left (b,d, and f) show CFC12. The $CYCLOCIM_0$ model does not have a penalty on the vertical velocity. Only model grid boxes with observations in any given decade are used to construct the means. The conresponding number of observations in each decades is: 5991, 19042, 13313 for CFC-11 and 5320, 17962, 13742 for CFC-12. The mean concentration is volume weighted mean concentration, which is integral of concentration times volume by depth and longitude divide by integral of volume by depth and longitude.

weak poleward heat transport in the Southern Ocean, whereas NCEP climatology implies a near zero heat transport. Moreover, the air-sea heat fluxes in the Kuroshio and Gulf Stream regions for the CYCLOCIM state estimate are substantially weaker than those for the NECP

reanalysis. The annually averaged heat loss to the atmosphere in the Gulf Stream region is estimated to be around 50 Wm^{-2}, while in the Labrador Sea the annually averaged heat loss is greater than 300 Wm^{-2}.

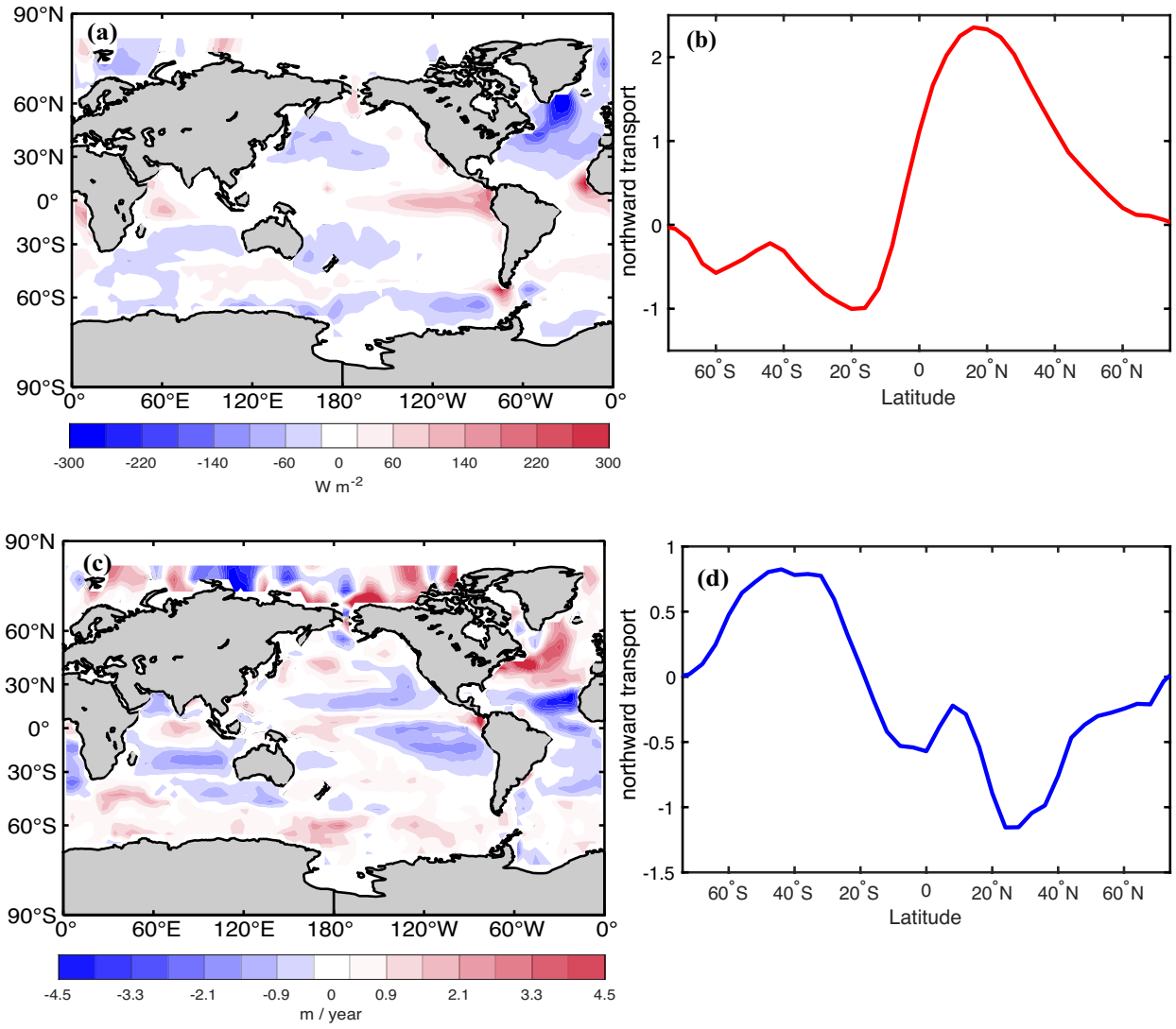

Figure 2.11: Global distribution of climatiogical (a) heat flux, colored at 40 Wm^{-2} intervals with a zero contour, and (c) fresh water flux, colored at 0.5 m/year intervals with a zero contour. (b) Northward ocean heat transports in PW and (d) Northward ocean freshwater transport in Sverdrup (Sv).

The implied annually averaged freshwater transport (Figure 2.11(b)) shows similar pattern as NECP reanalysis data (Large and Yeager, 2009). There is a net evaporation in the

subtropical gyre regions and net precipitation in the intertropical convergence zone (ITCZ) and the sub-polar regions. However, our model estimate predicts weak precipitation in ITCZ with a magnitude around 1 m/year and strong precipitation in gulf stream region and labrador sea with magnitude more than 3 m/year. In summary, without constraining the modeled surface heat flux and freshwater flux using the NECP reanalysis data, the model still produces reasonable heat flux and freshwater flux. It implies that circulation in CYCLOCIM that transports the heat and fresh water is well-grounded.

2.5.3 Meridional overturning circulation

The climatological mean meridional overturning circulation (MOC) is defined as stream function for the zonally integrated meridional volume transport in depth. Positive stream function represent clockwise circulation, and negative stream function represents counter-clockwise circulation. Figure 2.12(a)-(c) shows the implied stream function for CYLCOCIM_0 in the Southern ocean, Pacific ocean and Atlantic ocean. The estimated overturning circulation appears consistent with typical results from prognostic ocean general circulation models, however the strength of the MOC for CYCLOCIM_0 is bigger than expected. For example, maximum of stream function in the Southern Ocean (60 °S) is 40 Sv. In addition, the Pacific ocean and Atlantic ocean both have extreme value in equator at depth 3 km with magnitude of 35 Sv, -35 Sv respectively. Moreover, the vertical velocity, w, from the CYCLOCIM_0 estimate is 10 times bigger than vertical velocity derived from ECCO (Liang et al., 2017). The MOC from the CYLCOCIM state estimate with the penalty on large vertical velocities is shown in Figure 2.12(d)-(e). The maximum of stream function in Southern ocean is now only 30 Sv, and the extreme values in the in Pacific and Atlantic have disappeared.

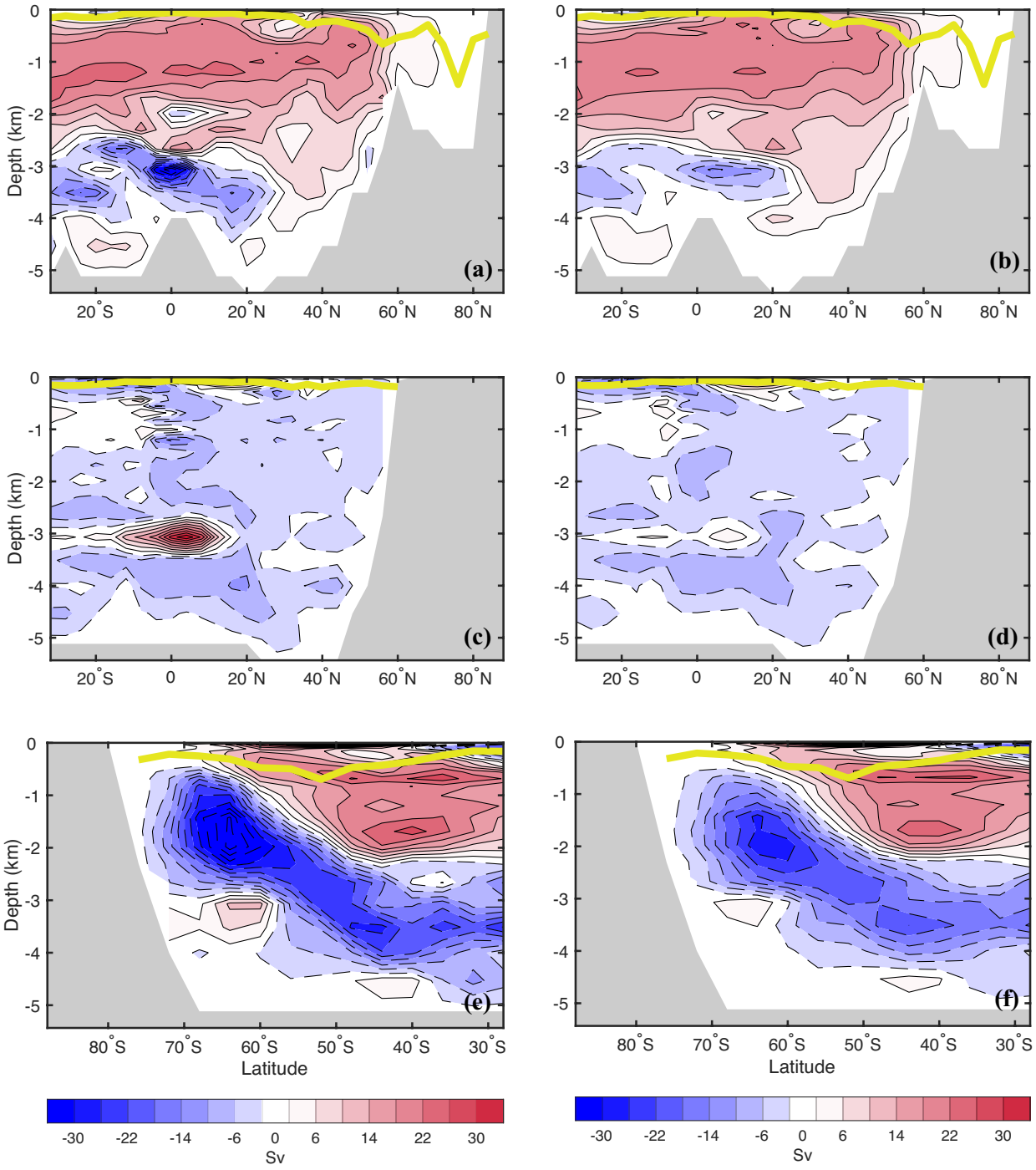

Figure 2.12: Climatogical mean meridional overturning circulation (MOC) stream function in three ocean basins for CYCLOCIM$_0$: (a) Atlantic Ocean (c) Pacific Ocean (e) Southern ocean, and for CYLCOCIM: (b) Atlantic Ocean (d) Pacific Ocean (f) Southern ocean. The contour interval corresponds to 4 Sv..

2.6 Summary and discussion

I have presented the formulation of a 4-D variational assimilation system for estimating the climatological mean seasonal cycle of the residual-mean ocean circulation. The system, which I call CYCLOCIM, assimilates monthly mean temperature and salinity data from the World Ocean Atlas, transient CFC-11 and CFC-12 tracers, and natural radiocarbon measurements for the deep ocean from the GLODAPv2 database. Compared with the majority of existing ocean reanalysis efforts (e.g. Balmaseda et al., 2015, and references therein), what sets our system appart is that it aims to estimate the ocean's mean annual cycle rather than its interanual variability. CYLCOCIM is therefore a generalization to a periodic annual cycle of previous steady-state inversions (e.g. Schlitzer, 1993; Wunsch, 1996; Ganachaud and Wunsch, 2000; Schlitzer, 2007; DeVries and Primeau, 2011). As such, our goal is most similar to the one in the study of Wenzel et al. (2001) who developed a 4-D variational assimilation method to estimate a cyclo-stationary annual cycle of the ocean circulation. There are, however, some important methodological differences. Most importantly, CYCLOCIM produces a state-estimate with zero temporal drift and is therefore completely independent of initial conditions. Initial conditions serve as the main control variables in the study of Wenzel et al. (2001) and most other 4-D variational assimilation studies for the ocean. For CYCLOCIM, I use unresolved eddy-stresses in the horizontal momentum equations together with surface heat, fresh-water, and momentum forcing as the main control variables. In this respect I follow the pioneering study of (Ferreira et al., 2005) who added eddy-stress to initial conditions and surface forcing as the control variables used to minimize solution drift and departures from climatological observations of temperature. In our study I have completely eliminated initial conditions from the list of adjustable parameters by directly solving for the cyclo-stationary annual cycle representative of the model's long-term climatological attractor.

I have demonstrated that our data-constrained model produces an overturning circulation

and meridional heat and fresh water transports that are largely in agreement with existing estimates even though the objective function did not explicitly include such a constraint. This is an improvement compared to our previous steady-state inversions using OCIM for which I included explicit constraints on the meridional heat and fresh water transports in the model's objective function (DeVries and Primeau, 2011). By resolving the seasonal cycle I am also able to produce a much better fit to observation in the upper ocean compared to our previous steady-state OCIM estimates and most of the assimilated variables appear to be in agreement with the observational constraints. One exception is the CFC-11 and CFC-12 tracers. South of 60° the model concentrations are several standard deviations too low for the 1980-1989 and the 2000-2009 period while being in very good agreement for the 1990-1999 period. In the North there are similar low biases but the exact latitude band with the largest biases appear to shift from decade to decade. Decadal variability in the ventilation of the ocean provide a plausible explanation for these errors (e.g. Waugh et al., 2013; DeVries et al., 2017)

The main product of our assimilation system is a set of 12 monthly data-constrained of tracer transport operators for the climatological annual cycle of the ocean circulation. I anticipate that these operators will be particularly useful for global biogeochemical inversions for which there is a need for reliable estimates of the seasonally varying climatological transport of tracers. The solution I presented here is for a version of CYCLOCIM with a $4°\times4°$ resolution, but I are presently optimizing a $2°\times2°$ version of the model. For expediency I also ignored valuable constraints on the dynamic topography of the model provided by satellite altimeter data. I plan on including this constraint in future versions of CYCLOCIM. Another avenue for future work is to produce an ensemble of tracer transport operators drawn from the Bayesian posterior distribution for the eddy-stresses and surface forcing. So far I have only sampled the maximum of the posterior distribution but the development of a computationally efficient means of drawing samples from the posterior should be a high priority for future work.

Chapter 3

Characterizing Stommel's demon using a new data-constrained ventilation diagnostics

3.1 Introduction

The ventilation of the main thermocline is the process that allows for an exchange of water between the mixed layer in contact with the atmosphere and thermocline. It happens where isopycnal surfaces encounters the surface so that water can move along the isopycnal surfaces to/from the interior ocean. The irreversible penetration of water into the main thermocline is called subduction. Seasonally varying mixed layer depth and circulation lead to the net annual subduction of water mass. Iselin (1939) noted that the temperature and the salinity of subsurface thermocline waters match that of late winter surface water rather than the annual mean properties of surface water. It was unclear why only late winter surface water entered the thermocline until Stommel (1979) proposed a hypothesis that the subduction of

water mass into the main thermocline is an intermittent process, happening at the end of winter. In analogy with Maxwell's Demon, Stommel (1979) suggested that during this period, a demon opens the door to allow the end-of-winter properties to flow into the permanent pycnocline. During the rest of the year, the door remains closed. Thus, the process is referred to as "Stommel's demon". Figure 3.1 demonstrates a schematic diagram of "Stommel's

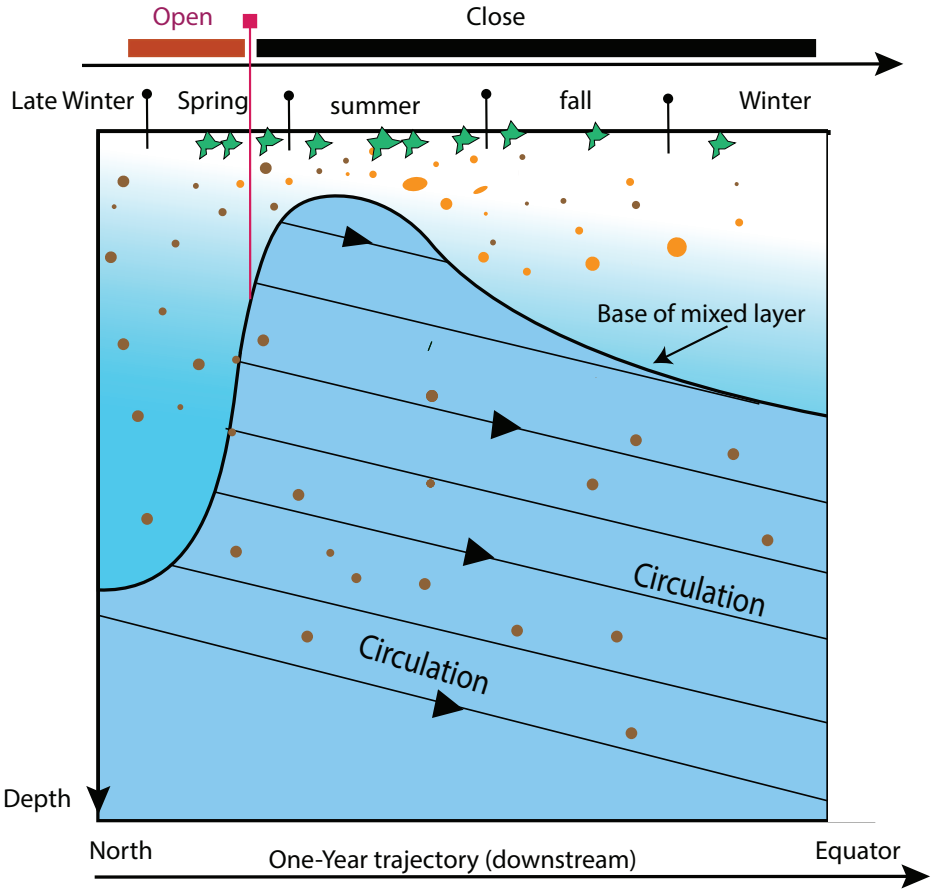

Figure 3.1: One year trajectory of water mass in the subtropical gyre moving northward and downward in the Lagrangian coordinates (Modified from Qiu and Huang (1995)). Brown dot represents the organic matter from last summer is transported to the permanent pycnocline by circulation in early spring. The yellow dot represents the new organic matter created by phytoplankton (green dot) this summer, which will stay in the mixed layer.

demon" in the northern subtropical gyre. Throughout the year, the circulation at the base of the mixed layer moves water mass southward and downward along isopycnal surfaces. During late winter, the mixed layer reaches its annual maximum depth and creates a thick

layer of vertically homogenized water. When spring comes, the rapid shoaling of the deep winter mixed layer leaves the homogenized water behind, which is then subducted into the permanent pycnocline by the large-scale Sverdrop circulation. However, water that is subducted during the summer and fall typically gets re-entrained into the mixed layer when the mixed layer deepens during the late fall and winter. Thus, only late-winter water properties make it into the permanent thermocline.

In addition to subduction, some studies have demonstrated a negative subduction rate in subpolar regions, i.e. a flux of water from the main thermocline to the surface. This process is defined as obduction (Williams et al., 1995; Qiu and Huang, 1995; Liu and Huang, 2011), indicating the effective entrainment from the main thermocline into the mixed layer (see figure 3.2. The mechanism of seasonal obduction is similar to subduction, which is mainly due to the seasonal cycle of mixed layer and circulation. Although water upwells to the surface throughout the whole year, only during a short period, water from the permanent thermocline enters the mixed layer. Most of the water entrained into the mixed layer is the water detained from the mixed layer during the previous year. Therefore, it is necessary to indentify when the effective obduction happens.

To quantify the subduction and obduction process, studies have calculated annual mean subduction rates using a kinematic diagnostic method that integrates the vertical transfer and the shoaling of the mixed layer along the trajectory of the water parcels that were tagged at the base of the mixed layer (Williams et al., 1995; Qiu and Huang, 1995; Kwon et al., 2013; Liu and Huang, 2011). Williams et al. (1995) calculated a subduction rate of 50-100 m/year and a obduction rate of 100-300 m/year in the North Atlantic using a numerical model. Qiu and Huang (1995) revealed similar subduction and obduction rates in the North Atlantic using climatological data. Liu and Huang (2011) produced a global map of annual mean subduction/obduction rate by averaging results from 1959 to 2006 using Simple Ocean Data Assimilation outputs. Kwon et al. (2013) studied the seasonal cycle of the subduction

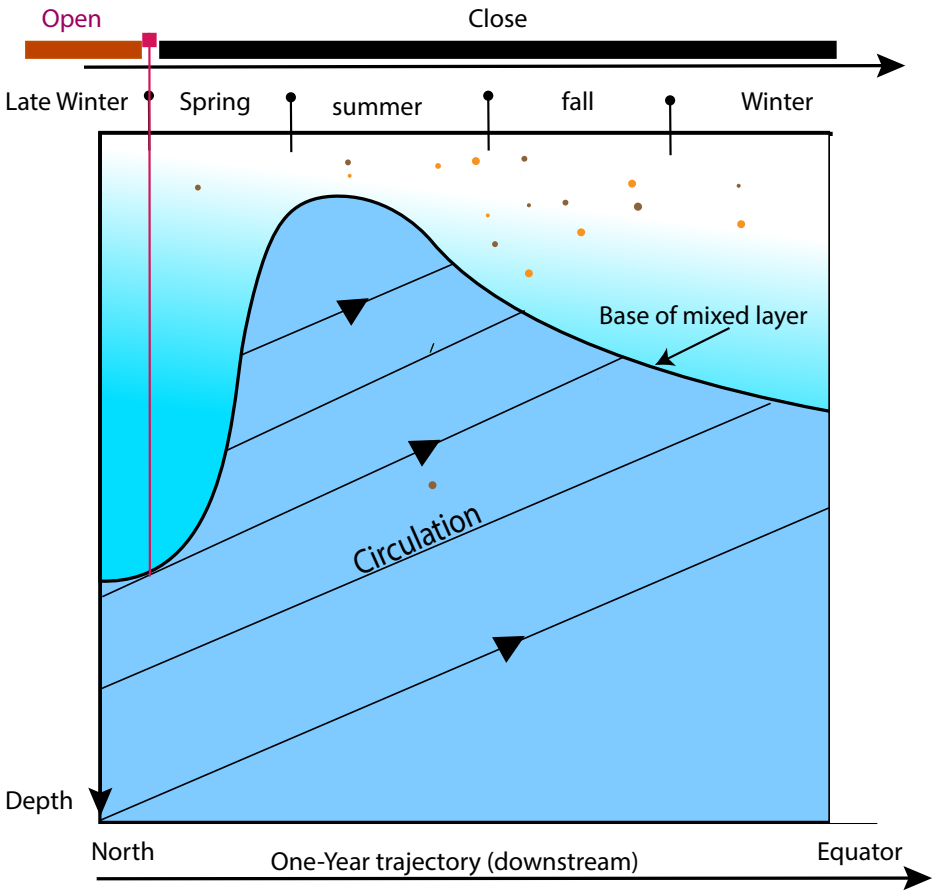

Figure 3.2: One year trajectory of water mass in the subpolar gyre moving northward and upward in the Lagrangian coordinates (Modified from Qiu and Huang (1995)).

rate of the upper ocean water in the Southern Ocean. However, kinematic diagnostics only calculate the net advection of water mass from the surface to the interior ocean. It ignores the diffusion along with the isopycnal layers, which is important for the study of passive tracers. Another limitation of previous studies is that the annual subduction rate can only capture the annual mean signal and thus does not quantify the transfer of seasonally varying tracers between the sea surface and the ocean's interior.

Moreover, some studies have focused on quantifying the periods of effective subduction and obduction, and the definition of the starting time of effective subduction remains unclear in those studies. Some studies assumed that effective subduction starts during the same month (e.g. late winter) in all the regions (Williams et al., 1995; Qiu and Huang, 1995), while others

adopt different starting time-based on the maximal mixed layer depth (Liu and Huang, 2011; Dall'Olmo et al., 2016) or based on the onset of buoyancy forcing in spring(Marshall et al., 1993, 1999). They diagnosed the effective subduction period by integrating the instantaneous subduction along the trajectory of water parcels starting from the prescribed starting month until the overall integral is equal to the annual mean subduction rate. Williams et al. (1995) showed that effective subduction happens approximately mostly during 1 to 2 months in late winter and the effective obduction happens mostly during 1 to 2 months before the end of winter in the North Atlantic. However, Marshall et al. (1993) calculated the subduction period using a different starting month depending on the onset of buoyancy forcing in spring. The effective subduction and obduction period ranged from 2 to 4 months. In conclusion, those studies have demonstrated the existence of a specific period that allows for the exchange between the surface and interior ocean. However, they failed to quantify the effective subduction periods in a consistent way.

In summary, previous studies that have attempted to quantify "Stommel's demon" have two main flaws: (1) they neglected the diffusion along with the isopycnal layers, and (2) they failed to provide an accurate estimate of effective subduction period. Moreover, since the purpose of Stommel's theory is to explain why the temperature and the salinity of subsurface water in the North Atlantic match that of late winter, it is more intuitive to quantify which month the subsurface water mass was last in the mixed layer instead of quantifying which month the water is being fluxed into the interior ocean. Due to the complexity of the circulation, water that subducted at the base of the mixed layer doesn't necessarily form the subsurface water mass, and the subsurface water mass doesn't necessarily originate from the mixed layer directly above it.

In the present study, I develop a new method to address all the above questions. I use the transit time distribution (TTD) method to describe where, in which month and how much of the water at a given location was transported from the surface (subduction) or will be

transported back to the surface (obduction) by the advective and diffusive circulation. The TTD method has been used widely to provide a complementary diagnostic of ventilation process (Holzer and Hall, 2000; Haine and Hall, 2002; Primeau, 2005; Primeau and Holzer, 2006; Haine et al., 2008; Holzer and Primeau, 2010; DeVries and Primeau, 2011). The surface-to-interior TTD is used to quantify the subduction and the interior-to-surface TTD is used to quantify the obduction. The zeroth moment of TTD is the volume fraction of a specific water mass that makes its last or first contact with the surface ocean, and the first moment of TTD is the mean of the transit time distribution, describing the mean travel time for the subduction process (also called age) and the obduction process (also called life expectancy). The method described in the study is the first time to use TTD to obtain which months and what regions of the surface ocean are the most important in terms of subduction and obduction. The detail of the TTD method is described in the method.

The plan of the study is as follows. In section 2, I introduce the new method to quantify the "Stommel demon". First, I use the seasonally varying circulation from CYCLOCIM which represents the best estimate of the advective and diffusive circulation learned from tracer data (See detail in Chapter 2). Second, I introduce two forms of TTD: the surface-to-interior TTD for subduction, and the interior-to-surface TTD for obduction. Last, I develop a periodic solver that enables efficient calculation of the zeroth and first moments of TTDs without direct calculation of the full distribution, which avoids thousands of years' time-stepping the transport equation. Sections 3 presents the map of the volume fraction of subduction and obduction in 12 months. Section 4 discusses the results and further application.

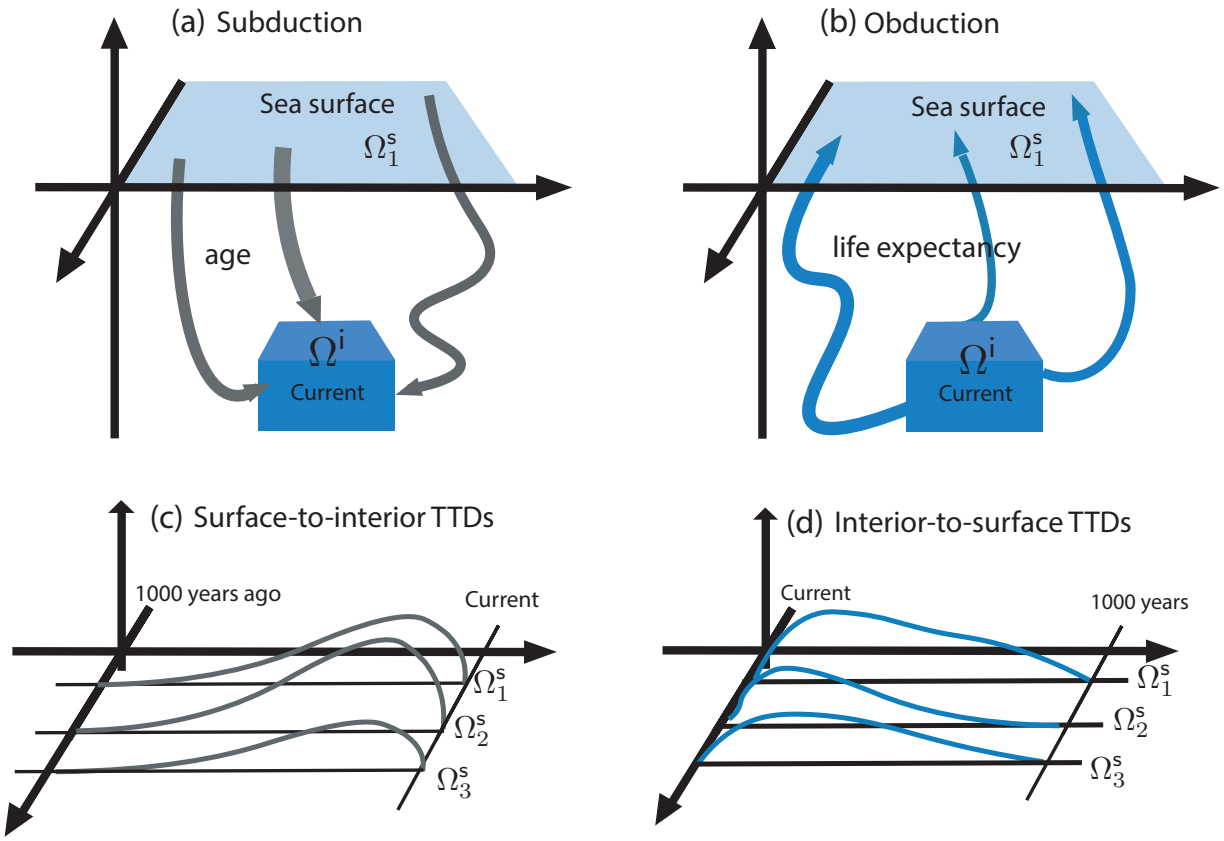

Figure 3.3: A schematic diagram of subduction(a) and obduction process(b), the surface-to-interior TTDs(c) and the interior-to-surface TTDs(d). The upper panels give a schematic representation of the process of subduction and obduction. Note that the mean time for water parcels to travel from surface,Ω_1^s, to the interior box, Ω^i, is referred as age. The mean time for water parcels to travel from the interior box, Ω^i, back to the surface ,Ω_1^s, is defined as life expectancy. The bottom panels are schematic representation of the surface-to-interior TTDs and the interior-to-surface TTDs at three surface patches $\Omega_1^s, \Omega_2^s, \Omega_3^s$. The TTD provides a quantitative description of the distribution of times for water to travel between the surface and interior ocean.

3.2 Method

3.2.1 Transit-time distribution (TTD)

Water parcels are transported through many advective and diffusive pathways with a multiplicity of transit times. The figure 3.3 (a) and (b) are the schematic diagrams of the subduction and obduction processes between a interior box, Ω^i, and a surface patch, Ω_1^s.

The transport of water between the surface patch Ω_1^{s} and the interior box Ω^{i} is described by a continuous distribution of transit-times, called transit-time distribution (TTD). Based on the direction of the pathway, figure 3.3(c) is the surface-to-interior TTD (also called the last-passage time distribution), indicating the subduction process, and figure 3.3(d) is the interior-to-surface TTD (also called first-passage time distribution), indicating the obduction process (Primeau, 2005). Note that there could be multiple TTDs corresponding to different surface patches for one interior box, e.g $\Omega_1^{\mathsf{s}}, \Omega_2^{\mathsf{s}}, \Omega_3^{\mathsf{s}}$.

Figure 3.4 is a schematic describing how to calculate the surface-to-interior TTD at a given location, Ω^{i}, and at given time, t, using the boundary impulse response (BIR) in a forward tracer equation. Here I inject one unit of tracers at a given surface patch, Ω_j^{s}, and record the evolution of tracer concentration at Ω^{i}, which is called BIR (Haine et al., 2008). Using a sequence of tracers injecting at a sequence of time, the TTD can be computed by the cut through the BIRs in the horizontal direction at the response time $\mathbf{t} = t$ (figure 3.4). Therefore, the surface-to-interior TTD is a function of transit-time τ that weights the contributions from the surface at all past times $t - \tau$ until time t. A more thorough explanation of the origin of TTD is described in Haine et al. (2008). Note the transit-time τ starts from 0 to infinity ∞, meaning that I need to calculate the BIRs in infinite times. Therefore, in section 3.3.2 and 3.3.3, I use CYCLOCIM adjoint model combined with a Newton-krylov solver to calculate the moments of the complete TTD effeciently.

The surface-to-interior TTD can be used to propagate the boundary conditions at a given surface patch Ω_k^{s} to a given interior box Ω^{i}. The tracer state of an interior ocean box is the convolution integral of the TTDs for all the surface patches and the surface boundary conditions. Mathematically, let's assume $C(\Omega^{\mathsf{i}}, t)$ is the concentration of tracer at location Ω^{i} and time t, which satisfies the tracers advection-diffusion equation. $C_s(\Omega_k^{\mathsf{s}}, t - \tau)$ is the surface boundary condition at surface patch Ω_k^{s} and time t. Therefore, the $C(\Omega^{\mathsf{i}}, t)$ can be

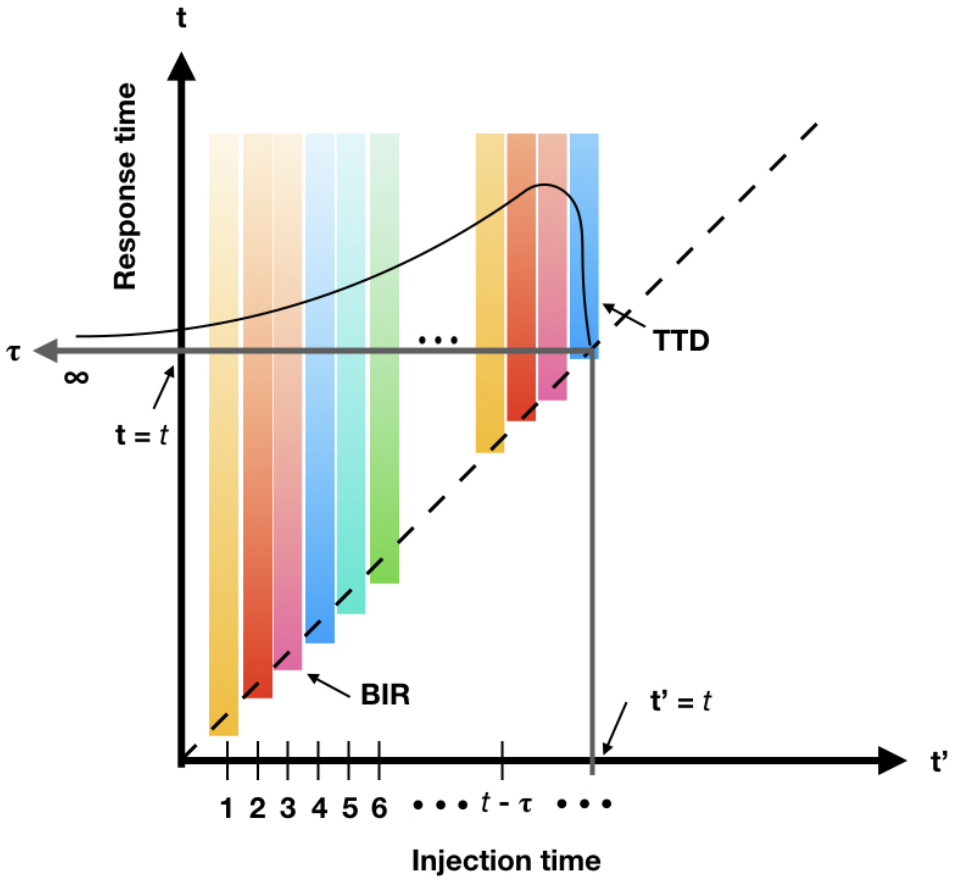

Figure 3.4: A schematic diagram showing how to calculate the surface-to-interior TTD at a given location, Ω^{i}, and time, t, using a sequence of boundary impulse responses (BIRs) computed using forward tracer equation. The x-axis represents the time of tracer injection, $\mathbf{t}$, and the y-axis represents the response time, $\mathbf{t}'$. τ is the transit-time (elapsed time). Each color bar represents a BIR that conresponds to a injected tracer at each time (x-axis). The TTD at time t corresponds to a cut through the BIRs in the horizontal direction at response time $\mathbf{t} = t$. Note the x-axis of TTD is τ, which starts from 0 to the infinity, ∞. The integral of TTD is equal to one.

written as:

$$C(\Omega^{\mathrm{i}}, t) = \sum_{k=1}^{n} \int_0^{\infty} \mathcal{G}(\Omega^{\mathrm{i}}, \Omega_k^{\mathrm{s}}, t, t-\tau) C_s(t-\tau) d\tau, \tag{3.1}$$

where $\mathcal{G}(\Omega^{\mathrm{i}}, \Omega_k^{\mathrm{s}}, t, t-\tau)$ is the TTD that propagates surface concentration C_s at time $t-\tau$ and surface patch Ω_k^{s}, to the interior box Ω^{i} at time t. n is the number of the surface patches.

$\int_0^\infty \mathcal{G}(\Omega^{\mathsf{i}}, \Omega_k^{\mathsf{s}}, t, t-\tau)d\tau$ is the zeroth moment of the surface-to-interior TTD, indicating the volume fraction of the water at (Ω^{i}, t) that originated from the surface patch Ω_k^{s}. The first moment of the TTD, $\int_0^\infty \mathcal{G}(\Omega^{\mathsf{i}}, \Omega_k^{\mathsf{s}}, t, t-\tau)\tau d\tau$, divided by its zeroth moment is the mean age of the water, which is defined as the mean time elapsed since the fluid parcel made its last contact with the surface patch Ω_k^{s} without making contact with other surface patches $\Omega_{k'}^{\mathsf{s}}$, where $k' \neq k$ (Primeau, 2005). In the present study, I use a CYCLOCIM adjoint transport model to propagate the tracers from the interior ocean backward to the surface and thus compute the surface-to-interior TTD (see details in 3.2.2).

The interior-to-surface TTD, $\mathcal{G}^\dagger$, describes the time evolution of how the circulation transports the water back to the surface ocean. $\mathcal{G}^\dagger(\Omega^{\mathsf{i}}, \Omega_k^{\mathsf{s}}, t, t-\tau)$ is the TTD that transport the interior properties concentration $C(\Omega^{\mathsf{i}}, t)$ back to the surface at time $t+\tau$. The zeroth moment of interior-to-surface, $\int_0^\infty \mathcal{G}^\dagger(\Omega^{\mathsf{i}}, \Omega_k^{\mathsf{s}}, t, t-\tau)d\tau$, is the volume fraction of the water at (Ω^{i}, t) that make the first contact with the surface patch Ω_k^{s} without making contact with other surface patches $\Omega_{k'}^{\mathsf{s}}$, where $k' \neq k$. The first moment of interior-to-surface TTD, $\int_0^\infty \mathcal{G}^\dagger(\Omega^{\mathsf{i}}, \Omega_k^{\mathsf{s}}, t, t-\tau)\tau d\tau$, divided by its zeroth moment is the remaining life expectancy of the water at (Ω^{i}, t) before it returns back to the surface patch Ω_k^{s} (Primeau, 2005). To calculate the interior-to-surface distribution, I use a CYCLOCIM forward transport model that propagates the tracer at the interior box to the surface (see detail in 3.2.2).

3.2.2 Forward and adjoint transport model

In this section, I design a forward model and a adjoint (backward) model using the monthly transport operators $\mathbf{\Gamma}$ obtained from the CYCLOCIM (see details in Chapter 2) to calculate the TTD. The details of the models are listed below.

Governing equation

The governing equation for the time evolution of a tracer without source term is given by

$$\begin{cases} \dfrac{\partial}{\partial t} C(\mathbf{r},t) + \nabla \cdot \left[\mathbf{u}^{\dagger} - \mathbf{K} \cdot \nabla\right] C(\mathbf{r},t) = 0, \\ \qquad\qquad\qquad\qquad\qquad\qquad C(\mathbf{r},0) = C_0(\mathbf{r}), \end{cases} \tag{3.2}$$

where $\mathbf{u}^{\dagger}(\mathbf{r},t)$ is the residual mean fluid velocity field and $\mathbf{K}(\mathbf{r},t)$ is the eddy-diffusion tensor. Therefore, The spatially discretized version of the tracer transport problem can be written as follows:

$$\begin{cases} \dfrac{d}{dt}\mathbf{c}(t) + [\mathbf{\Gamma}(t)]\,\mathbf{c}(t) = 0, \\ \qquad\qquad\qquad\qquad \mathbf{c}(0) = \mathbf{c}_o, \end{cases} \tag{3.3}$$

where $\mathbf{\Gamma}(t) = \mathbf{\Gamma}(t+T)$ is a time-periodic sparse $N \times N$ matrix operator obtained from CYCLOCIM with N equal the total number of gridboxes in the model.

To keep track of where and when fluid elements in the interior of the ocean were last in contact with the sea surface I add a rapid linear loss term in the top layer of the model, which I implement using a linear operator:

$$\mathbf{\Lambda} = \lambda \mathbf{diag}(\mathbf{\Omega^s 1}), \tag{3.4}$$

where λ is the loss rate and $\mathbf{\Omega^s}$ is a diagonal matrix with 1 for grid box in the top layer of the model and zeros otherwise. Therefore, the tracer transport equation subject to a zero Dirichlet boundary condition at the sea surface, which I implement here with the linear loss

operator is

$$\begin{cases} \dfrac{d}{dt}\mathbf{c}(t) + [\mathbf{\Gamma}(t) + \mathbf{\Lambda}]\,\mathbf{c}(t) = 0, \\ \qquad\qquad\qquad\qquad \mathbf{c}(t_0) = \mathbf{c}_o. \end{cases} \tag{3.5}$$

Masks

To describe the transport time-scales to and from the sea surface in the numerical model, it is convenient to define mask vectors of zeros and ones, some of which isolate particular regions of interest in the interior of the ocean and others that partition the surface of the ocean. The surface masks cover the upper-most layer of the model with m non-overlaping patches implemented as m column vectors of length N which I arrange into the columns of an $N \times m$ matrix.

$$\mathbf{\Omega}^{\mathsf{s}} = \left[\begin{array}{cccccc} \boldsymbol{\omega}^{\mathsf{s}}{}_1 & \cdots & \boldsymbol{\omega}^{\mathsf{s}}{}_k & \cdots & \boldsymbol{\omega}^{\mathsf{s}}{}_m, \end{array} \right], \tag{3.6}$$

with the elements of $\boldsymbol{\omega}^{\mathsf{s}}{}_k$ equal to 1 for grid-boxes in the k-th surface patch and equal to 0 otherwise. If I sum the rows of $\mathbf{\Omega}^{\mathsf{s}}$ by multiplying on the right by an $m \times 1$ column vector of 1's, I will obtain a vector that is equal to 1 for surface grid boxes and zero otherwise.

For the interior regions of interest I consider n potentially overlapping regions described by n column vectors of length N which I arrange into the columns of an $N \times n$ matrix

$$\mathbf{\Omega}^{\mathsf{i}} = \left[\begin{array}{cccccc} \boldsymbol{\omega}^{\mathsf{i}}{}_1 & \cdots & \boldsymbol{\omega}^{\mathsf{i}}{}_k & \cdots & \boldsymbol{\omega}^{\mathsf{i}}{}_n, \end{array} \right], \tag{3.7}$$

with the elements of $\boldsymbol{\omega}^{\mathsf{i}}{}_k$ equal to 1 for grid-boxes in the m-th interior region and equal to 0 otherwise.

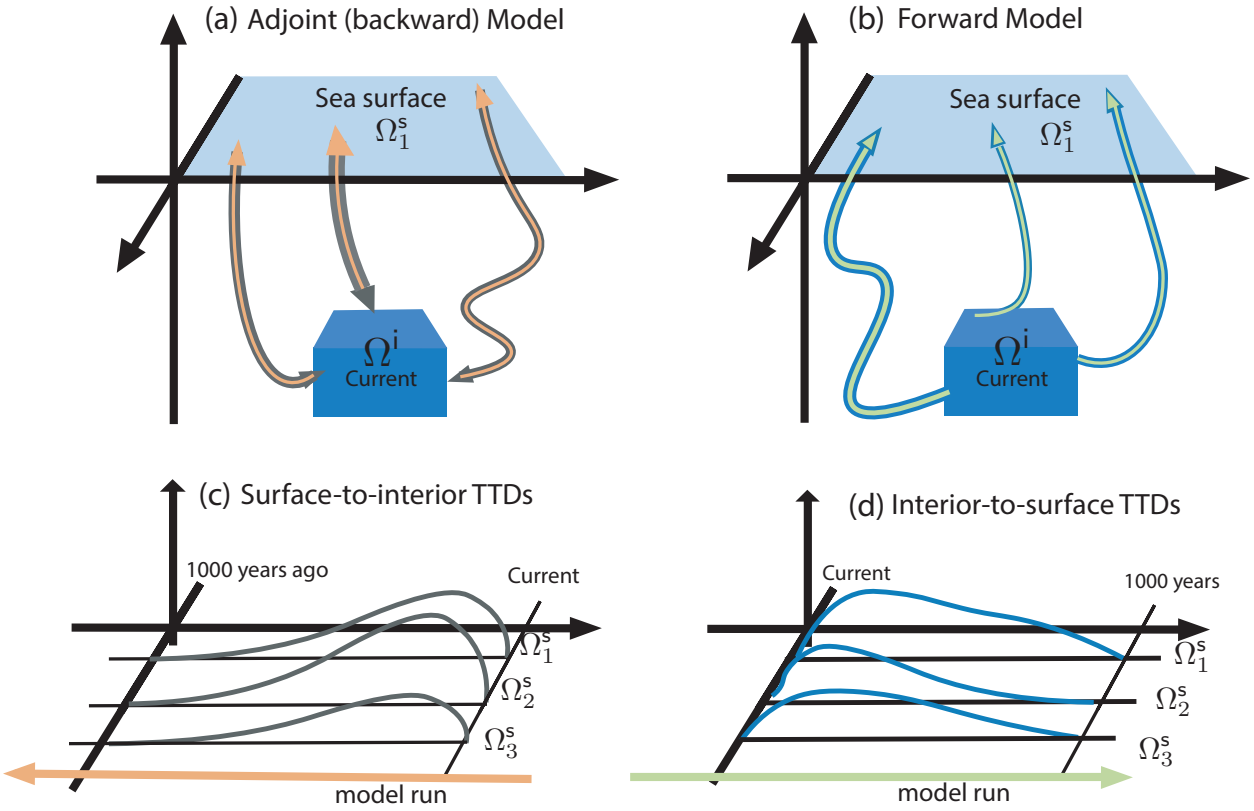

Figure 3.5: The left panels are the process of calculating the surface-to-interior TTDs (c) using adjoint(backward) model (a), which is transporting the water parcel backward using reverse circulation starting from current time to few thousands year ago. The right panels are the process of calculating the interior-to-surface TTDs (d) using forward model (b), which is transporting the water parcel forward for few thousands of years. The TTDs record the fraction and time spent of the water parcels once it arrives at the surface patches.

Forward model

To compute the interior-to-surface TTD, I inject a unit amount of tracer in interior box $\mathbf{\Omega}^i$ at time t, and let model run forward (see figure 3.5(b) and (d)). Once a labelled water parcel returns to the surface, its tracer label is removed. In the process I record how much tracer label is removed at each time so as to determine the distribution of transit-time.

The concentration of tracer in each interior region immediately after injection is equal to the reciprocal of the volume within each region. The initial conditions are therefore obtained by rescaling the n columns of $\mathbf{\Omega}^i$ by multiplying from the right by the inverse of an $n \times n$

diagonal matrix formed from the total volume contained in each region:

$$\mathbf{c}(t) = \mathbf{\Omega^i diag}(\mathbf{\Omega^{i\prime} V \Omega^i})^{-1}. \tag{3.8}$$

The time evolution of an initial tracer distribution $\mathbf{c(t)}$ is given by:

$$\mathbf{c}(t+\tau) = \mathbf{\Phi}(t+\tau, t)\mathbf{c}(t) \tag{3.9}$$

where $\mathbf{\Phi}$ is the state transition matrix given by the solution to:

$$\begin{aligned} \frac{\partial}{\partial \tau}\mathbf{\Phi}(t+\tau;t) + \left[\mathbf{\Gamma}(\tau+t) + \mathbf{\Lambda}\right]\mathbf{\Phi}(t+\tau;t) = 0, \\ \mathbf{\Phi}(t;t) = \mathbf{I}. \end{aligned} \tag{3.10}$$

Here τ represents the time elapsed since water parcel is transported away from the interior box $\mathbf{\Omega^i}$. In the forward transport model, the time step $\Delta\tau$ is one month. $\mathbf{\Phi}(t+\tau;t)$ is the state matrix of tracer at time $t+\tau$.

Therefore, propagating the initial condition in each interior box defined by $\mathbf{\Omega^i}$ forward for thousands of years and computing the loss rate of tracer from each surface patch in $\mathbf{\Omega^s}$ yields $\boldsymbol{\phi}^{\uparrow}(\tau|t)$:

$$\begin{aligned} \boldsymbol{\phi}^{\uparrow}(\tau|t) &= \mathbf{\Omega^{s\prime} V \Lambda \Phi}(t+\tau|t)\mathbf{c}(t), \\ &= \mathbf{B\Phi}(t+\tau|t)\mathbf{c}(t), \end{aligned} \tag{3.11}$$

where $\mathbf{c}(t)$ is the intial condition and $\mathbf{B} \equiv \mathbf{\Omega^{s\prime} V \Lambda}$ is surface loss term.

The $\boldsymbol{\phi}^{\uparrow}(\tau|t)$ is a $m \times n$ matrix where column index j conresponds to the interior box $\mathbf{\Omega^i}_j$ and row index i conresponds to the surface patch $\mathbf{\Omega^s}_i$. Each element in the $\boldsymbol{\phi}^{\uparrow}(\tau|t)$ is the fraction of water that originated from interior box defined at column j and is transported to the surface patch defined at row i wit a transit time τ. Summing over column indices and

integrating over τ yields an $1 \times n$ row vector of 1's because the unit amount of tracer injected in each of the n interior regions eventually leaves the ocean via one of the m surface patches. Note that if the regions of interest are in the upper ocean, the above equation should be solved for several values of $t \in [0, T]$ to resolve the seasonal cycle. Otherwise, t can be any month in the present study.

Therefore, I can simply run the forward model thousands of simulation years until the inkected tracer is completely removed from the surface. The calculated $\boldsymbol{\phi}^{\uparrow}(\tau)_{i,j}$ at each time τ records the interior-to-surface TTD of tracers that originated from the interior box $\boldsymbol{\Omega}^{\mathsf{i}}{}_j$ and transported to the surface patch $\boldsymbol{\Omega}^{\mathsf{s}}{}_i$.

Backward model

To obtain the surface-to-interior TTD, I build the adjoint (backward) model, which transport the tracer by the time-reversed adjoint circulation. Therefore, the tracer in interior box will be transported backward to its source region in the opposite direction of its original trajectory (See figure 3.5 (a) and (c)). Once the water parcel returns back to the surface, the tracer label is removed. We record the removed rate to construct the TTD. Therefore, the tracer state of at time t can related to the tracer state at time $t - \tau$ $\mathbf{c}(\mathbf{t})$, is given by:

$$\mathbf{c}(t-\tau) = \boldsymbol{\Phi}^{\dagger}(t-\tau, t)\mathbf{c}(t), \tag{3.12}$$

where $\boldsymbol{\Phi}$ is the state transition matrix given by the adjoint transport model:

$$\begin{aligned} \frac{\partial}{\partial \tau}\boldsymbol{\Phi}^{\dagger}(t-\tau;t) + \left[\boldsymbol{\Gamma}^{\dagger}(t-\tau) + \boldsymbol{\Lambda}\right]\boldsymbol{\Phi}^{\dagger}(t-\tau;t) = 0, \\ \boldsymbol{\Phi}^{\dagger}(t;t) = \mathbf{I}. \end{aligned} \tag{3.13}$$

Here $-\tau$ represent the age. Therefore, if I integrate the equation backward for a certain amount of time τ, the resulting $\boldsymbol{\Phi}^{\dagger}(t-\tau;t)$ will be the ocean state in τ years ago. Note $\mathbf{V}(t)$

is a diagonal matrix formed from the model grid-box volumes and

$$\mathbf{\Gamma}^{\dagger}(t) \equiv \mathbf{V}^{-1}\mathbf{\Gamma}'(t)\mathbf{V}. \tag{3.14}$$

Therefore, similar to the forward model, the surface-to-interior TTDs can obtained by propagating the initial condition in each interior box defined by $\mathbf{\Omega}^{\mathsf{i}}$ backward for thousands of years and computing the loss rate of tracer from each surface patch in $\mathbf{\Omega}^{\mathsf{s}}$:

$$\begin{aligned} \boldsymbol{\phi}^{\downarrow}(\tau|t) &= \mathbf{\Omega}^{\mathsf{s}\prime}\mathbf{V}\mathbf{\Lambda}\mathbf{\Phi}^{\dagger}(t-\tau|t)\mathbf{\Omega}^{\mathsf{i}}\mathbf{diag}(\mathbf{\Omega}^{\mathsf{i}\prime}\mathbf{V}\mathbf{\Omega}^{\mathsf{i}})^{-1}, \\ &= \mathbf{B}\mathbf{\Phi}^{\dagger}(t-\tau|t)\mathbf{c}(t). \end{aligned} \tag{3.15}$$

Figure 3.6 shows $\Phi^{\downarrow}(\tau|0)$ computed using CYCLOCIM, where the interior box $\mathbf{\Omega}^{\mathsf{i}}$ is the global ocean below the 200m and the surface patch $\mathbf{\Omega}^{\mathsf{s}}$ is the North Hemisphere (figure 3.6(a) and (c)) and the Southern Hemisphere (figure 3.6(b) and (d)). In the experiment, 46% of the water in the interior ocean is subducted from the surface Northern Hemisphere and 54% from the surface Southern Hemisphere. Figure 3.6 (a)-(b) show that most of the water in the interior ocean comes 1000 year ago (72%). However, the water coming from the Southern Hemisphere is younger than the Northern Hemisphere, since the curve in 3.6(b) is more right skewed than 3.6(a). By zooming in the most recent 20 years, the subduction in both hemisphere shows strong seasonality (Figure 3.6(c) and (d)), however, with opposite phase. Therefore, by calculating the surface-to-interior TTD, I can study where and in which month and how much of the water in the main thermocline is subducted from the surface. However, it is computationally expensive to run the forward and the backward model directly for thousands of simulation years until the injected tracer is completely removed from the surface. Therefore, I develop an efficient method that takes advantage of the periodic flow to calculate the zeroth and first moment of TTD in section 3.2.3.

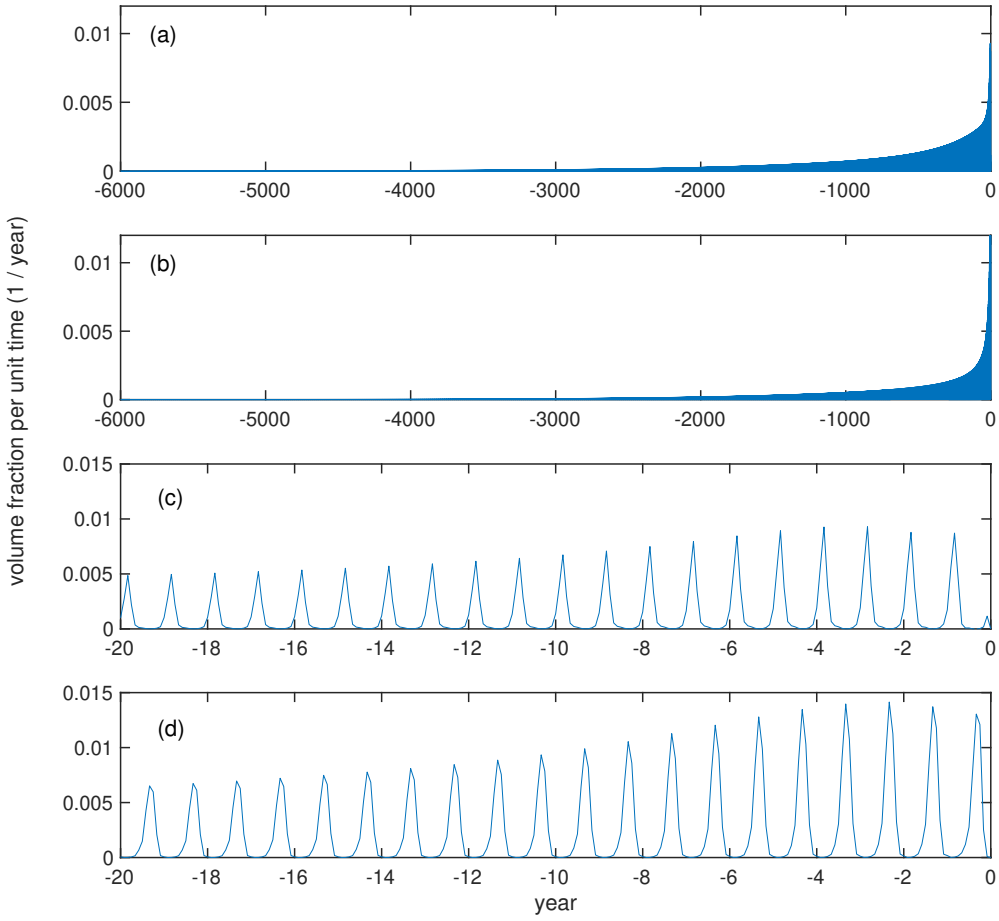

Figure 3.6: An example of the surface-to-interior TTD, where the interior box $\mathbf{\Omega}^{\mathrm{i}}$ is the global ocean below 200m, and the surface patch $\mathbf{\Omega}^{\mathrm{s}}$ is the North Hemisphere ((a) and (c)) and the Southern Hemisphere ((b) and (d)). The x-axis represents when the water was last contact with the surface, which is also called the age of the water, and y-axis represents the volume fraction of the water per unit of time. (a) and (b) shows the TTD for 6000 years run with the time step, 1 month. (c) and (d) shows water enter the interior ocean in the most recent 20 years.

3.2.3 Direct computation of moments of TTD using Newton krylov solver

The periodicity of the flow implies that ventilation function is also periodic:

$$\boldsymbol{\phi}^{\downarrow}(\tau|t) = \boldsymbol{\phi}^{\downarrow}(\tau + T|t + T), \tag{3.16}$$

which means that I need only consider times t in the interval $[0, T]$ or $[-T, 0]$ in order to completely characterise the ventilation. Therefore, I take advantage of the periodicity of the ventilation and derives a effecient way to obtain the moments of TTD. The devried equation is shown below.

Moments of the interior-to-surface TTDs

Volume fraction. The volume fraction of the water at time t in each region defined by the n masks in $\boldsymbol{\Omega}^{\mathsf{i}}$ that make first contact with the surface patches defined by the m masks in $\boldsymbol{\Omega}^{\mathsf{s}}$ is given by a $m \times n$ matrix:

$$\begin{aligned} \left\langle \tau^0 | t \right\rangle^{\uparrow} &\equiv \int_0^{\infty} \tau^0 \boldsymbol{\phi}^{\uparrow}(\tau|t)\, d\tau \\ &= \int_0^{T} d\tau \left\{ \mathbf{B}\boldsymbol{\Phi}(t + \tau|t)\mathbf{Q}_0(t) \right\} \end{aligned} \tag{3.17}$$

and the volume fraction of water that returns back to the surface in each month i:

$$\left\langle \tau^0 | t \right\rangle_i^{\uparrow} = \int_{(i-1)\Delta t}^{i\Delta t} d\tau \left\{ \mathbf{B}\boldsymbol{\Phi}(t + \tau|t)\mathbf{Q}_0(t) \right\} \tag{3.18}$$

where

$$\left[\mathbf{I} - \boldsymbol{\Phi}(t + T|t) \right] \mathbf{Q}_0(t) = \mathbf{c}(t) \tag{3.19}$$

can be solved using an iterative newton Krylov solver (Kelley (2013) see details in Chapter 2)

Partitioned mean life expectancy The mean life expenctancy of the water-mass fraction in each of the n interior region at time t that make first contact with the m surface patch at each month i is given by a $m \times n$ matrix:

$$a_i^{\uparrow}(t) = \frac{\langle \tau^1 | t \rangle_i^{\uparrow}}{\langle \tau^0 | t \rangle_i^{\uparrow}} \tag{3.20}$$

where $\langle \tau^1 | t \rangle_i$ is:

$$\begin{aligned} \left\langle \tau^1 | t \right\rangle_i^{\uparrow} &\equiv \int_0^{\infty} \tau \boldsymbol{\phi}^{\uparrow}(\tau | t)\, d\tau \\ &= \int_{(i-1)\Delta t}^{i\Delta t} d\tau \mathbf{B}\boldsymbol{\Phi}(t+\tau|t) \left\{ \tau \mathbf{Q}_0(t) + T\boldsymbol{\Phi}(t+T|t)\mathbf{Q}_1(t) \right\} \end{aligned} \tag{3.21}$$

where

$$\left[\mathbf{I} - \boldsymbol{\Phi}(t+T|t) \right] \mathbf{Q}_1(t) = \mathbf{Q}_0(t), \tag{3.22}$$

can be solved using the Newton-Krylov solver.

In summary, the main procedure to compute the water mass fraction that make its first contact with surface ocean and its life expectancy using adjoint model is:

1. Define the set of interior region ($\mathbf{\Omega}^{\mathsf{i}}$) and surface patch masks ($\mathbf{\Omega}^{\mathsf{s}}$)

2. Define initial condition $\mathbf{c}(t)$ at time t. If the regions of interest are in the upper ocean the above equation should be solved for several values of $t \in [0, T]$ to resolve the seasonal cycle. Otherwise, the result TTD in deep ocean box will be similar by starting with any time.

3. Using an iterative Newton Krylov solver solve for $\mathbf{Q}_0(t)$ from the Eq. 3.19 and solve for $\mathbf{Q}_1(t)$ from the the Eq. 3.22.

4. Perform a sequence of forward model runs starting at t to different times $t + \tau_k$ for $k = 0, \cdots 11$ with $\tau_k = k\Delta\tau$. Therefore, the fraction of water mass and its age in interior box $\mathbf{\Omega^i}$ that make last contact with surface box $\mathbf{\Omega^s}$ at each month i can be calculated using Eq. 3.18 and Eq. 3.21

Moments of the surface-to-interior TTDs

Volume fraction. The fraction of the water mass at time t in each region defined by the n masks in $\mathbf{\Omega^i}$ that originated from each of the patches defined by the m masks in $\mathbf{\Omega^s}$ is given by the $m \times n$ matrix function. The water mass fractions $\langle \tau^0 | t \rangle^{\downarrow}$ can be calculate using the zeroth moment of the TTD:

$$\begin{aligned} \langle \tau^0 | t \rangle^{\downarrow} &\equiv \int_0^{\infty} \tau^0 \boldsymbol{\phi}^{\downarrow}(\tau | t)\, d\tau, \\ &= \int_0^{T} d\tau \left\{ \mathbf{B}\mathbf{\Phi}^{\dagger}(t - \tau | t) \mathbf{Q}_0^{\dagger}(t) \right\}, \end{aligned} \tag{3.23}$$

and the water mass fractions injected from the surface patch in each month i is:

$$\langle \tau^0 | t \rangle_i^{\downarrow} = \int_{(i-1)\Delta t}^{i\Delta t} d\tau \left\{ \mathbf{B}\mathbf{\Phi}^{\dagger}(t - \tau | t) \mathbf{Q}_0^{\dagger}(t) \right\}, \tag{3.24}$$

where

$$\left[\mathbf{I} - \mathbf{\Phi}^{\dagger}(t - T | t) \right] \mathbf{Q}_0^{\dagger}(t) = \mathbf{c}(t), \tag{3.25}$$

can be solved using an iterative Newton-Krylov solver (Kelley (2013), see details in Chapter 2). Multiplying from the left by $\mathbf{\Phi}^{\dagger}(t - T | t)$ corresponds to integrating the model backward in time for one period using the vector(s) on the right as the tracer initial condition. The

quantity $\mathbf{Q}^{\dagger}{}_0(t)$ is an $N \times m$ matrix where N is the number of grid boxes in the model and m is the number of interior regions.

Partitioned mean age The mean age of the water-mass fraction in each of the n interior region at time t that originated from of the m surface patch at each month i is given by the $m \times n$ matrix function whose elements are

$$a_i^{\downarrow}(t) = \frac{\langle \tau^1 | t \rangle_i^{\downarrow}}{\langle \tau^0 | t \rangle_i^{\downarrow}} \tag{3.26}$$

where $\langle \tau^1 | t \rangle_i$ is:

$$\begin{aligned} \langle \tau^1 | t \rangle_i^{\downarrow} &\equiv \int_0^{\infty} \tau^1 \boldsymbol{\phi}^{\downarrow}(\tau | t)\, d\tau \\ &= \int_{(i-1)\Delta t}^{i\Delta t} d\tau \mathbf{B} \boldsymbol{\Phi}^{\dagger}(t - \tau | t) \left\{ \tau \mathbf{Q}_0^{\dagger}(t) + T \boldsymbol{\Phi}^{\dagger}(t - T | t) \mathbf{Q}_1^{\dagger}(t) \right\} \end{aligned} \tag{3.27}$$

where

$$\left[\mathbf{I} - \boldsymbol{\Phi}^{\dagger}(t - T | t) \right] \mathbf{Q}_1^{\dagger}(t) = \mathbf{Q}_0^{\dagger}(t), \tag{3.28}$$

can also be solved using the newton Krylov solver.

In summary, the main procedure to compute the water mass fraction that originated from surface patch and its age using adjoint model is:

1. Define the set of interior region ($\boldsymbol{\Omega}^{\mathsf{i}}$) and surface patch masks ($\boldsymbol{\Omega}^{\mathsf{s}}$)

2. define initial condition $\mathbf{c}(t)$ at time t. If the regions of interest are in the upper ocean the above equation should be solved for several values of $t \in [0, T]$ to resolve the seasonal cycle. Otherwise, the result TTD in deep ocean box will be similar by starting with any time.

3. Using an iterative Newton Krylov solver solve for $\mathbf{Q}_0^{\dagger}(t)$ from the Eq. 3.25 and solve for $\mathbf{Q}_1^{\dagger}(t)$ from the the Eq. 3.28.

4. Perform a sequence of backward model runs starting at t and run back to different times $t - \tau_k$ for $k = 0, \cdots 11$ with $\tau_k = k\Delta\tau$. Therefore, the fraction of water mass and its age in interior box $\mathbf{\Omega}^{\mathsf{i}}$ that make last contact with surface box $\mathbf{\Omega}^{\mathsf{s}}$ at each month i can be calculated using Eq. 3.25 and Eq. 3.27.

3.3 Results

To quantify the "Stommel's demon " in terms of subduction and obduction, I calculate the water fraction and the ventilation time scales of the water mass that was subducted from or will be obducted to the surface at each month. The water fraction of subduction represents how much new water is pumped from the surface patches to the thermocline, while the water fraction of obduction represents how much water into the thermocline is returned to the mixed layer. The age of subduction represents how long the new water is pumped from the surface patches to the permanent thermocline while the age of obduction is the life expectancy of water parcel which represents how long water in the permanent thermocline is transported back to the mixed layer. Since the theory of "Stommel's demon" focuses on the main thermocline, I focus on the upper ocean (200 - 1000m) at global scales and then I discuss the subduction and obduction of the main thermocline in the North Atlantic and the North Pacific in comparison with previous studies (Williams et al., 1995; Qiu and Huang, 1995; Marshall et al., 1993).

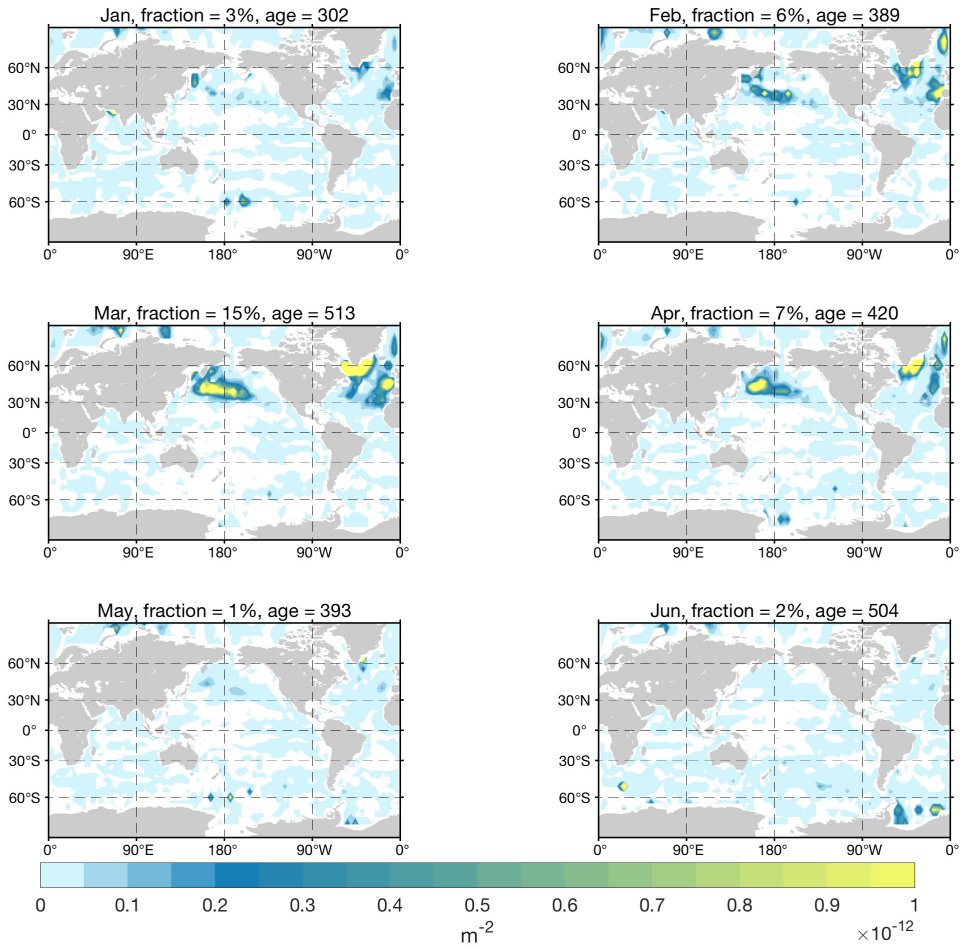

Figure 3.7: The volume fraction of the water in the upper ocean (200-1000m) that was subducted from the surface ocean from January to June. The total fraction and mean age of water that was subducted at each month are listed in the titles. The sum of the total fraction for each month is equal to one.

3.3.1 Global ocean

In the first calculation, I injected one unit of tracer uniformally in the upper ocean (200 - 1000m) and run the adjoint model and forward model to study the subduction and obduction contribution in each month. The results indicate where, which month and how much the water are exchanged between the surface ocean and the ocean between 200 and 1000 m.

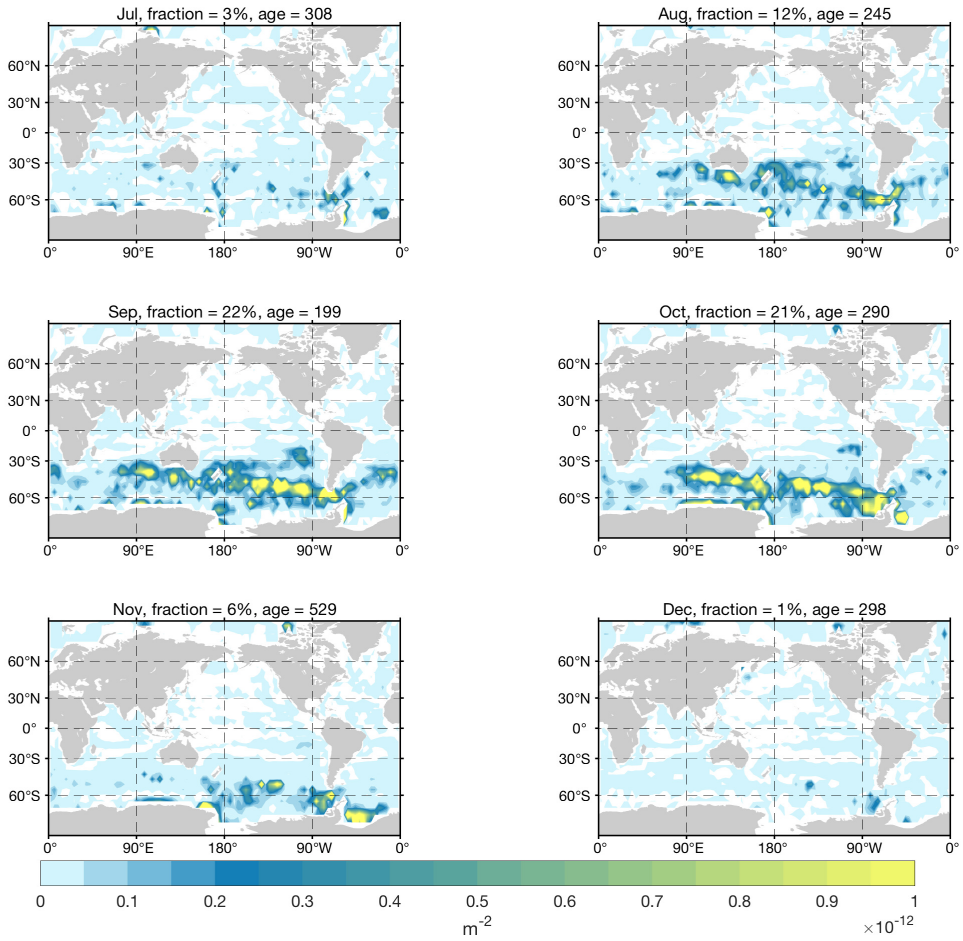

Figure 3.8: The volume fraction of the water in the upper ocean (200-1000m) that was subducted from the surface ocean from July to December. The total fraction and mean age of water that was subducted at each month are listed in the titles. The sum of the total fraction for each month is equal to one.

Subduction

Figure 3.7 and figure 3.8 show how much of the water that subducted from the surface to the upper ocean during each month. Figure 3.9 demonstrates the monthly contribution of the surface water from different ocean basins to the upper ocean. The total fraction of subduction in the Northerm hemisphere (excluding the tropical region 10°S - 10°N) is 33%, and the subducted water fraction in March is up to 15%. Subduction in the northern hemisphere mainly takes place in the North Atlantic ocean (16%), and the North Pacific ocean (12%).

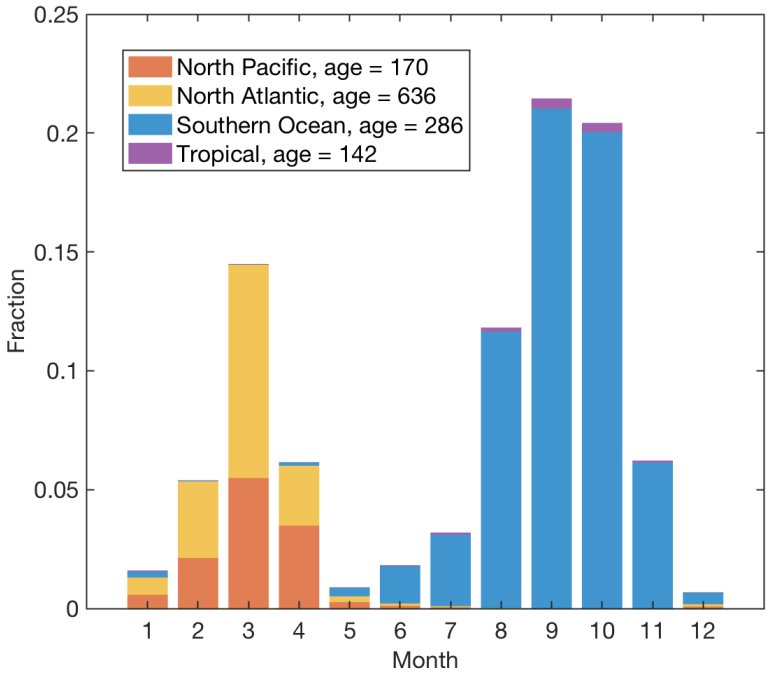

Figure 3.9: Monthly distribution of the volume fraction of water in the upper ocean (200-1000m) that was subducted from the surface in each ocean basin: the North Pacific (10 - 60°N), the North Atlantic (10 - 60°N), the Southern Ocean(30 - 60°S), the Tropical ocean (10°S - 10°N). The fractions from all the ocean basins sum to one.

The effective subduction in the northern hemisphere lasts from February to April and peaks in March (15%). Moreover, subduction in the southern hemisphere mainly occurs in the Southern Ocean, starting from August to November and peaking in September(21%) and October (20%). For the upper ocean, water that subducted from the North Atlantic is older than that from other ocean basins, which is 600 years old (see Figure 3.9). Therefore, the water parcel that subducted in March, which partly comes from North Atlantic, is older than the water parcel that subducted in September and October, which mainly comes from the Southern Ocean. The pattern of major subduction region in Figure 3.7 and Figure 3.8 is similar to the map of the annual subduction rates calculated using kinematic method (Liu and Huang, 2011) where the main subduction region is subtropical gyre in Pacific, subtropical gyre and subpolar region in the Atlantic and Antarctic Circumpolar Current (ACC) region. Those locations are associated with the formation of mode water (Liu and

Huang, 2011; Talley, 1999).

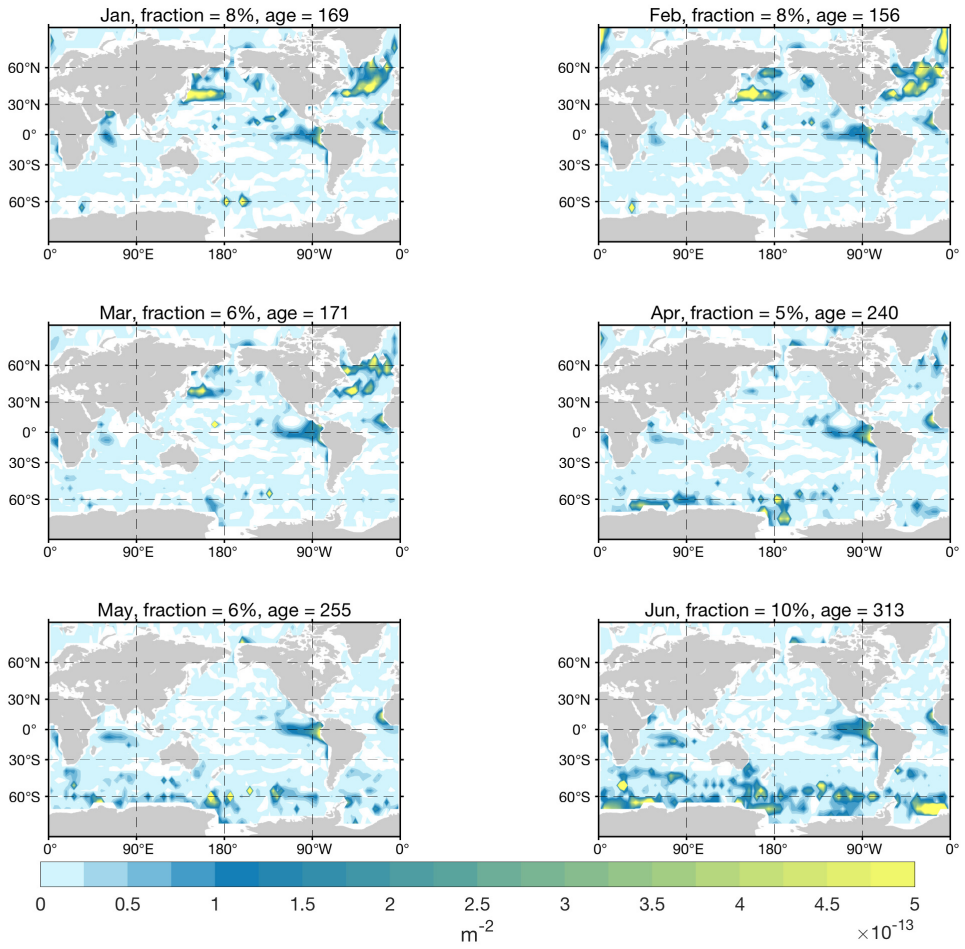

Figure 3.10: The volume fraction of the water in the upper ocean (200-1000m) that will be transported back to the surface ocean from January to June. The total fraction and mean age of water that returned to the surface at each month are listed in the titles. Note the age of obduction is the mean life expectancy of water mass which represents how long it takes for the water in the permanent thermocline to be transported back to the surface ocean. The sum of the total fraction for each month is equal to one.

Obduction

Figure 3.10 and figure 3.11 show how much water in the upper ocean (200-1000m) that will return to the mixed layer during each month, and the figure 3.12 demonstrates the monthly volume fraction that will return to different ocean basins. Obduction primarily

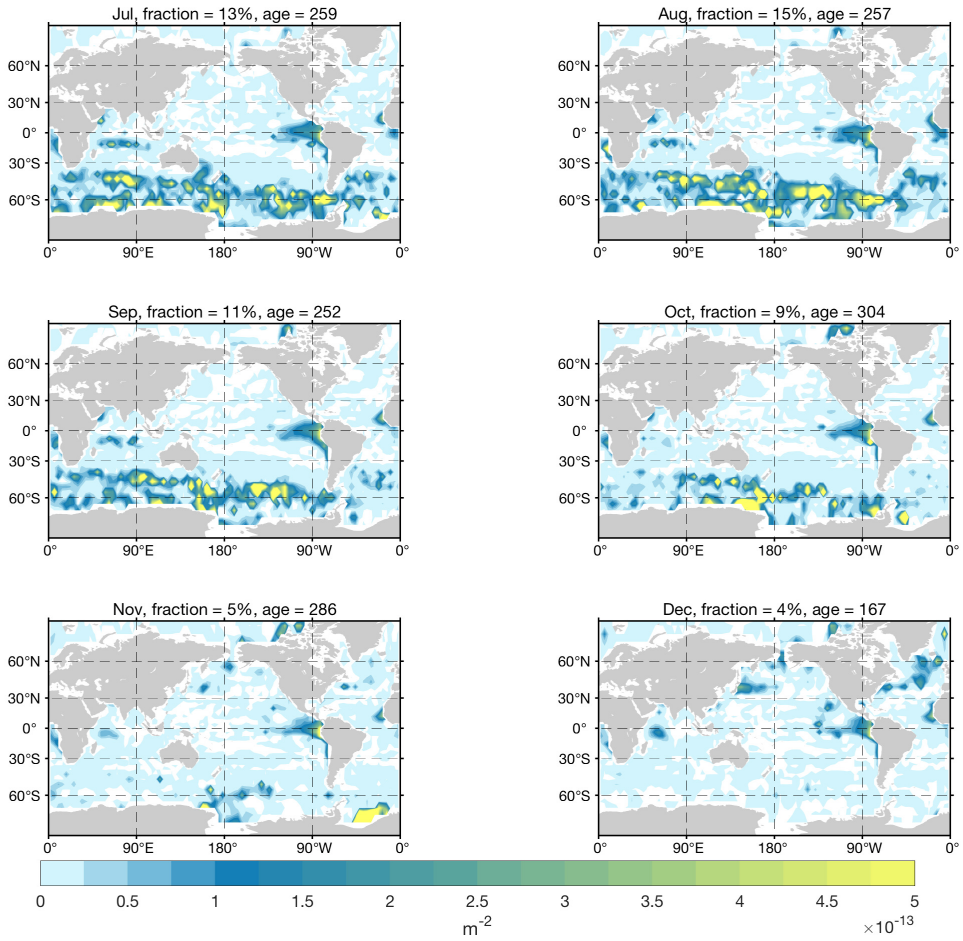

Figure 3.11: The volume fraction of the water in the upper ocean (200-1000m) that will be transported back to the surface ocean for each month during the July to December. The total fraction and mean age of water that returned to the surface at each month are listed in the titles. Note the age of obduction is the mean life expectancy of water mass which represents how long it takes for the water in the permanent thermocline to be transported back to the surface ocean. The sum of the total fraction for each month is equal to one.

occurs in ACC regions (48%) where strong westerlies drive Ekman upwelling of the water. The dominant obduction perid starts from April to November and peaks in August. The second primary region is the upwelling region in the eastern equatorial band and in the coastal upwelling region along the edges of the basin, which transports 35% of the water in the upper ocean back to the surface. Obduction in tropical region occurs throughout the whole year. The rest of the obduction takes place at the North Atlantic (10%) and the North Pacific (8%), and the effective period is from December to March. Note that there are

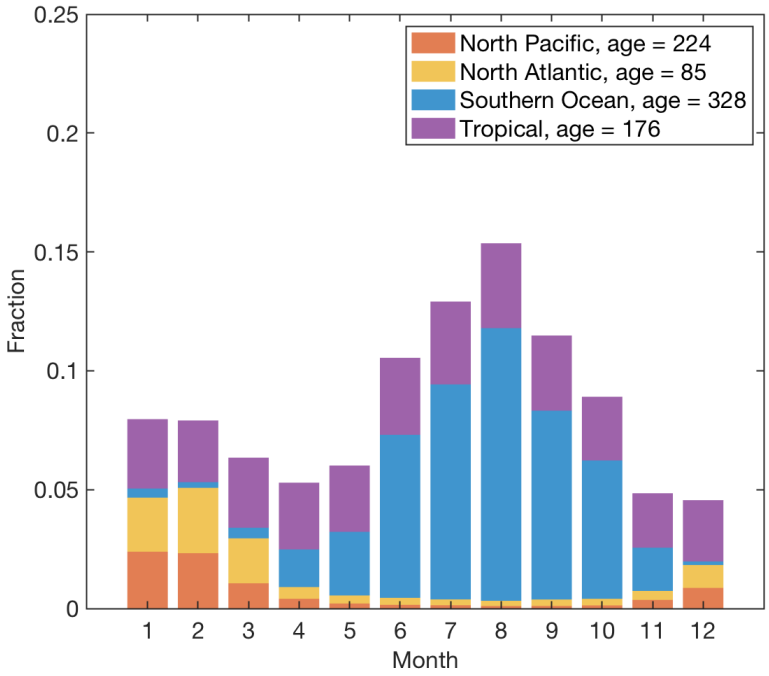

Figure 3.12: Monthly distribution of volume fraction of water in upper ocean (200-1000m) that will be transported back to the surface in each ocean basin: the North Pacific (10 - 60°N), the North Atlantic (10 - 60°N), the Southern Ocean(30 - 60°S), the Tropical ocean (10°S - 10°N). The fractions from all the ocean basins sum to one. Note that the "age" of obduction is the mean transit time from the permanent thermocline to the mixed layer.

a few locations where both subduction and obduction take place, such as, the ACC region and the recirculation region of the Gulf Stream and Kuroshio. The regions are called the "ambiduction" regions (Qiu and Huang, 1995; Liu and Huang, 2011). However, obduction and subduction in the "ambiduction" region occurs during different times of the year. The subduction in the recirculation region of the Gulf Stream and Kuroshio is mainly in March and April, while obduction takes place mainly in January and February. Moreover, in the ACC region, the largest subduction period and obduction period overlap, but peak during different months.

3.3.2 North Atlantic

To study the subduction and the obduction of the permanent thermocline in the North Atlantic, I take the upper layers (200 - 1000m) of the North Atlantic ($10° - 60°$N) as a whole and inject one unit of tracer in the box. I calculate the fraction and the ventilation time scales of water that subducted from or obducted to surface at each month. The results indicate where, which month and how much the water are exchanged between the surface ocean and permanent thermocline in the North Atlantic.

Subduction

Figure 3.13 and figure 3.14 show the geographic location of subduction take places during each month, and figure 3.15 shows the monthly distribution of water fraction that originated at different ocean basins. It shows that 74% of the permanent thermocline in North Atlantic is subducted from the local ocean basin. Moreover, the effective subduction in the North Atlantic starts from January, ends in May and peaks in March, which disagrees with previous studies that claimed that the effective obduction period starts in March (Williams et al., 1995; Qiu and Huang, 1995). There are three locations in the North Atlantic that are associated with mode water formation: the northwestern part of the subtropical gyre which are associated with the formation of Subtropical Mode Water, the eastern sides of the subtropical gyres which is associated with the formation of Eastern Subtropical Mode water, and the north poleward eastern boundary which is associated with the formation of Subpolar Mode Water (Talley, 1999; Hanawa and Talley, 2001; Liu and Huang, 2011). Figure 3.13 shows that the formation of those mode waters during a different months. On the other hand, 23% of water is subducted from the Southern Ocean. Subduction from the Southern Ocean takes place from August to November.

In summary, the main thermocline in the North Atlantic not only selects late winter and early

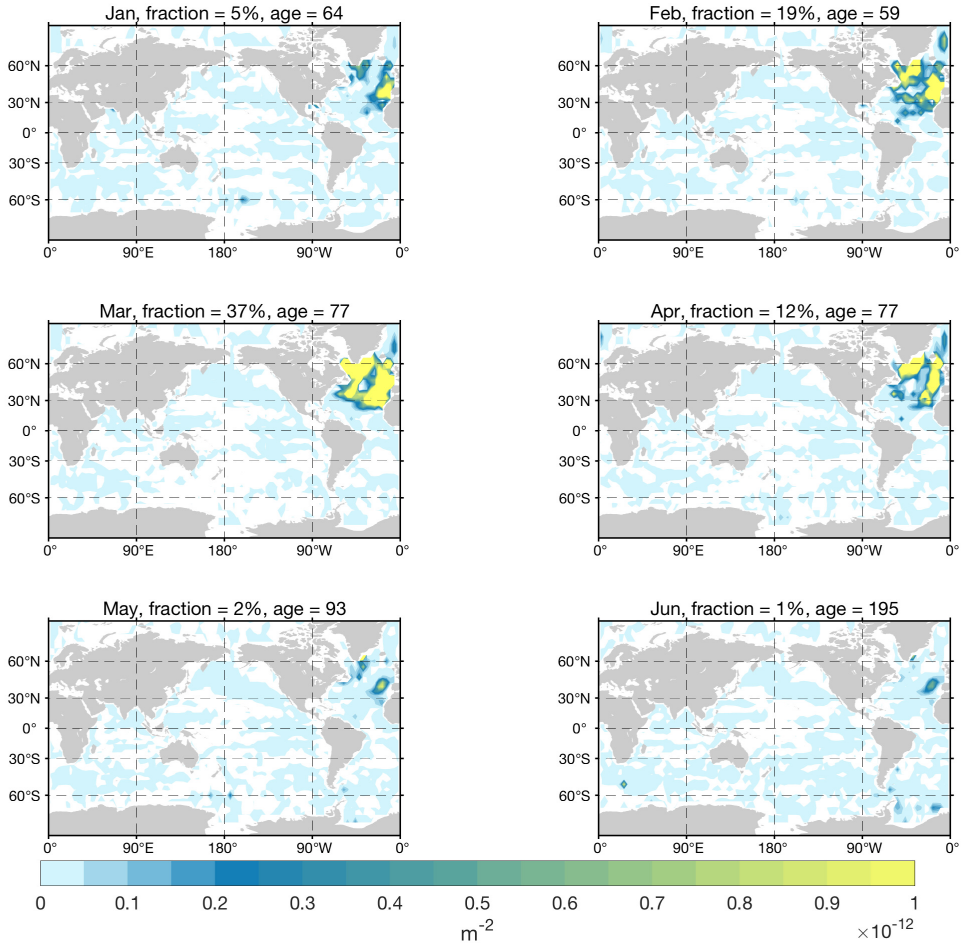

Figure 3.13: The volume fraction of the water in the upper North Atlantic ocean (200-1000m, 10-60°N) that was subducted from the surface ocean from January to June. The total fraction and mean age of water that was subducted at each month are listed in the titles. The sum of the total fraction for each month is equal to one.

spring water from the North Atlantic but also selects the Southern Hemisphere late winter and early spring water from the Southern Ocean. The kinematic method that calculates the suduction rate at the base of the mixed layer can only explain the subduction occurs locally (Williams et al., 1995; Qiu and Huang, 1995). Moreover, the water subducted locally is younger than the water coming from other ocean basins, therefore, water subducted during winter and spring is younger than water that appears to have been subducted during the summer and fall, but which was in fact subducted from the Southern Hemisphere winter and spring.

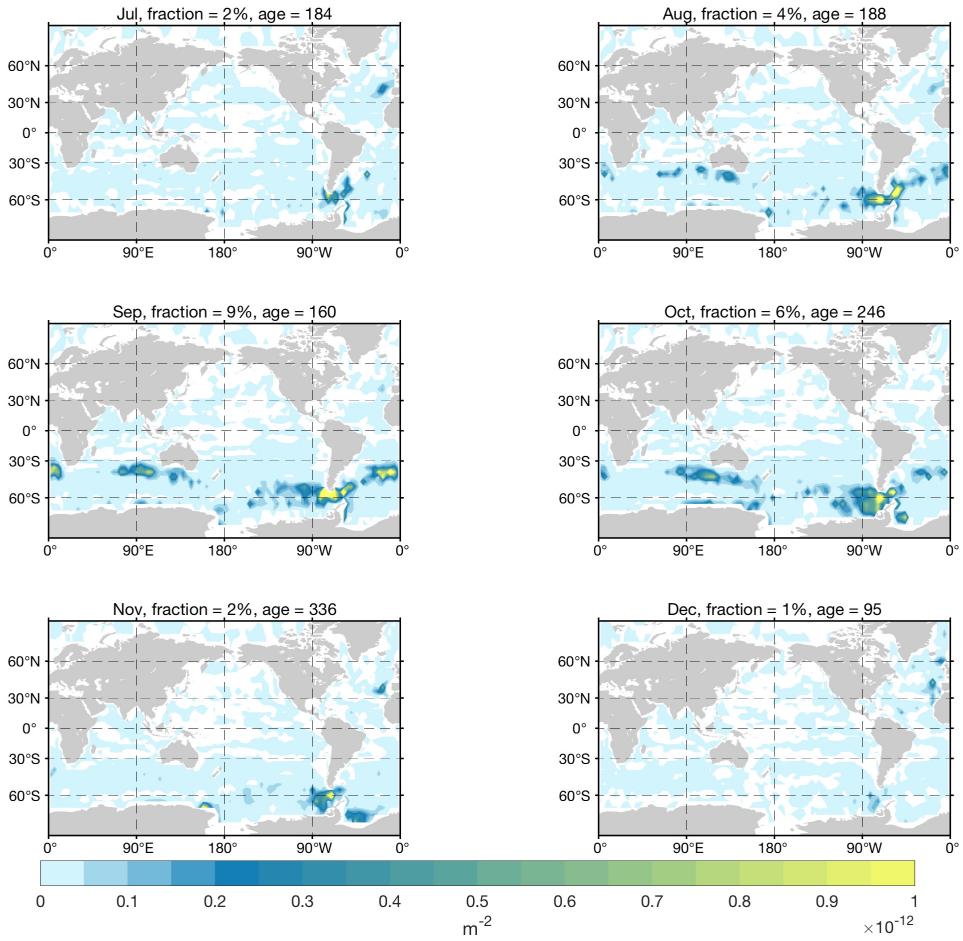

Figure 3.14: The volume fraction of the water in the upper North Atlantic ocean (200-1000m, 10-60°N) that was subducted from the surface ocean from July to December. The total fraction and mean age of water that was subducted at each month are listed in the titles. The sum of the total fraction for each month is equal to one.

Obduction

Figure 3.16 and figure 3.17 show how much of volume fraction in the upper North Atlantic ocean (200-1000m) that will return to the mixed layer during each month. Figure 3.18 demonstrates the monthly volume fraction that will return to different ocean basins. 64% of the water in the main thermocline upwells to the surface of the north subtropical gyre and the subpolar gyre region from December to March, which agrees with the two to four months of effective entrainment periods identified by (Williams et al., 1995). The spatial

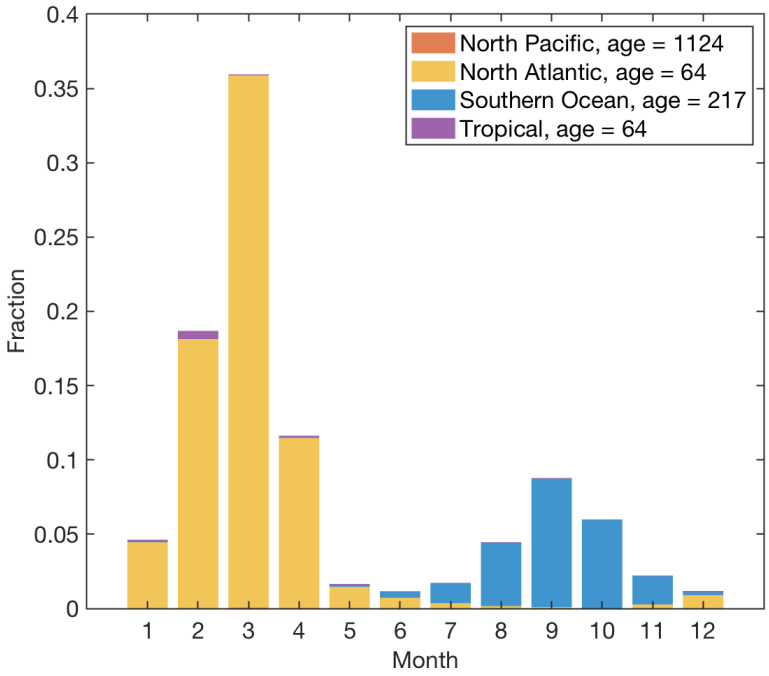

Figure 3.15: Monthly distribution of the volume fraction of water in the upper North Atlantic ocean (200-1000m, 10-60°N)that was subducted from the surface in each ocean basin: the North Pacific (10 - 60°N), the North Atlantic (10 - 60°N), the Southern Ocean(30 - 60°S), the Tropical ocean (10°S - 10°N). The fractions from all ocean basins sum to one.

pattern of obduction in North Atlantic is also similar to the map of the obduction rate in previous studies (Williams et al., 1995; Qiu and Huang, 1995). However, previous studies ignore the other two major pathways of obduction: 20% of the water returns to the surface from the strong equatorial and coastal upwelling region which lasts throughout the year, while 22% water is returned back to the ACC region and upwells to the surface from April to November. The long trip to the Southern Ocean takes 700 years while the mean transit time to the surface locally is only 37 years.

3.3.3 North Pacific

In addition to North Atlantic, the "Stommel's demon" in the North Pacific have been studied by Qiu and Huang (1995). To make contact with this previous study, I inject one unit of

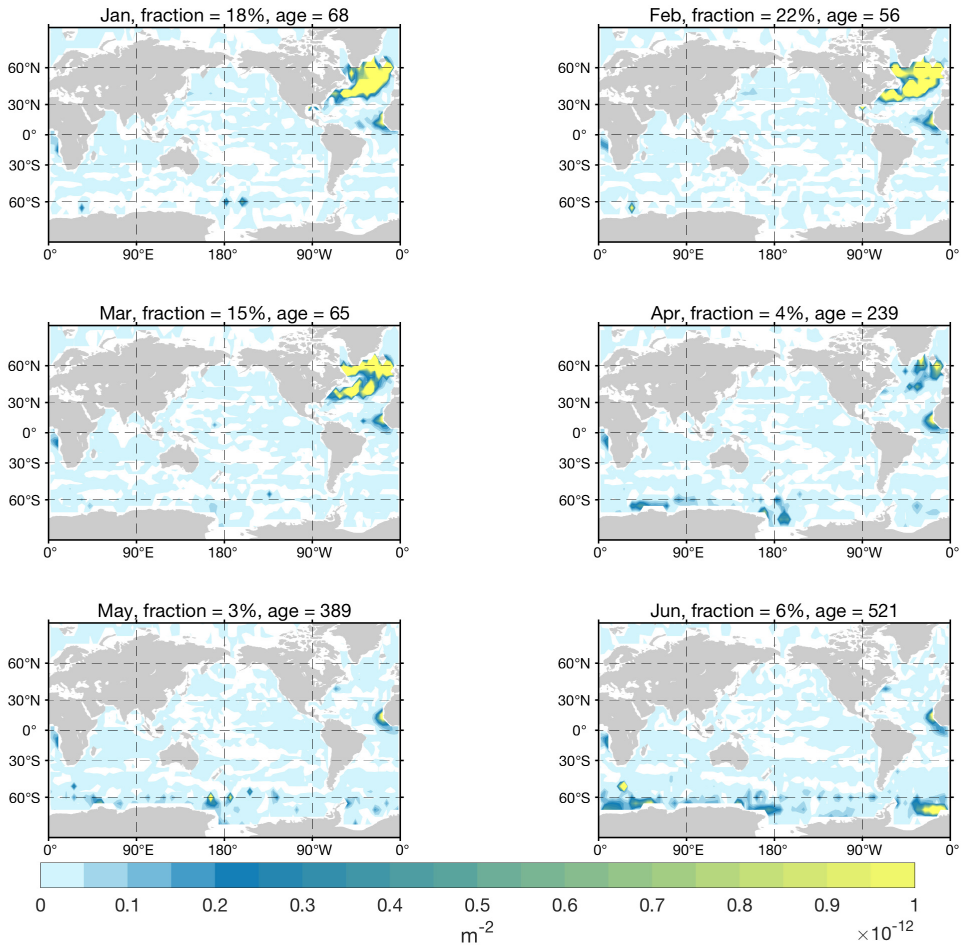

Figure 3.16: The volume fraction of the water in the upper North Atlantic ocean (200-1000m, 10-60°N) that will be transported back to the surface ocean from January to June. The total fraction and mean age of water that returned to the surface at each month are listed in the titles. Note the age of obduction is the mean life expectancy of water mass which represents how long it takes for the water in the permanent thermocline to be transported back to the surface ocean. The sum of the total fraction for each month is equal to one.

tracer in the upper North Pacific (200 - 1000m, 10-60°N) and calculate the fraction and the mean ventilation time of water that subducted from or obducted to the surface during each month.

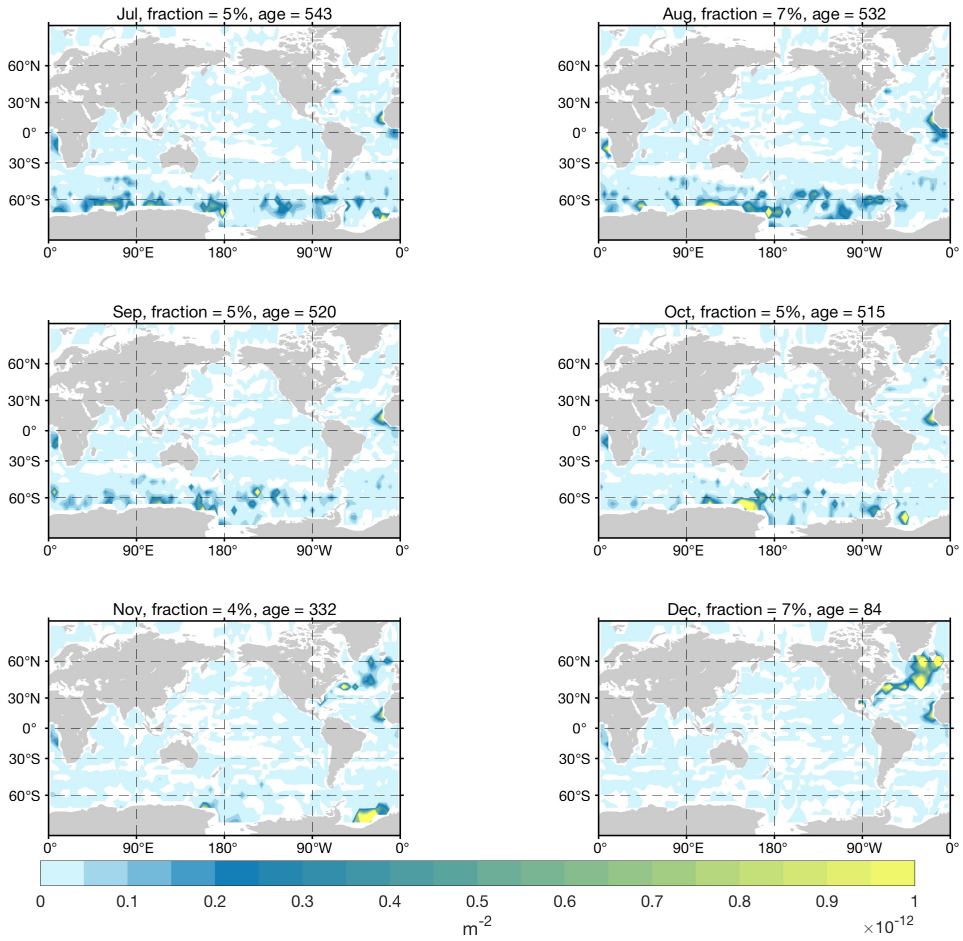

Figure 3.17: The volume fraction of the water in the upper North Atlantic ocean (200-1000m, 10-60°N) that will be transported back to the surface ocean from July to December. The total fraction and mean age of water that returned to the surface at each month are listed in the titles. Note the age of obduction is the mean life expectancy of water mass which represents how long it takes for the water in the permanent thermocline to be transported back to the surface ocean. The sum of the total fraction for each month is equal to one.

Subduction

Figure 3.19 and figure 3.20 show volume fraction of water in the upper North Pacific ocean (200-1000m) that was subducted from the mixed layer during each month. Figure 3.21 shows the monthly volume fraction that will return to different ocean basins. 52% of water in the main thermocline of the North Pacific is subducted locally, mainly in the subtropical gyre while 34% of water comes from the Southern Ocean. The spatial pattern of subduction in the

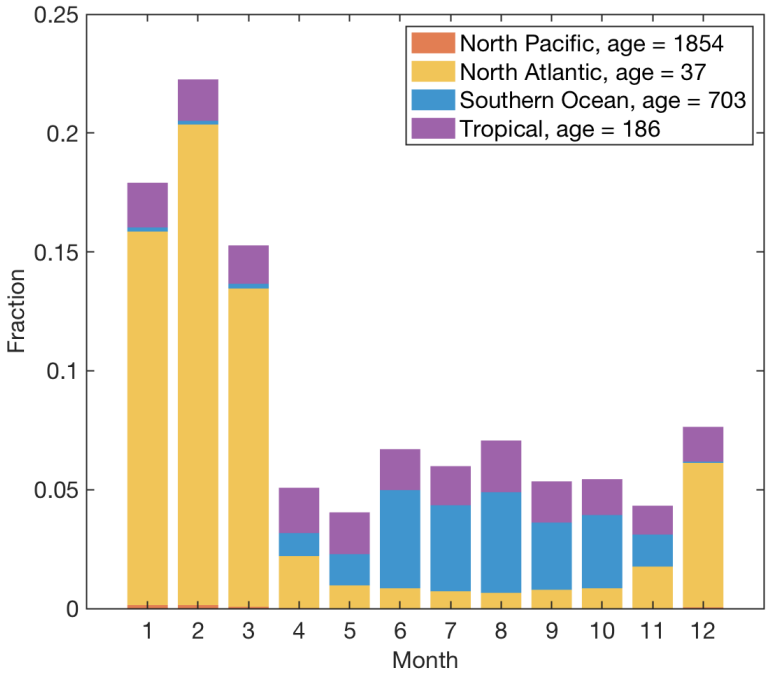

Figure 3.18: Monthly distribution of the volume fraction of water in the upper North Atlantic ocean (200-1000m, 10-60°N) that will be transported back to the surface of different ocean basins: the North Pacific (10 - 60°N), the North Atlantic (10 - 60°N), the Southern Ocean(30 - 60°S), the Tropical ocean (10°S - 10°N). The fractions from all ocean basins sum to one. Note the "age" of obduction is the mean transit time of water parcel to be transported from the permanent thermocline to the mixed layer.

North Pacific agrees with the map of the high subduction rate calculated in Qiu and Huang (1995). The effective subduction periods in the North Pacific starts in January, peaks in March and ends in May, and the effective subduction period in the Southern Ocean is from July to November. As I found for the North Atlantic, the subduction location in the North Pacific is also related to three mode water formation regions: the Kuroshio extensions in the subtropical gyres, the eastern part of the subtropical gyres and the subpolar fronts on the poleward boundaries of the subtropical gyres (Talley, 1999; Hanawa and Talley, 2001; Liu and Huang, 2011). It is interesting to note that 9% of water originates from the surface of North Atlantic which mainly takes place in March. The water in the North Pacific thermocline that was last subducted from the North Atlantic has a mean of nearly 2000 years.

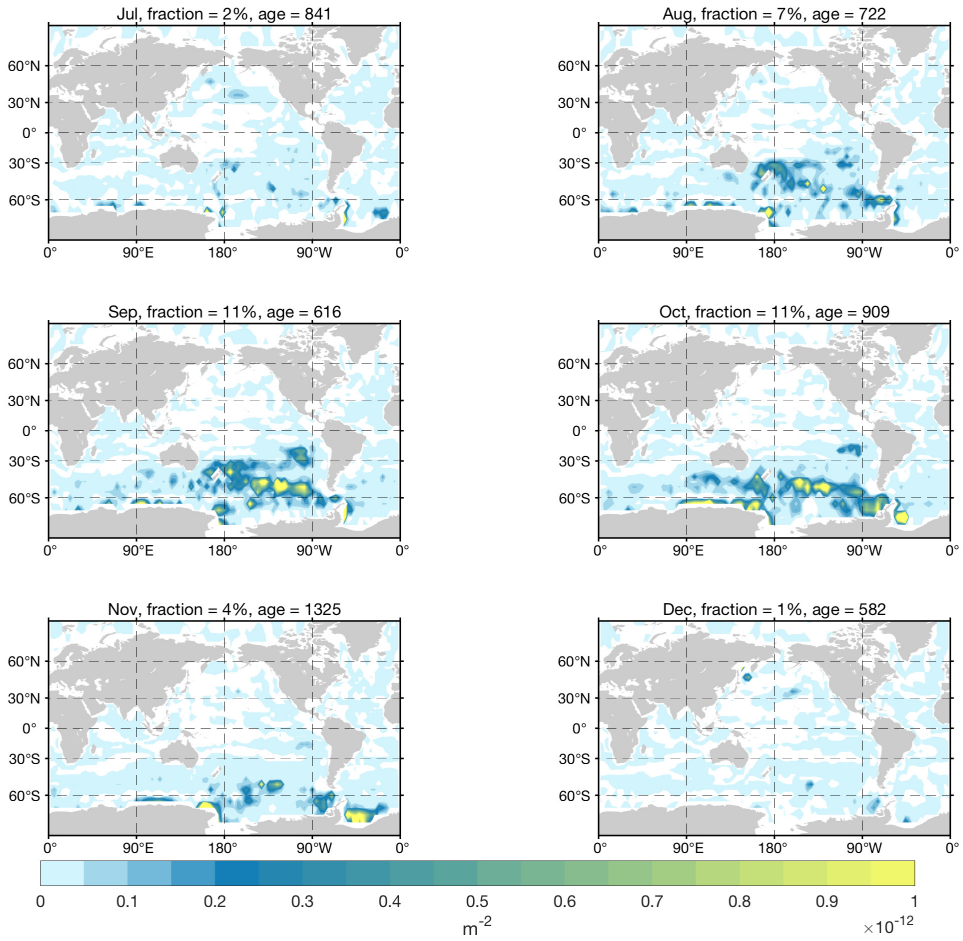

Figure 3.19: The volume fraction of the water in the upper North Pacific ocean (200-1000m, 10-60°N) that was subducted from the surface ocean from January to June. The total fraction and mean age of water that was subducted at each month are listed in the titles. The sum of the total fraction for each month is equal to one.

Obduction

Figure 3.22 and figure 3.23 show the spatial distribution of the volume fraction that returns to the mixed layer during each month. Figure 3.24 demonstrates the monthly distribution of water fraction that ventilated back to the surface layer of different ocean basins. 53% of the erosion of water mass in the upper North Pacific takes place mainly in eastern tropical Atlantic where there is strong equatorial and coastal upwelling. Only 32% of water is transported back to the surface locally. The effective obduction period is from November to

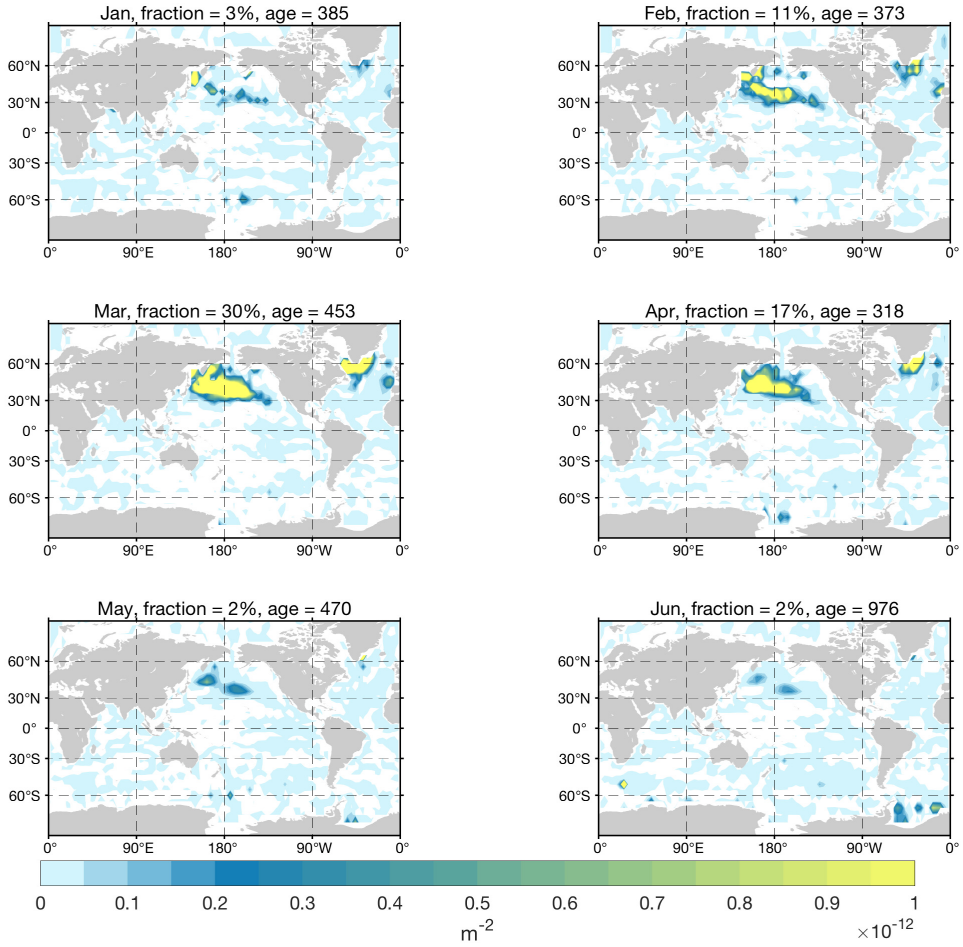

Figure 3.20: The volume fraction of the water in the upper North Pacific ocean (200-1000m, 10-60°N) that was subducted from the surface ocean from July to December. The total fraction and mean age of water that was subducted at each month are listed in the titles. The sum of the total fraction for each month is equal to one.

April. Moreover, 18% of the water is transported to the Southern Ocean and re-enters the surface from April to November.

3.4 Discussion

The present study has provided an accurate estimate of the effective subduction and obduction period along with an estimate of the volume fraction from contributes of each month. I

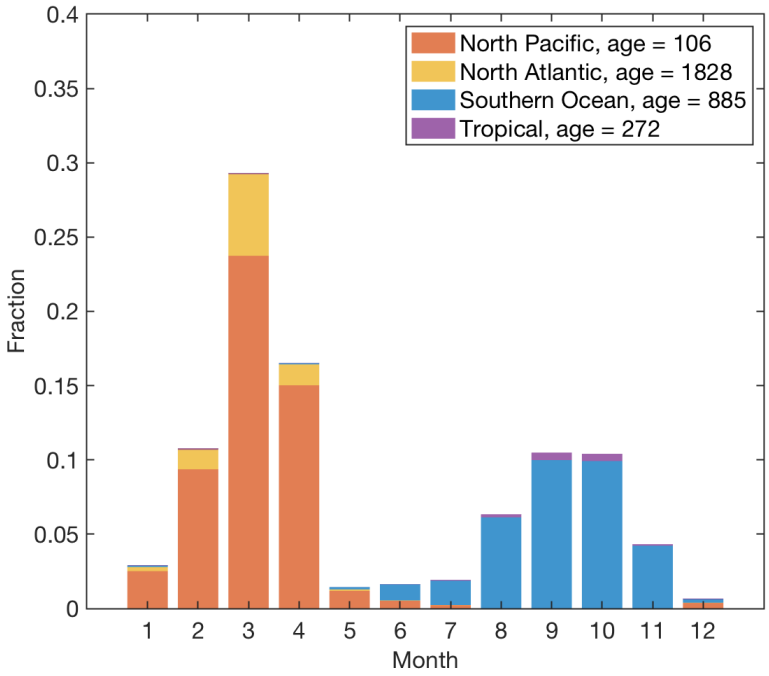

Figure 3.21: Monthly distribution of the volume fraction of water in the upper North Pacific ocean (200-1000m, 10-60°N) that was subducted from the surface of different ocean basins: the North Pacific (10 - 60°N), the North Atlantic (10 - 60°N), the Southern Ocean(30 - 60°S), the Tropical ocean (10°S - 10°N). The Fractions from all ocean basins sum to one

showed that the Southern Ocean is the dominant subduction region(64%), which lasts from June to November and peaks at September(21%) and October (20%). Suduction from the surface North Pacific (12%) and the surface North Atlantic (16%) lasts from January to April and peaks at March (15%). The obduction occurs mainly in ACC regions (48%), lasting from April to November and peaking in August. The second primary obduction region is the upwelling region in the eastern equatorial band and coastal upwelling along the edges of the basin, which upwell 35% of the water back to surface and lasts the whole year. The rest of the obduction takes place at the North Atlantic (10%) and the North Pacific (8%) and the effective period is from December to March.

Unlike the previous studies (Williams et al., 1995; Qiu and Huang, 1995; Marshall et al., 1993; Liu and Huang, 2011) which only explain the local selection of water property in the mixed layer, the TTD method provides a novel way to quantify Stommel's demon by

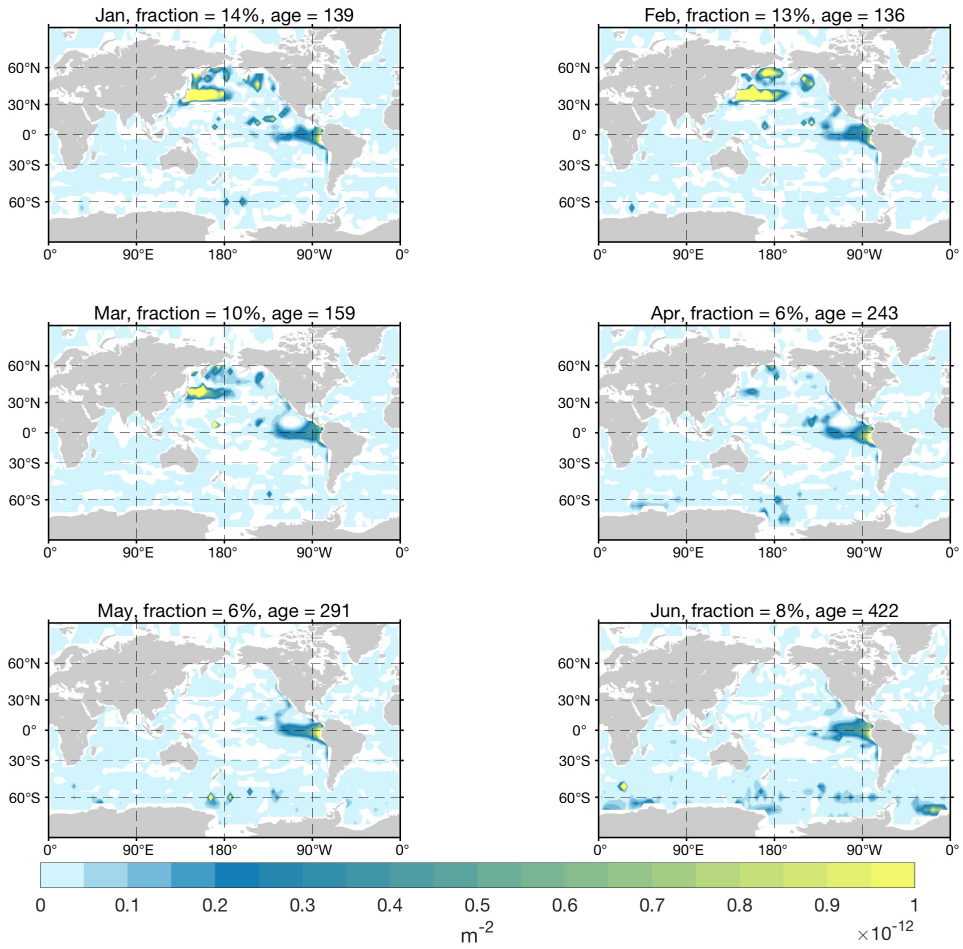

Figure 3.22: The volume fraction of the water in the upper North Pacific ocean (200-1000m, 10-60°N) that will be transported back to the surface ocean from January to June. The total fraction and mean age of water that returned to the surface at each month are listed in the titles. Note the age of obduction is the mean life expectancy of water mass which represents how long it takes for the water in the permanent thermocline to be transported back to the surface ocean. The sum of the total fraction for each month is equal to one

identifying the fraction contribution of water from the different ocean basins. For example, the main thermocline in the North Pacific not only selects late winter and early spring water properties of the mixed layer in the North Pacific but also selects early spring properties of the mixed layer in the North Atlantic and the late summer and early fall water properties of the mixed layer in the Southern Ocean. The kinematic method, however, can only detect one "Stommel's demon" in the North Pacific who control the supply of water from the surface North Pacific ocean into the interior ocean. Here I suggest there is a whole team of demon

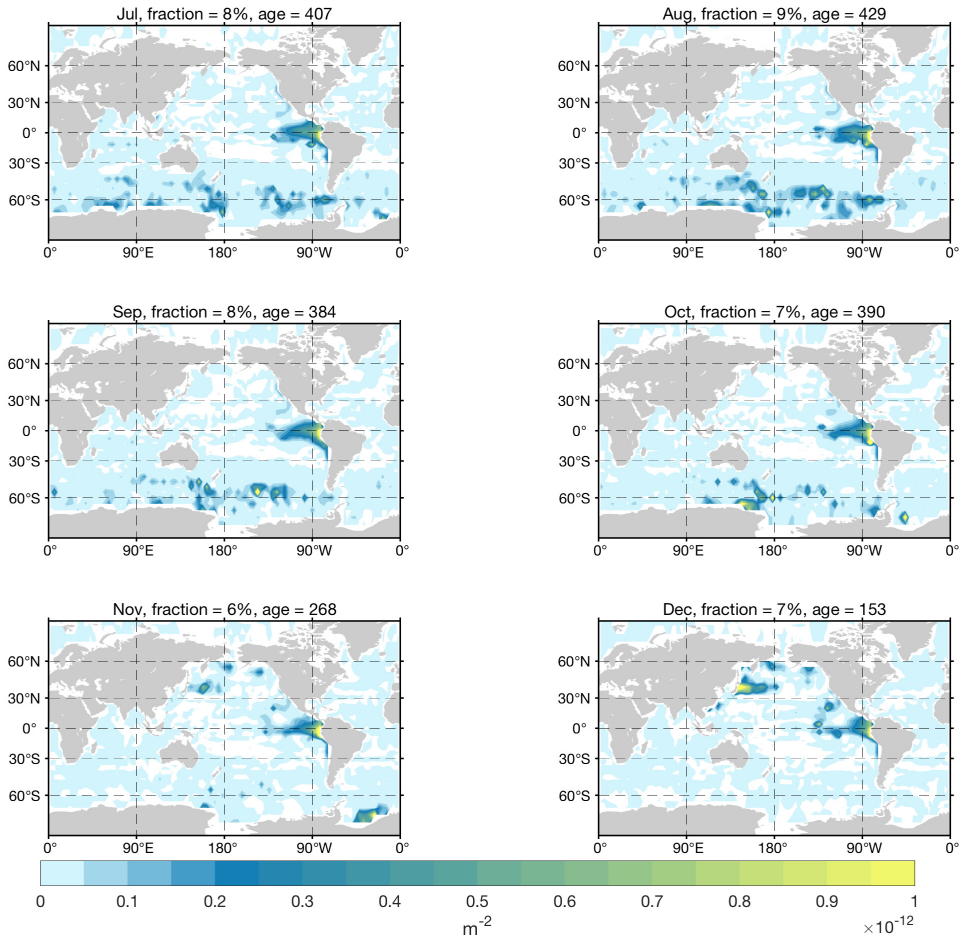

Figure 3.23: The volume fraction of the water in the upper North Pacific ocean (200-1000m, 10-60°N) that will be transported back to the surface ocean from July to December. The total fraction and mean age of water that returned to the surface at each month are listed in the titles. Note the age of obduction is the mean life expectancy of water mass which represents how long it takes for the water in the permanent thermocline to be transported back to the surface ocean. The sum of the total fraction for each month is equal to one

operating in different regions.

Moreover, the TTDs method can be used to explain the formation and erosion of mode water(Hanawa and Talley, 2001; Talley, 1999). Liu and Huang (2011) used the map of the annual net subduction/obduction rate below the mixed layer to explain the location of the formation and erosion of mode water. However, it ignores the role of mixing and diffusion in the thermocline. The TTDs method developed in the present study can precisely describe

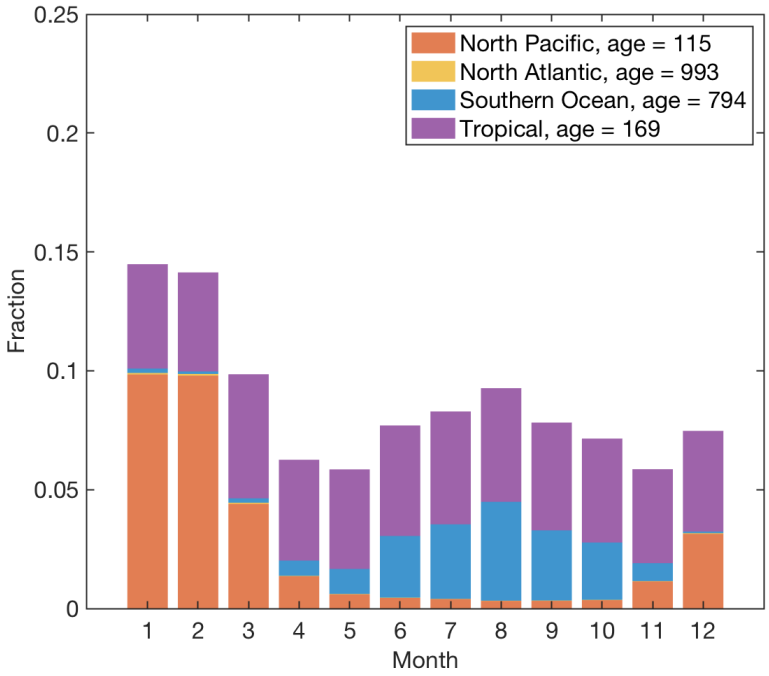

Figure 3.24: Monthly distribution of volume fraction of water in the upper North Pacific ocean (200-1000m, 10-60°N) will be transported back to the surface of different ocean basins: the North Pacific (10 - 60°N), the North Atlantic (10 - 60°N), the Southern Ocean(30 - 60°S), the Tropical ocean (10°S - 10°N). The fractions from all ocean basins sum to one. Note the "age" of obduction is the mean transit time of water parcel to be transported from the permanent thermocline to the mixed layer.

where, when and how many the water from specific mode water is coming from or is going to.

The other important application of the new method is to provide a quick estimation concentration of tracers in a given interior ocean box by integrating the monthly and spatially distributed water fraction combined with the monthly surface concentration. For example, Dall'Olmo et al. (2016) shows that the suspended particulate organic carbon (POC), as well as dissolved organic carbon DOC, can be exported when the mixed layer reaches its maximum depth (usually in late winter) in a process called "seasonal mixed layer pumping". This is a biogeochemical version of "Stommel's demon". The study estimated that the mixed-layer pump of suspended POC supplies between 0.1 and 0.5 PgC yr^{-1}, which on average is

equal to 23 % of the carbon supplied by fast-sinking particles and even amounts to 100% at the region where deep winter mixing happened. However, the calculation in the study only considered the vertical transfer due to the local change of the mixed layer depth and ignored the effect of the lateral induction and diffusion along the isopycnal. The subduction rate due to lateral induction has been proven to be about two to four times greater than that resulting from Ekman pumping alone in North Atlantic subtropical gyre (Marshall et al., 1993). Therefore, the calculated monthly subduction fraction of the upper ocean can be applied to re-evaluate the "seasonal mixed layer pumping" (Dall'Olmo et al., 2016).

Chapter 4

Quantifying ventillation of the deep water masses

4.1 Introduction

The formation of deep waters and its interior transport along multiple pathways, that is, the global overturning circulation (GOC), is essential for understanding the ocean's role in climate. The GOC adjusts the climates by transporting the warm water from the tropical region to the mid-latitude and transporting the cold water in the opposite direction at the deep ocean. Moreover, the GOC affects the climate not only by altering the air-sea exchange of carbon but also by redistributing the transport of carbon and nutrients in the interior ocean.

Efforts have been made to quantify the ocean overturning and its relation to the formation of different water mass (Broecker, 1987, 1991). The history of meridional overturning can be found in Richardson (2008). The most updated quantitative picture of the large-scale circulation contains four components: one starts with the formation of North Atlantic deep

water (NADW) in the Labrador Sea and the Nordic Sea. The cold and salty NADW flows northward to the Southern Ocean and then returns to the surface or forms the AABW; The second component is associated with the formation of the Antarctic bottom water (AABW) in the Southern Ocean. The dense deep water moves northward at the bottom of the Atlantic, the Pacific and the Indian ocean and hence upwells diapycnally into the local deep water mass, that is, the NADW, the Pacific Deep Water (PDW) and the Indian Deep Water (IDW); The third and fourth components are associated with diffusively formed PDW and IDW which moves southward and upwell to the surface in the Southern Ocean (Lumpkin and Speer, 2007; Talley, 2013; Cessi, 2019). The main return pathway for the deep water is through the wind-driven upwelling branch in the Southern Ocean. The other return pathway is diapycnal upwelling in the Pacific and the Indian ocean. The schematic diagram of GOC in those studies provides a useful overview of how the large-scale circulation maintains the climatological density structure of the ocean, However, the geostrophic flow transport estimation based on the water mass transformation and heat conservation ignores the important along-isopycnal eddy-diffusive transport which leads to various transport pathways of deep water. For example, Ali Muttaqi Shah et al. (2017) argued that the effect of diffusion is critical for tracing the pathways of the GOC in addition to the advection.

Another method to study the transport of water masses along advective–diffusive pathways is to trace the movement of water directly using floats. For example, floats that released in the Labrador Sea show the complex transport pathways with trajectories spreading throughout the western basin or recirculating within the subpolar gyre rather than following the narrow deep western boundary currents (Bower et al., 2009). Eddy stirring is thought to be the main driver of the intertwined spreading pathway of the Labrador Deep Water. (Bower et al., 2009) provides a realistic picture of the ocean circulation in the short term, however, it's impossible to represent the long term ventilation process that takes hundreds to thousands of years. Therefore, studies have used the modeled circulation to simulate the Lagrangian pathways of the tracers in the interior ocean (Bower et al., 2011; Lozier et al., 2013; Ali Muttaqi Shah

et al., 2017). Although the Lagrangian calculations provide the typical sample ventilation pathways, it is difficult to compute enough trajectories of long enough duration to provide a summary diagnostics.

The Green function and the transit time distribution (TTD) method are the Eulerian approaches that summary the complex and intertwined pathways of the advective and diffusive transports. The zeroth moment of TTD provides the volume fraction of the water in a specific location that was last in contact with or will make first contact with the surface ocean. The first moment of TTD divided by the zeroth moment provides the mean transit time from the surface to interior (called age) or from the interior to surface (called life expectancy, Primeau (2005)). The TTD method has been widely used to provide a complementary diagnostic of ventilation process (Holzer and Hall, 2000; Haine and Hall, 2002; Primeau, 2005; Primeau and Holzer, 2006; Haine et al., 2008; Holzer and Primeau, 2010; DeVries and Primeau, 2011; Ali Muttaqi Shah et al., 2017). Therefore, I will use TTD method to study the ventilation of the deep water masses.

The ventilation rate itself cannot be measured directly, but the integrated effect of a multiplicity of ventilation processes separated in time and space is manifest in the time evolving concentration of transient hydrographic tracers, such as CFCs or radiocarbon.

Therefore, a reanalysis effort combining models and observations should provide the most accurate quantification of the ventilation process. There are several data-assimilation models. One is the Estimating the Circulation and Climate of the Ocean (ECCO) model which includes the initial state of the ocean as the main control variables. It repeatedly simulates the circulation for at most a few decades. The residual mean circulation from ECCO has been used in (Cessi, 2019) to derive the meridional transport of GOC, which agrees with Lumpkin and Speer (2007); Talley (2013) in Atlantic mid-depth cell but less certain with the global abyssal cells. However, the ventilation rates of these data-assimilated circulation models cannot produce stable water-mass distributions on timescales longer than those

used for the assimilation. Therefore, to avoid the short assimilation window, an alternative method that quantifies climatological ventilation rate have been developed, such as the model developed by Schlitzer (2007), the Ocean Circulation Inverse Model (OCIM: DeVries and Primeau (2011); DeVries and Holzer (2019). Here I use the CYCLOCIM developed in Chapter 2, which is the first climatological data-assimilation oceanic circulation model that includes the seasonal cycle. It provides better model fit to tracer data in the upper ocean compared to OCIM (Chapter 2). In Chapter 3, I have successfully applied the seasonally varying circulation from CYCLOCIM to quantify the Stommel's demon in the upper ocean. Therefore, I use the climatological monthly Transport Operator from CYCLOCIM to calculate the TTD and then quantify the ventilation of the deep water masses. The purpose of the present paper is to study the ventilation of the deep water masses by answering the question that when, in where and how much the water in the deep water masses were last in contact or will make the first contact with the surface. The plan is as follows. First, I calculate meridional transport streamfuncion and the zeroth and first moment of TTD of the deep ocean. Moreover, I examine the seasonality of the subduction and the obduction of the deep water to see whether it has strong seasonality like the "Stommel's demon" in the main thermocline (Chapter 3). Secondly, I calculate the subduction and obduction of the NADW, AABW, PDW and IDW separately to compared with previous studies (Lumpkin and Speer, 2007; Talley, 2013; Cessi, 2019).

4.2 Method

4.2.1 Cyclo-stationary Ocean Circulation Model

The Cyclo-stationary Ocean Circulation model (CYCLOCIM) is a 4D variational data-assimilation model that is constrained by transient tracer observations of the climatological

temperature, salinity, and natural (prebomb) radiocarbon and the transient chlorofluorocarbon (CFC-11, CFC-12) (see details in chapter 2). In the present study, I use the monthly transport operators from $4° \times 4°$CYCLOCIM to calculate the TTDs.

4.2.2 TTD method

The transit-time distribution (TTD) is a continuous distribution of times between successive visits of the water parcel. Base on the direction of pathways, there are surface-to-interior TTD, which describes the continuous transports of water from the surface to a specific location, and interior-to-surface TTD, which describes the continuous transports of water from the surface to a specific location (Primeau, 2005). The zeroth moment of TTD is the volume fraction of a specific water mass that makes its last and first contact with the sea surface. It can be used to obtain which months and what regions of the surface ocean are the most important in terms of subduction and obduction. The first moment of TTD is the mean time scale of water parcel that makes their last and first contact with the sea surface. It can be used to describe the ventilation time scales for the different surface regions and different months that water parcel is exchanged between the surface ocean and the interior ocean. In the present study, I use the adjoint model and the forward model combined with the Newton Krylov solver method (Kelley, 2013) to calculate the zeroth and first moments of TTD. The details of the method can be found in Chapter 3.

4.3 Results

In the present study, the deep ocean is selected as the region below 1000m. NADW, PDW, IDW are selected as the water between 1500m to 3000m in each ocean basin and their south boundary is 30°S. The definition is based on Talley (2013) who shows that the cores of

Table 4.1: (a) the fraction of water that subducted from the surface ocean to the specific interior ocean box (b) the mean transit time of the water parcel subducted from the surface ocean to the specific interior ocean box, also called the age of the water in the ocean box.

(a)

	Southern Ocean	Pacific	Atlantic	Indian Ocean
Deep Ocean	0.5025	0.0323	0.4546	0.0062
NADW	0.1473	0.0030	0.8488	0.0009
AABW	0.5958	0.0122	0.3879	0.0041
PDW	0.5628	0.0621	0.3705	0.0046
IDW	0.5392	0.0211	0.4143	0.0253

(b)

	Southern Ocean	Pacific	Atlantic	Indian Ocean
Deep Ocean	935	1011	884	947
NADW	674	1387	236	1081
AABW	563	1329	784	1011
PDW	1367	1013	1590	1734
IDW	947	1272	1050	534

the three water mass are approximately located between 1500 m to 3000m. The AABW is defined as the water below 4000m and between 90°S-30°S.

4.3.1 Deep ocean

Figure 4.1 shows the annual mean global stream function that calculated from the vertically and zonally integrated meridional residual mean velocity from CYCLOCIM. The meridional velocity is the residual mean circulation which is the sum of Eulerian velocity, and Bolus velocity that represents the eddy induced transport(see details in Chapter 2). Figure 4.1 shows two main global meridional cells: the mid-depth cell and the abyssal cell. The sinking of the deep water occurs mainly in the north side of the mid-depth cell ($> 30°$S) and the south side($> 60°$S) of the abyssal cell, while the upwelling mainly happens in the Southern Ocean between 40°S and 60°S. The pattern of cells agrees with those of Lumpkin and Speer

Table 4.2: (a) the fraction of water that subducted from the surface ocean to the specific interior ocean box (b) the mean transit time of the water parcel subducted from the surface ocean to the specific interior ocean box, also called the age of the water in the ocean box.

(a)

	Southern Ocean	Pacific	Atlantic	Indian Ocean
Deep Ocean	0.7893	0.1541	0.0352	0.0177
NADW	0.8866	0.0631	0.0410	0.0093
AABW	0.8681	0.0919	0.0285	0.0115
PDW	0.6846	0.2690	0.0253	0.0211
IDW	0.8624	0.0722	0.0334	0.0320

(b)

	Southern Ocean	Pacific	Atlantic	Indian Ocean
Deep Ocean	879	1260	835	1149
NADW	666	1750	646	1428
AABW	840	1823	1034	1583
PDW	1098	1032	1208	1165
IDW	796	1764	891	781

(2007) except for that the upper branch of the abyssal cell that is far below the surface. The meridional stream function calculated in Lumpkin and Speer (2007) only includes advection and ignores the mixing, while the upwelling in the upper Southern Ocean in my calculation is mainly driven by the mixing. Therefore, with or without strong mixing in the upper ocean will lead to a different versions of the meridional circulation.

Figure 4.2(a) shows how much of water in the deep ocean are transported from the surface by the advective-diffusive circulation, and Figure 4.3(b) shows how much of water in the deep ocean is transported back to the surface. It is shown that deep water formation occurs mainly in the south sides of the ACC, however, due to mixing, part of water between 30°S and 60°S is transported from the surface to the downwelling branch of the abyssal cell and formes the bottom water. Table 4.1a shows that the Southern Ocean contributes 50% of water to the deep ocean while the Atlantic Ocean contributes 45% to the deep ocean. The mean age of water from the Atlantic Ocean is 884 years while that originated from the

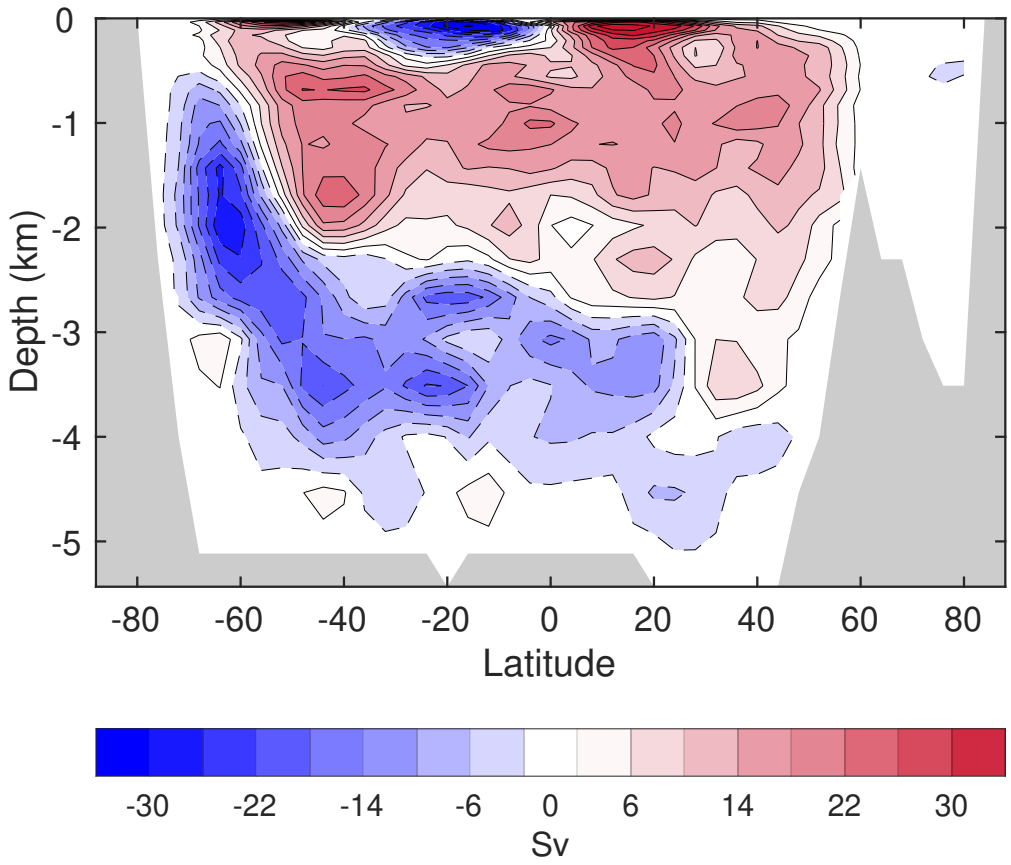

Figure 4.1: The Global climatogical mean meridional overturning circulation (MOC) stream function. The value is colored at 4 Sv intervals.

Southern Ocean is 935 years (table 4.1b).

Moreover, strong mixing in the Southern Ocean enables the deep water to return back to the surface across the Southern ocean basin between between 40°S to 80°S, although the advective upwelling branch is located between 40°S to 60°S (figure 2.12). The upwelling in the Southern Ocean transports 79% of water from the interior ocean back to the surface (table 4.1a). The rest of the water in the deep ocean is transported back to the Pacific (15%), the Atlantic (3%) and the Indian (1%). It takes an average of 879 years for water flow from the interior ocean to the surface Southern Ocean and 1261 years to the surface of the Pacific Ocean (table (4.2b)). Figure 4.2(b) and Figure 4.3(a) show strong seasonality in the ventilation process in the different ocean basins. The formation in the Atlantic starts in January, peaks in March and ends in May. In the Southern Ocean, the formation starts in

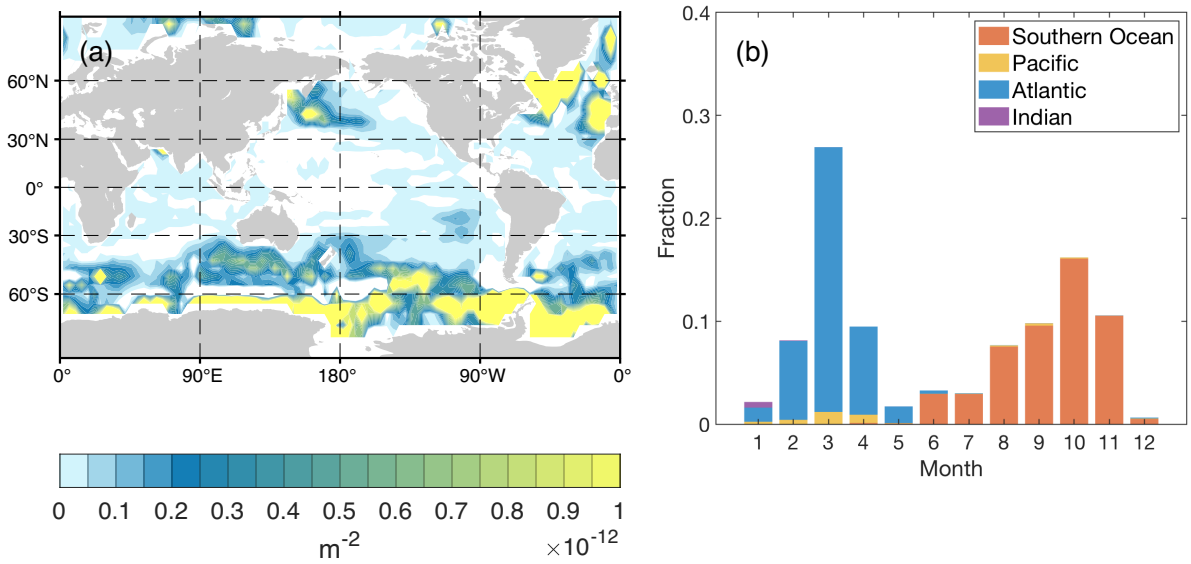

Figure 4.2: (a) The total volume fraction of the water in the deep ocean (below 1000m) that was transported from the surface ocean. The sum of the total fraction is equal to one. (b) the monthly distribution of water fraction that originated at different ocean basins: the Pacific (30°S - 60°N), the Atlantic (30°S - 60°N), the Indian Ocean (30°S - 30°N) and the Southern Ocean (30 - 90°S).

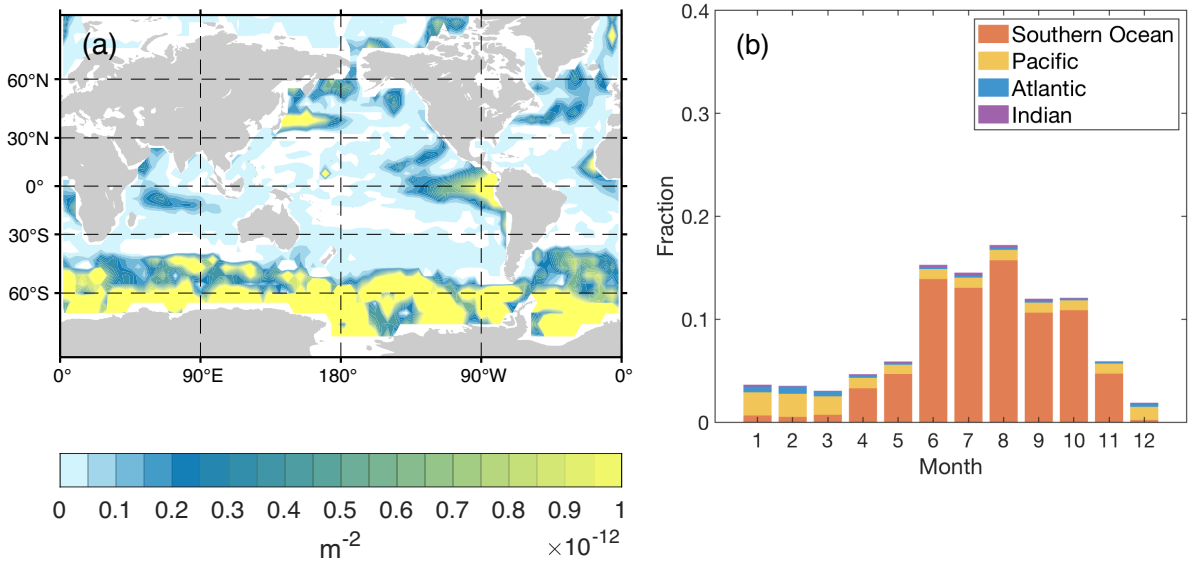

Figure 4.3: (a) The total volume fraction of the water in the deep ocean (below 1000m) that will be transported back to the surface ocean. The sum of the total fraction is equal to one. (b) The monthly distribution of volume fraction that returns to the different ocean basins: the Pacific (30°S - 60°N), the Atlantic (30°S - 60°N), the Indian Ocean (30°S - 30°N) and the Southern Ocean (30 - 90°S).

June, peaks in October and ends in November. Moreover, the return of water in the interior ocean to the surface Southern Ocean starts in April and ends in November, while its return to the surface Pacific occurs throughout the year due to the consistent equatorial Ekman upwelling. Next, I discuss the sinking and returning path of the four deep water masses: NADW, AABW, PDW, and IDW.

4.3.2 NADW

NADW is mainly formed in the Atlantic Ocean which contributes 85% of its water volume (table 4.1a). There are three main subduction regions: (1) the Labrador Sea and its extended northwest Atlantic region (2) the Nordic Sea and (3) the northeast Atlantic region (figure 4.4(a)). Water that sinks in the Labrador Sea forms the Labrador Sea Water (LSW), while warm water in the northeast Atlantic region mixes with the dense Arctic Ocean water and intermediate water from the Nordic Sea and then forms the Iceland-Scotland Overflow Water (ISOW) and Denmark Strait Overflow Water (DSOW). The pattern of subduction in North Atlantic is similar to the vertical transport between the potential density layer of 37 kg/m^3 and the sea surface in (Cessi, 2019). Moreover, 15% of the NADW comes from the Southern Ocean which proves the upwelling of the AABW into the NADW. The mean age of the water that subducted from Atlantic is 236 years and the water that subducted from the Southern Ocean is 674 years.

The return of NADW to surface occurs mainly in the Southern Ocean (88%, table (4.2a)). There are two potential paths that transport NADW back to the Southern Ocean: (1) approximate 40% of NADW follows the direct adiabatic upwelling routes to the surface mixed layer (2) 60% of NADW entrain into the lower branch of the abyssal cells and then transformed to the denser bottom water and then follows the AABW upwelling path (Lumpkin and Spear, 2007). However, Talley (2013) argued that all the NADW recycles through the

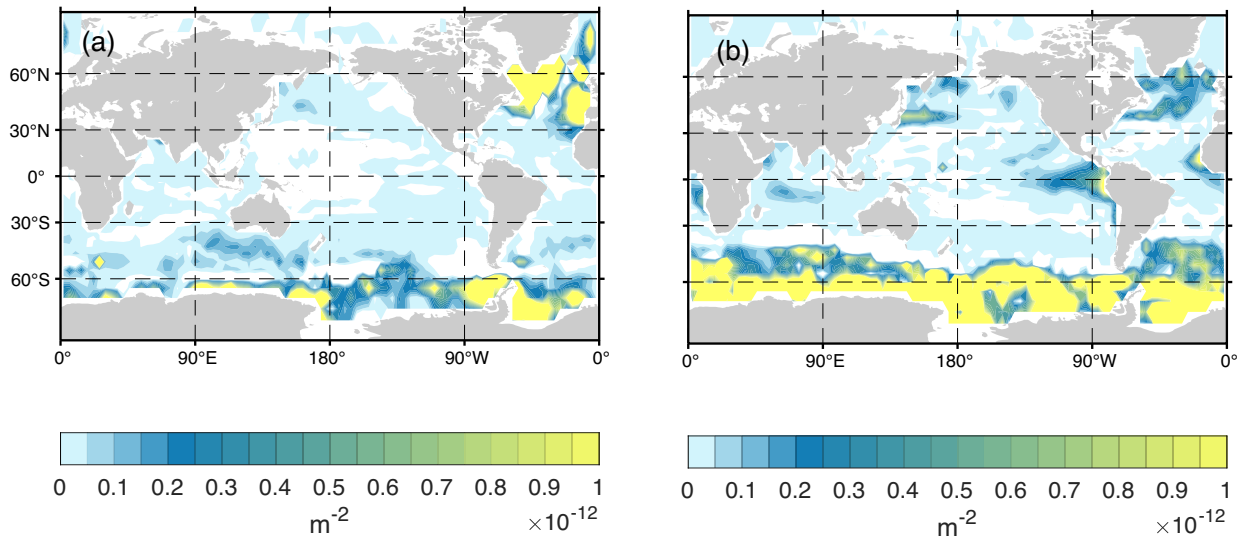

Figure 4.4: (a) The total volume fraction of the water of NADW that was transported from the surface ocean. (b) The total volume fraction of the water of NADW that will be transported back to the surface ocean. The sum of the total volume fraction is equal to one in each figure

abyssal cells. It is unclear to see which return path is correct in the present study. Moreover, a small fraction of NADW upwells to the surface of the Pacific (6%) and the Atlantic (4%) (Table 4.2a). It takes a relatively short time for NADW to return to the surface Southern Ocean (666 years) compared to the surface Pacific (1750 years) (Table 4.2b). The potential return pathway of NADW to the surface Pacific is through merging with PDW and then upwell to the Sea Surface, and the potential pathway to the surface Atlantic is through the northward transport of the upwelled NADW water into the thermoclines and hence the return flow to the North Atlantic (Talley, 2013).

4.3.3 AABW

AABW is the combination of the surface water in Southern Ocean (60%) and the North Atlantic Ocean water (39%) (Table 4.2a and Figure 4.5a). AABW that forms near the Antarctic continent is the result of the Antarctic winds and formation of the sea ice during the winter (Talley, 1999). Moreover, AABW that subducted from North Atlantic is mainly due to the southward flow of NADW which enters the lower branch of the abyssal cell and then transformed to the denser bottom-water classes (Lumpkin and Speer, 2007; Talley, 2013). The mean age of AABW that from the Southern Ocean is 563 year and that from NADW is 784 year.

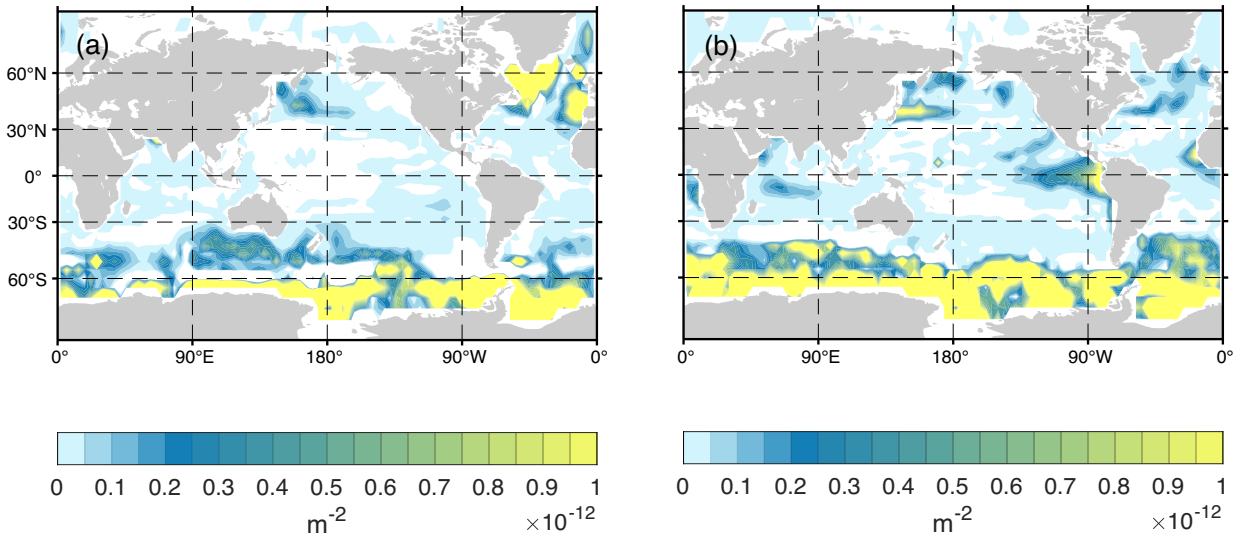

Figure 4.5: (a) The total volume fraction of the water of AABW that was transported from the surface ocean. (b) The total volume fraction of the water of AABW that will be transported back to the surface ocean. The sum of the total volume fraction is equal to one in each figure

The obduction of AABW is mainly through upwelling into the deep water masses of the three oceans and then return back to the surface Southern ocean (Talley, 2013). Moreover, 10% of upwelled AABW flows northward into the main thermocline of pacific and then returns to the surface, which takes average 1823 years.

4.3.4 PDW and IDW

It is shown that 56% of PDW water originates from the surface Southern Ocean, however, 37% of water comes form the surface of the North Atlantic (Figure 4.6a and Table 4.1a). Similar to PDW, IDW is the combination of the surface water in the Southern Ocean (53%) and the North Atlantic (41%). However, more IDW comes from the regions between 30°S and 60°S than PDW. Talley (2013) pointed out that AABW is the sole source of the PDW and IDW. Therefore, one possible connection between the surface North Atlantic, PDW, and IDW is through the transformation of NADW into AABW. However, Ali et al 2007 shows three typical pathways of particle that travels from the surface North Atlantic to the Deep Pacific Ocean and none of them is associated with the formation of AABW. The mean age of water that comes from North Atlantic is 1590 years and the mean age of water that comes from North Pacific is 1367 years. Besides, 6% of PDW water is subducted from the northwestern part of the subtropical gyre, which implies the weak meridional cells in the Pacific.

The return of PDW to the surface mainly happens in the Southern Ocean (67%) and the Pacific (27%) (Table 4.2a and Figure 4.6b), which agrees with Talley (2013) that there are two upwelling pathways that return the PDW to the surface: The adiabatic upwelling in the Southern ocean and the diapycnal upwelling in the northwestern of the subtropical gyre and in the eastern tropical Pacific. However, the return of IDW to the surface occurs mainly in the Southern Ocean (86%) (table 4.2 and 4.7b). Only 3% of the IDW returns to the surface of the Indian Ocean suggesting that the diapycnal upwelling in the Indian Ocean is not as strong as the Pacific Ocean. Moreover, 7% of IDW travels to the pacific and return to the mixed layer. It takes average 1098 years and 1032 years for PDW to return back to the surface of the Southern and the Pacific ocean, while it takes an average of 1098 years and 1032 years for IDW to be transported back to the surface of the Southern Ocean and the Pacific.

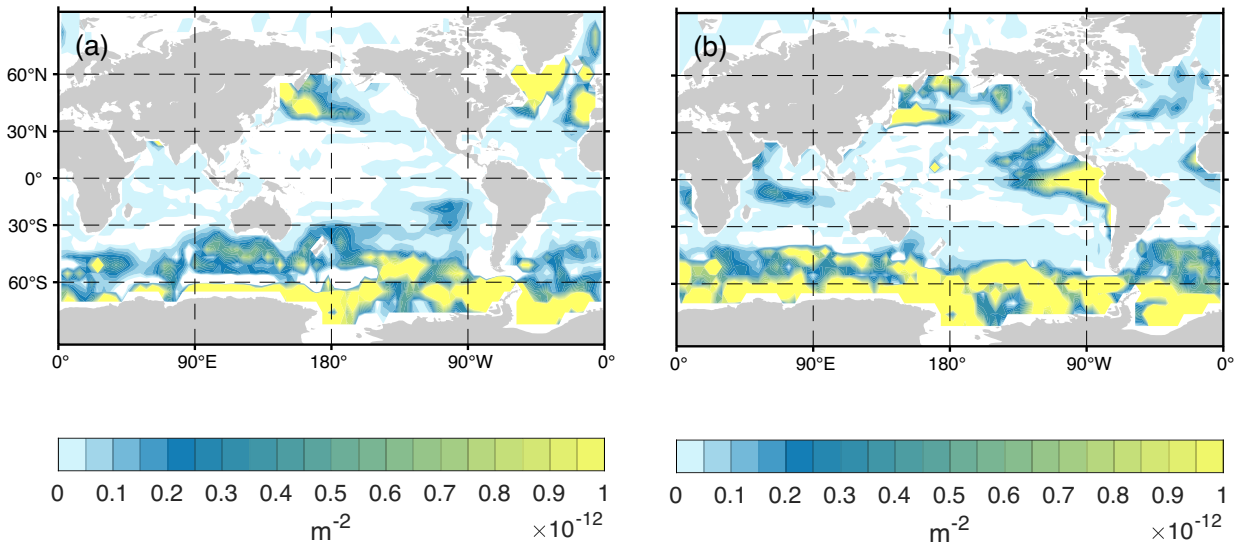

Figure 4.6: (a) The total volume fraction of the water of PDW that was transported from the surface ocean. (b) The total volume fraction of the water of PDW that will be transported back to the surface ocean. The sum of the total volume fraction is equal to one in each figure.

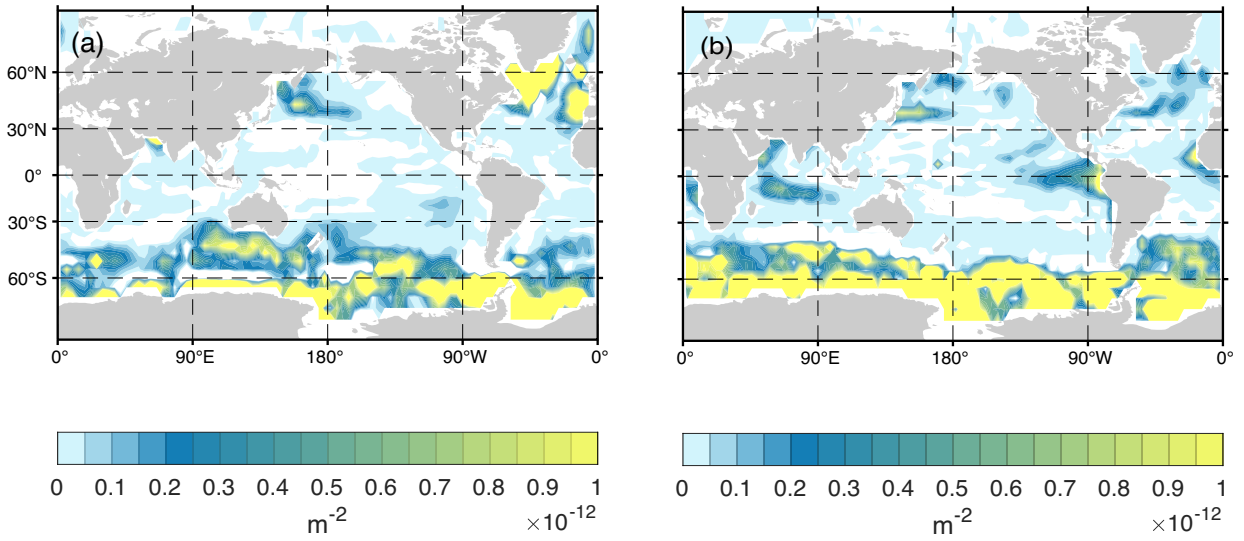

Figure 4.7: (a) The total volume fraction of the water of IDW that was transported from the surface ocean. (b) The total volume fraction of the water of IDW that will be transported back to the surface ocean. The sum of the total volume fraction is equal to one in each figure.

4.4 Discussion

The present study analyzes the sinking and upwelling of the deep water masses using the monthly varying residual mean circulation from CYCLOCIM. Compared with the previous studies of GOC that focusing on the pathways in the interior ocean (Lumpkin and Speer, 2007; Talley, 2013; Cessi, 2019), the present study demonstrates the surface branch of the GOC by calculating where, in which month and how much of the water in the deep water masses was transported from or will be transported back to the surface. It shows the main sinking of NADW, AABW, PDW, IDW occurs in the Southern Ocean (respectively, 15%, 69%, 56% and 53%) and the Atlantic Ocean (respectively, 84%, 39%, 37% and 41%). The deep water formation in the Atlantic starts in January, peaks in March and ends in May. In the Southern Ocean, deep water formation starts in June, peaks in October and ends in November. Moreover, the upwelling in the Southern Ocean starts in April and ends in November. In the Pacfic, it occurs throughout lasts the whole year due to the tropical Ekman upwelling. The results agree with previous studies that the main return pathways of the deep water are the Southern Ocean. However, the adiabatic upwelling in the Indian Ocean is not as important as it is suggested by Talley (2013).

Since our analysis focuses on the summary diagnostics of the surface and ignores the pathway information of the interior ocean, it is insufficient to provide complete pictures of GOC. Therefore, future work should include the Lagrangian particle diagnostics which have been applied in OCIM (Ali Muttaqi Shah et al., 2017) and the water mass transformation diagnostics (Groeskamp et al., 2019) to produce a data-constrained estimate of the overturning circulation pathway along with water mean transformation .

Chapter 5

Discussion and future work

The thesis presented a study of the climatological mean seasonal cycle of ventilation. To obtain the monthly varying circulation that agrees with observation, I have developed a computationally efficient 4-D variational assimilation system called CYCLOCIM (Chapter 2). CYCLOCIM is a novel variational assimilation system that is specifically designed to the problem of estimating the climatological seasonal cycle of the residual mean circulation. The main product of the assimilation system is a set of 12 monthly data-constrained tracer-transport operators. I applied the transport operators combined with the TTD method to quantify the seasonality of the ventilation in the main thermocline (Chapter 3) and estimate the sinking and returning of deep water masses from or to the surface (Chapter 4).

Chapter 2 describes the detailed formulation of CYCLOCIM and compares the model results with previous studies. CYCLOCIM assimulates monthly mean temperature and salinity data from the World Ocean Atlas, transient CFC-11 and CFC12 tracers, and natural radiocarbon measurements for the deep ocean from the GLODAPv2 database. The adjustable parameters of CYCLOCIM are the unresolved eddy stresses in the horizontal momentum equations and the surface heat, fresh water in the tracer equations. I infer the adjustable parameters of the

CYCLOCIM by a Bayesian inversion procedure and hence reconstruct the data-assimilation problem as a constrained optimization problem. The optimization process includes the forward simulation system to calculate the circulation and the transport of tracers, the backward adjoint system to calculate the gradient and the quasi-newton search algorithm. The analysis shows that the modeled overturning circulation and the meridional heat and the fresh water transport largely agree with existing studies. Moreover, CYCLOCIM improves the model fit to the observation in the upper ocean compared to OCIM (DeVries and Primeau, 2011) which ignored the seasonal cycle. In conclusion, the CYCLOCIM have successfully produced a periodic annual cycle that agrees with the climatiological monthly tracer data.

I, therefore, anticipate that the 12 transport operators will be useful for the global biogeochemical inversion for which there is a need for reliable estimates of the seasonally varying climatiological transport of tracers. In other words, previous studies that used the annual mean transport operator form OCIM should be revisited using the new transport operators (e.g. DeVries et al., 2013; Holzer and Primeau, 2013; Devries and Deutsch, 2014; DeVries, 2014; Holzer et al., 2014; Teng et al., 2014; Frants et al., 2015; Holzer et al., 2016; Weber et al., 2016; DeVries et al., 2017; Pasquier and Holzer, 2016; Roshan et al., 2017; Pasquier and Holzer, 2017; Roshan and DeVries, 2017; Holzer et al., 2017; John et al., 2018; Wang et al., 2019; Martin et al., 2019b,a).

More work need to be done to improve CYCLOCIM. First, the solution I presented here is for a version of CYCLOCIM with a $4^\circ \times 4^\circ$ resolution, but I am presently optimizing a $2^\circ \times 2^\circ$ version of the model. Moreover, I ignored valuable constraints on the dynamic topography of the model provided by satellite altimeter data. I plan on including this constraint in future versions of CYCLOCIM. Furthermore, CYCLOCIM has produced the time-and-space dynamically intepolated CFC-11 and CFC-12, which can be used for other studies. Another avenue for future work is to produce an ensemble of tracer transport operators drawn from the Bayesian posterior distribution for the eddy-stresses and surface forcing. So far I have only

sampled the maximum of the posterior distribution but the development of a computationally efficient means of drawing samples from the posterior should be a high priority for future work.

Chapter 3 demonstrates a novel way to quantify the "Stommel's demon" by calculating where, in which month and how much of the water in the main thermocline was last subducted from the surface or will be first obducted back to the surface. The present study has addressed two main flaws of the previous studies (Marshall et al., 1993, 1999; Qiu and Huang, 1995; Williams et al., 1995; Liu and Huang, 2011), that is, the neglect of diffusion along the isopycnal layers and the failure to provide an accurate estimate of the effective subduction and obduction period. To address these shortcomings, I used the transport operators from CYCLOCIM which produced the best estimate of the climatiological advective and diffusive circulation of the ocean, and applied the TTD method to describe the time distribution of the transport to and from the mixed layer by the advective and diffusive process. I also developed a periodic solver that enables efficient calculation of the zeroth and first moments of TTD without direct calculation of TTD. The method provides the first application of the TTD method to obtain which months and surface areas contributes the most in terms of subduction and obduction.

Chapter 3 provides an accurate estimate of the effective subduction and obduction period and the fraction of each month's contribution. It shows that the effective subduction happening in the Southern Ocean (64%) lasts from June to November and peaks at September (21%) and October (20%), and in the surface North Pacific (12%) and the surface North Atlantic (16%) lasts from January to April and peaks at March (15%). The obduction occurs mainly in the ACC region (48%). The Southern Ocean Obduction occurs from April to November and peaks in August. The tropical ocean transport 35% of the water in the upper ocean back to the surface. The obduction in the tropical region occurs throughout the whole year. The rest of the obduction takes place at the North Atlantic (10%) and the North Pacific

(8%) and the effective period is from January to Febrary. Moreover, unlike the previous studies which only explain the local selection of water property in the mixed layer (Marshall et al., 1993, 1999; Qiu and Huang, 1995; Liu and Huang, 2011), the TTD method provides a picture of the fraction of the surface water over the global ocean that forms the main thermocline. For example, the main thermocline in the North Pacific not only selects the late winter and early spring water properties of the mixed layer in the North Pacific but also selects early spring properties of the mixed layer in the North Atlantic, and the late winter and early spring water properties in the Southern Ocean.

Chapter 4 analyzes the sinking and upwelling of the deep water masses in the surface ocean using the monthly varying residual mean circulation from CYCLOCIM (Chapter2) and the TTD method (Chapter 3). Compared with the previous studies of the global overturning circulation (GOC) that focused on the pathways in the interior ocean (Lumpkin and Speer, 2007; Talley, 2013; Cessi, 2019), the present study demonstrates the surface branch of the GOC by calculating where, when and how much of water in deep water masses was transported from or will be transported back to the surface by the advective and diffusive circulation. It is shown that formation of NADW, AABW, PDW, IDW mainly occurs in the Southern Ocean (respectively, 15%, 69%, 56% and 53%) and the Atlantic Ocean (respectively, 84%, 39%, 37% and 41%). Moreover, the sinking and upwelling of the deep water masses shows strong seasonality as the ventilation of the main thermocline in Chapter 3. The formation of deep water in the Atlantic starts in January, peaks in March and ends in May. The formation of deep water in the Southern Ocean starts in June, peaks in October and ends in November. Furthermore, the upwelling in the Southern Ocean starts in April and ends in November, and the upwelling in the Pacific happens throughout the year. In agreement with previous studies, I found that the main return pathway of deep water is the upwelling in the Southern Ocean. However, the adiabatic upwelling in the Indian Ocean suggested by Talley (2013) is not evident from my analysis. Since my analysis focuses on the summary diagnostics of the surface and ignores the pathway information of the interior

ocean, it is insufficient to provide complete pictures of GOC. Therefore, further work should apply the Lagrangian particle diagnostics which have been applied in OCIM (Ali Muttaqi Shah et al., 2017) and the water mass transformation diagnostics (Groeskamp et al., 2019) to produces a complete picture of the data-constrained estimate of the overturning circulation pathway.

Bibliography

Ali Muttaqi Shah, S. H., Primeau, F. W., Deleersnijder, E., Heemink, A. W., 2017. Tracing the Ventilation Pathways of the Deep North Pacific Ocean Using Lagrangian Particles and Eulerian Tracers. Journal of Physical Oceanography 47 (6), 1261–1280.

Balmaseda, M. A., Hernandez, F., Storto, A., Palmer, M. D., Alves, O., Shi, L., Smith, G. C., Toyoda, T., Valdivieso, M., Barnier, B., Behringer, D., Boyer, T., Chang, Y.-S., Chepurin, G. A., Ferry, N., Forget, G., Fujii, Y., Good, S., Guinehut, S., Haines, K., Ishikawa, Y., Keeley, S., KÃ¶hl, A., Lee, T., Martin, M. J., Masina, S., Masuda, S., Meyssignac, B., Mogensen, K., Parent, L., Peterson, K. A., Tang, Y. M., Yin, Y., Vernieres, G., Wang, X., Waters, J., Wedd, R., Wang, O., Xue, Y., Chevallier, M., Lemieux, J.-F., Dupont, F., Kuragano, T., Kamachi, M., Awaji, T., Caltabiano, A., Wilmer-Becker, K., Gaillard, F., 2015. The Ocean Reanalyses Intercomparison Project (ORA-IP). Journal of Operational Oceanography 8 (sup1), s80–s97.

Bardin, A., Primeau, F., Lindsay, K., 2014. An offline implicit solver for simulating prebomb radiocarbon. Ocean Modelling 73, 45–58.

Botev, Z. I., Grotowski, J. F., Kroese, D. P., 2010. Kernel density estimation via diffusion. Ann. Statist. 38 (5), 2916–2957.

Bower, A., Lozier, S., Gary, S., 2011. Export of Labrador Sea Water from the subpolar North Atlantic: A Lagrangian perspective. Deep Sea Research Part II: Topical Studies in Oceanography 58 (17), 1798–1818.

Bower, A. S., Lozier, M. S., Gary, S. F., Böning, C. W., 2009. Interior pathways of the North Atlantic meridional overturning circulation. Nature 459 (7244), 243–247.

Boyer, T. P., Antonov, J. I., Baranova, O. K., Garcia, H. E., Johnson, D. R., Mishonov, A. V., O'Brien, T. D., Seidov 1948-, D., Smolyar, I. I., Zweng, M. M., Paver, C. R., Locarnini, R. A., Reagan, J. R., Forgy, C. C., Grodsky, A., Levitus, S., 2013. World ocean database 2013.

Broecker, W., 1987. The biggest chill. Natural History Magazine 97, 74–84.

Broecker, W., 1991. The Great Ocean conveyor. Oceanography 4, 79–87.

Cessi, P., 2019. The global overturning circulation. Vol. 11 of Annual Review of Marine Science. Annual Reviews, Palo Alto, pp. 249–270.

Dall'Olmo, G., Dingle, J., Polimene, L., Brewin, R. J. W., Claustre, H., sep 2016. Substantial energy input to the mesopelagic ecosystem from the seasonal mixed-layer pump. Nature Geoscience 9, 820.

de Boyer Montégut, C., Madec, G., Fischer, A. S., Lazar, A., Iudicone, D., dec 2004. Mixed layer depth over the global ocean: An examination of profile data and a profile-based climatology. Journal of Geophysical Research: Oceans 109 (C12).

DeVries, T., 2014. The oceanic anthropogenic CO2 sink: Storage, air-sea fluxes, and transports over the industrial era. Global Biogeochemical Cycles 28 (7), 631–647.

Devries, T., Deutsch, C., 2014. Large-scale variations in the stoichiometry of marine organic matter respiration. Nature Geoscience 7 (12), 890–894.

Devries, T., Deutsch, C., Primeau, F., Chang, B., Devol, A., 2012a. Global rates of water-column denitrification derived from nitrogen gas measurements. Nature Geoscience 5 (8), 547–550.

DeVries, T., Deutsch, C., Rafter, P. A., Primeau, F., 2013. Marine denitrification rates determined from a global 3-D inverse model. Biogeosciences 10 (4), 2481–2496.

DeVries, T., Holzer, M., 2019. Radiocarbon and Helium Isotope Constraints on Deep Ocean Ventilation and Mantle-3He Sources. Journal of Geophysical Research: Oceans 124 (5), 3036–3057.

DeVries, T., Holzer, M., Primeau, F., 2017. Recent increase in oceanic carbon uptake driven by weaker upper-ocean overturning. Nature 542 (7640), 215–218.

DeVries, T., Primeau, F., 2011. Dynamically and Observationally Constrained Estimates of Water-Mass Distributions and Ages in the Global Ocean. Journal of Physical Oceanography 41 (12), 2381–2401.

Devries, T., Primeau, F., Deutsch, C., 2012b. The sequestration efficiency of the biological pump. Geophysical Research Letters 39 (13), 1–5.

Devries, T., Weber, T. S., 2017. The export and fate of organic matter in the ocean : New constraints from combining satellite and oceanographic tracer observations. Global Biogeochemical Cycles 31 (3), 535–555.

Ferreira, D., Marshall, J., Heimbach, P., 2005. Estimating Eddy Stresses by Fitting Dynamics to Observations Using a Residual-Mean Ocean Circulation Model and Its Adjoint. Journal of Physical Oceanography 35 (10), 1891–1910.

Forget, G., Campin, J.-M., Heimbach, P., Hill, C. N., Ponte, R. M., Wunsch, C., oct 2015. ECCO version 4: an integrated framework for non-linear inverse modeling and global ocean state estimation. Geosci. Model Dev. 8 (10), 3071–3104.

Frants, M., Holzer, M., DeVries, T., Matear, R., 2015. Constraints on the global marine iron cycle from a simple inverse model. Journal of Geophysical Research: Biogeosciences 121 (1), 28–51.

Fu, W., Primeau, F., 2017. Application of a fast Newton–Krylov solver for equilibrium simulations of phosphorus and oxygen. Ocean Modelling 119, 35–44.

Ganachaud, A., Wunsch, C., 2000. Improved estimates of global ocean circulation, heat transport and mixing from hydrographic data. Nature 408 (6811), 453–457.

Groeskamp, S., Griffies, S. M., Iudicone, D., Marsh, R., Nurser, A. J. G., Zika, J. D., jan 2019. The Water Mass Transformation Framework for Ocean Physics and Biogeochemistry. Annual Review of Marine Science 11 (1), 271–305.

Haine, T. W. N., Hall, T. M., jun 2002. A Generalized Transport Theory: Water-Mass Composition and Age. Journal of Physical Oceanography 32 (6), 1932–1946.

Haine, T. W. N., Zhang, H., Waugh, D. W., Holzer, M., 2008. On transit-time distributions in unsteady circulation models. Ocean Modelling 21 (1), 35–45.

Haltiner, G. J., Williams, R. T., 1980. Numerical Prediction and Dynamical Meteorology Second Edition. John Wiley & Sons.

Hanawa, K., Talley, L. D., 2001. Mode Waters. No. 77 in International geophysics series. Academic, San Diego, Calif. London, pp. 373–386.

Heinkenschloss, M., 2008. Numerical solution of implicitly constrained optimization problems. CAAM Technical Report.

Holzer, M., DeVries, T., Bianchi, D., Newton, R., Schlosser, P., Winckler, G., 2017. Objective estimates of mantle3He in the ocean and implications for constraining the deep ocean circulation. Earth and Planetary Science Letters 458, 305–314.

Holzer, M., Frants, M., Pasquier, B., 2016. The age of iron and iron source attribution in the ocean. Global Biogeochemical Cycles 30 (10), 1454–1474.

Holzer, M., Hall, T. M., nov 2000. Transit-Time and Tracer-Age Distributions in Geophysical Flows. Journal of the Atmospheric Sciences 57 (21), 3539–3558.

Holzer, M., Primeau, F. W., dec 2010. Improved constraints on transit time distributions from argon 39: A maximum entropy approach. Journal of Geophysical Research: Oceans 115 (C12).

Holzer, M., Primeau, F. W., 2013. Global teleconnections in the oceanic phosphorus cycle: Patterns, paths, and timescales. Journal of Geophysical Research: Oceans 118 (4), 1775–1796.

Holzer, M., Primeau, F. W., DeVries, T., Matear, R., 2014. The Southern Ocean silicon trap: Data-constrained estimates of regenerated silicic acid, trapping efficiencies, and global transport paths. Journal of Geophysical Research: Oceans 119 (1), 313–331.

Iselin, C. O., jul 1939. The influence of vertical and lateral turbulence on the characteristics of the waters at mid-depths. Eos, Transactions American Geophysical Union 20 (3), 414–417.

John, S. G., Helgoe, J., Townsend, E., Weber, T., DeVries, T., Tagliabue, A., Moore, K., Lam, P., Marsay, C. M., Till, C., 2018. Biogeochemical cycling of Fe and Fe stable isotopes in the Eastern Tropical South Pacific. Marine Chemistry 201 (March), 66–76.

Kelley, C. T., 2013. Solving nonlinear equations with Newton's method. Society for Industrial and Applied Mathematics, Philadelphia, PA.

Khatiwala, S., 2008. Fast spin up of Ocean biogeochemical models using matrix-free Newton-Krylov. Ocean Modelling 23 (3-4), 121–129.

Köhl, A., jan 2015. Evaluation of the GECCO2 ocean synthesis: transports of volume, heat and freshwater in the Atlantic. Quarterly Journal of the Royal Meteorological Society 141 (686), 166–181.

Kwon, E. Y., 2014. Global estimate ofsubmarinegroundwaterdischarge basedonanobservationallyconstrained radium isotope model Eun. Geophysical Research Letters, 1–7.

Kwon, E. Y., Downes, S. M., Sarmiento, J. L., Farneti, R., Deutsch, C., jan 2013. Role of the Seasonal Cycle in the Subduction Rates of Upper–Southern Ocean Waters. Journal of Physical Oceanography 43 (6), 1096–1113.

Large, W. G., Yeager, S. G., aug 2009. The global climatology of an interannually varying air–sea flux data set. Climate Dynamics 33 (2), 341–364.

Leonard, B. P., 1979. A stable and accurate convective modelling procedure based on quadratic upstream interpolation. Computer Methods in Applied Mechanics and Engineering 19 (1), 59–98.

Li, X., Primeau, F. W., 2008. A fast Newton-Krylov solver for seasonally varying global ocean biogeochemistry models. Ocean Modelling 23 (1-2), 13–20.

Liang, X., Spall, M., Wunsch, C., 2017. Global Ocean Vertical Velocity From a Dynamically Consistent Ocean State Estimate. Journal of Geophysical Research: Oceans 122 (10), 8208–8224.

Liu, L. L., Huang, R. X., aug 2011. The Global Subduction/Obduction Rates: Their Interannual and Decadal Variability. Journal of Climate 25 (4), 1096–1115.

Lozier, M. S., Gary, S. F., Bower, A. S., 2013. Simulated pathways of the overflow waters in the North Atlantic: Subpolar to subtropical export. Deep Sea Research Part II: Topical Studies in Oceanography 85, 147–153.

Lumpkin, R., Speer, K., oct 2007. Global Ocean Meridional Overturning. Journal of Physical Oceanography 37 (10), 2550–2562.

Marshall, J., Jamous, D., Nilsson, J., 1999. Reconciling thermodynamic and dynamic methods of computation of water-mass transformation rates. Deep Sea Research Part I: Oceanographic Research Papers 46 (4), 545–572.

Marshall, J., Schott, F., 1999. Open-ocean convection: Observations, theory, and models. Reviews of Geophysics 37 (1), 1–64.

Marshall, J. C., Williams, R. G., Nurser, A. J. G., jul 1993. Inferring the Subduction Rate and Period over the North Atlantic. Journal of Physical Oceanography 23 (7), 1315–1329.

Martin, T. S., Primeau, F., Casciotti, K. L., 2019a. Assessing marine nitrogen cycle rates and process sensitivities with a global {3D} inverse model. {G}lobal {B}iogeochem. {C}ycles accepted August 4 (n.a), n.a.

Martin, T. S., Primeau, F., Casciotti, K. L., 2019b. Modeling oceanic nitrate and nitrite concentrations and isotopes using a 3-{D} inverse {N} cycle model. Biogeosciences 16 (2), 347–367.

Olsen, A., Key, R. M., van Heuven, S., Lauvset, S. K., Velo, A., Lin, X., Schirnick, C., Kozyr, A., Tanhua, T., Hoppema, M., Jutterström, S., Steinfeldt, R., Jeansson, E., Ishii, M., Pérez, F. F., Suzuki, T., aug 2016. The Global Ocean Data Analysis Project version 2 (GLODAPv2) – an internally consistent data product for the world ocean. Earth Syst. Sci. Data 8 (2), 297–323.

Pasquier, B., Holzer, M., 2016. The plumbing of the global biological pump: Efficiency control through leaks, pathways, and time scales. Journal of Geophysical Research: Oceans 121 (8), 6367–6388.

Pasquier, B., Holzer, M., 2017. Inverse-model estimates of the ocean's coupled phosphorus, silicon, and iron cycles. Biogeosciences 14 (18), 4125–4159.

Primeau, F., 2005. Characterizing Transport between the Surface Mixed Layer and the Ocean Interior with a Forward and Adjoint Global Ocean Transport Model. Journal of Physical Oceanography 35 (4), 545–564.

Primeau, F. W., Holzer, M., jul 2006. The Ocean's Memory of the Atmosphere: Residence-Time and Ventilation-Rate Distributions of Water Masses. Journal of Physical Oceanography 36 (7), 1439–1456.

Primeau, F. W., Holzer, M., DeVries, T., 2013. Southern Ocean nutrient trapping and the efficiency of the biological pump. Journal of Geophysical Research: Oceans 118 (5), 2547–2564.

Qiu, B., Huang, R. X., oct 1995. Ventilation of the North Atlantic and North Pacific: Subduction Versus Obduction. Journal of Physical Oceanography 25 (10), 2374–2390.

Richardson, P. L., 2008. On the history of meridional overturning circulation schematic diagrams. Progress in Oceanography 76 (4), 466–486.

Roshan, S., DeVries, T., 2017. Efficient dissolved organic carbon production and export in the oligotrophic ocean. Nature Communications 8 (1), 2036.

Roshan, S., Wu, J., DeVries, T., 2017. Controls on the Cadmium-Phosphate Relationship in the Tropical South Pacific. Global Biogeochemical Cycles 31 (10), 1516–1527.

Schlitzer, R., 1993. Determining the mean, large-scale circulation of the Atlantic with the adjoint method. Journal of Physical Oceanography 23, 1935–1952.

Schlitzer, R., 2007. Assimilation of Radiocarbon and Chlorofluorocarbon Data to Constrain Deep and Bottom Water Transports in the World Ocean. Journal of Physical Oceanography 37 (2), 259–276.

Stammer, D., Wunsch, C., Giering, R., Eckert, C., Heimbach, P., Marotzke, J., Adcroft, A., Hill, C. N., Marshall, J., 2002. Global ocean circulation during 1992–1997, estimated from ocean observations and a general circulation model. Journal of Geophysical Research: Oceans 107 (C9), 1–27.

Stommel, H., jul 1979. Determination of water mass properties of water pumped down from the Ekman layer to the geostrophic flow below. Proceedings of the National Academy of Sciences 76 (7), 3051 LP – 3055.

Talley, L. D., 1999. Some aspects of ocean heat transport by the shallow, intermediate and deep overturning circulations. No. 112 in Geophysical monograph series. American Geophysical Union, Washington, DC, pp. 1–22.

Talley, L. D., mar 2013. Closure of the Global Overturning Circulation Through the Indian, Pacific, and Southern Oceans: Schematics and Transports. Oceanography 26 (1), 80–97.

Teng, Y. C., Primeau, F. W., Moore, J. K., Lomas, M. W., Martiny, A. C., 2014. Global-scale variations of the ratios of carbon to phosphorus in exported marine organic matter. Nature Geoscience 7 (12), 895–898.

Trenberth, K. E., Large, W. G., J.G., O., 1989. A global ocean wind stress climatology based on {ECMWF} analyses.

Wang, W.-L., Moore, J. K., Martiny, A. C., Primeau, F. W., 2019. Convergent estimates of marine nitrogen fixation. Nature 566 (7743), 205–211.

Waugh, D. W., Primeau, F., Devries, T., Holzer, M., 2013. Recent changes in the ventilation of the southern oceans. Science (New York, N.Y.) 339 (6119), 568–70.

Weber, T., Cram, J. A., Leung, S. W., DeVries, T., Deutsch, C., 2016. Deep ocean nutrients imply large latitudinal variation in particle transfer efficiency. Proceedings of the National Academy of Sciences 113 (31), 8606–8611.

Weber, T., John, S., Tagliabue, A., DeVries, T., 2018. Biological uptake and reversible scavenging of zinc in the global ocean. Science 361 (6397), 72–76.

Wenzel, M., SchrÃ¶ter, J., Olbers, D., 2001. The annual cycle of the global ocean circulation as determined by 4D VAR data assimilation. Progress in Oceanography 48 (1), 73–119.

Williams, R. G., Marshall, J. C., Spall, M. A., dec 1995. Does Stommel's Mixed Layer "Demon" Work? Journal of Physical Oceanography 25 (12), 3089–3102.

Wunsch, C., 1996. The Ocean Circulation Inverse Problem. Cambridge University Press.